Development and Validation of Image Processing Framework for Dynamic Quantitative Morphometric Analyses of Joint and Osteochondral Tissues

Pholpat Durongbhan

ORCID: 0000-0002-5164-3482

July 2023

Department of Biomedical Engineering

Faculty of Engineering and Information Technology

The University of Melbourne

Submitted in total fulfilment of the requirements of the degree of

Doctor of Philosophy in Engineering

Dedicated to my parents.

My philosophers at home:

Phol and Apiradee Durongbhan

ลิขิตวิจิตรด้วย ศุภอรรถ

ด่งงมณิจินดารัตน์ เลอศแล้ว

อันมีศิริสวัสดิ โสภาคย์

ใครรู้ถือได้แก้ว ค่าแท้ควรเมือง

จินดามณี, ค.ศ. ๑๘๗๓

แบบเรียนภาษาไทยฉบับแรก

The one who reads, wise and learned,

Holds a gem of priceless worth,

Jewel of knowledge, prosperity it brings,

Illuminating the path beyond earthly things.

Jindamanee, 1873

The first Thai grammar book

Abstract

Quantitative morphometric analysis (QMA) using micro-computed tomography (microCT) allows non-invasive assessment of structural degradation of joint tissues, such as bone and cartilage, during osteoarthritis (OA) progression in small animal knees. Whole-joint features, such as joint space width and joint alignment, were shown to provide sensitive markers of biomechanical changes due to OA. As elastic links, the relative position of joint components can vary. Combined with traditional manual image processing and analysis approaches that requires recalibration between studies, QMA of the joint often encounters reproducibility issues that are technically challenging and time-consuming to tackle.

The general aim of this thesis is to examine how improvements in image processing protocols can lead to reproducible and dynamic quantitative analysis of joint morphology. In this work, reproducibility issues in the acquisition, processing, and analysis routines were tackled by addressing the following hypotheses:

1. Introduction of contrast agents and control of knee pose with a positioning device during microCT acquisition allows reproducible and accurate *in situ* QMA of cartilage and joint.

2. Automating the image processing pipeline through morphological representation using spherical harmonics improves the efficiency and reproducibility of joint QMA.

3. An empirical probabilistic approach provides an automatic and model-invariant solution to statistically capture morphological changes due to OA by detecting osteophyte activity.

In response to the first hypothesis, a whole animal positioning device and a cationic contrast agent injection protocol were developed for *in situ* microCT morphological assessments of the mouse knee. By securing the mouse using the device for consistent landmark location and limb stabilisation, high reproducibility of joint QMA results was achieved. Combined with the optimised contrast agent injection protocol, accurate measurements of cartilage attenuation and QMA were concurrently observed.

Addressing the second hypothesis, an automatic workflow based on spherical harmonics and persistent homology was developed to process the acquired microCT images for joint QMA. Spherical harmonics, describing the basic shape of the tibia, were used to align the joint to a common reference coordinate system. Anatomically meaningful subdivision of the joint into

lateral and medial volume of interests was subsequently performed using a watershed method based on persistent homology. Validated on microCT scans of rabbit and rat knees, joint QMA results from images processed through the automated workflow show excellent reproducibility with significantly reduced time and personnel training requirements compared to manual processing.

Tackling the final hypothesis, an empirical probabilistic approach was developed for an automatic and model-invariant QMA of osteophyte activity. Osteophyte disrupts the integrity of the cortical exterior, leading to a rougher surface with smaller local thickness values. The method statistically captures these changes by identifying shifts in local thickness as an indicator of osteophyte activity. Validated on microCT datasets of rabbit and rat knees, the method and the resulting models were shown to be objective and invariant to animal scale. Using this approach, reproducibility can be maintained across studies by removing the need for parametric recalibrations to adjust for animal scale and voxel size.

As these approaches are invariant to animal scale and voxel size, the need for recalibration in subsequent studies has been removed. By improving the acquisition, processing, and analysis protocols, this work increases the reproducibility and efficiency of QMA workflows, leading to higher throughput and more dynamic QMA outcomes.

Declaration

This is to certify that:

• the thesis comprises only my original work towards the PhD;

• due acknowledgement has been made in the text to all other material used;

• the thesis is fewer than 100,000 words in length, exclusive of tables, maps, bibliographies and appendices.

Pholpat Durongbhan

July 2023

Preface

This thesis was completed at the Department of Biomedical Engineering, Faculty of Engineering and Information Technology, the University of Melbourne. Data used in Chapter 4 was acquired at the University of Melbourne with approvals from the Melbourne University Animal Ethics Committee (AEC# 1614078). The datasets used in Chapter 5 and 6 were obtained in previous studies supported by the Swiss Commission for Technology and Innovation CTI (Grant No. 9853.1) and approved by the Cantonal Ethics Commission of Bern (Permit Number: 49/10).

This is a thesis with publications. Chapters 3 to 6 are author-accepted versions of the manuscripts with minor formatting according to the University of Melbourne guidelines. The publication detail, status, and author contribution statement (CRediT format) are as follows:

- Chapter 3: **P. Durongbhan**, J. W. MacKay, J. E. Schadow, C. E. Davey, K. S. Stok. "Quantitative morphometric analysis in tibiofemoral joint osteoarthritis imaging: a literature review." doi.org/10.1016/j.ostima.2023.100088
  (Published by *Osteoarthritis Imaging*, March 2023)
  PD: Data curation**,** Writing - original draft preparation. PD, CED, KSS: Formal analysis. PD, KSS: Visualisation. CED, KSS: Supervision. All authors: Conceptualisation, Writing - review & editing.

- Chapter 4: **P. Durongbhan**, M. O. Silva, Z. Li, N. Ansari, R. Y. Nigel Kour, C. E. Davey, K. S. Stok. "A microCT imaging protocol for reproducible and efficient quantitative morphometric analysis (QMA) of joint structures of the *in situ* mouse tibio-femoral joint." doi.org/10.1016/j.bone.2022.116606
  (Published by *Bone*, January 2023)
  KSS: Conceptualisation, Methodology. MOS, NA, ZL, NK: Investigation. PD: Software. PD, ZL, KSS: Data curation, Validation, Writing - original draft preparation. PD, MOS, ZL, CED, KSS: Formal analysis. CED, KSS: Supervision. All authors: Writing - review & editing.

- Chapter 5: **P. Durongbhan**, C. E. Davey, K. S. Stok. "SPHARM-PDM based image preprocessing pipeline for quantitative morphometric analysis (QMA) for in situ joint assessment in rabbit and rat models." doi.org/10.1038/s41598-021-04542-8
  (Published by *Scientific Reports*, January 2022)
  PD, CED, KSS: Conceptualisation, Methodology. PD: Data curation, Software, Validation**,** Writing - original draft preparation. KSS: Resources. KSS, CED: Supervision. All authors: Formal analysis, Writing - review & editing.

- Chapter 6: **P. Durongbhan**, C. E. Davey, K. S. Stok. “Automatic, objective, and resolution invariant approach for quantitative assessment of osteophyte in rabbit and rat trauma models of osteoarthritis.”
  (In progress)
  PD, CED, KSS: Conceptualisation, Methodology. PD: Data curation, Software, Validation, Writing - original draft preparation. KSS: Resources. KSS, CED: Supervision. All authors: Formal analysis, Writing - review & editing.

The candidate is the primary author of all these manuscripts and contributed more than 50% of all work. The candidate’s general contribution focuses on the conceptualisation, design, data curation, software development and validation, image processing, statistical analysis, and manuscript write-up and revision. All authors contributed their relevant expertise, critically revised all manuscripts for important intellectual content and provided final approval of the version to be published. No work was carried out by the candidate prior to enrolment, and no work has been submitted for other qualifications. Beyond manuscript revisions made by co-authors listed above, no third party editorial assistance was involved.

This degree was funded through the University of Melbourne Research scholarship, the Discovery Projects scheme of the Australian Research Council (DP180101838), the Open and Reproducible Musculoskeletal Imaging Research Community Travel Grant, the Christine and T. Jack Martin Research Travel Grant of the Australian & New Zealand Bone & Mineral Society, the W. E. and C. H. H. Cook Memorial Award, and the Argus Research Scholarship in Engineering of the University of Melbourne.

Additionally, the following list summarises other co-authored manuscripts made during this degree. In these works, the candidate’s contribution was on applying image processing tools developed in this thesis and manuscript revision.

- H. Liu, **P. Durongbhan**, M. O. Silva, J. Gregory, C. E. Davey, K. S. Stok, “In vivo microCT imaging allows assessment of the microstructural properties of subchondral bone remodelling using image registration.”
  (In progress)

- H. Liu, **P. Durongbhan**, M. O. Silva, J. E. Schadow, C. E. Davey, K. S. Stok, "Micro-computed tomography reveals early bone structural changes in osteoarthritis progression in a collagenase-induced mouse model."
  (In progress)

- H. Liu, **P. Durongbhan**, C. E. Davey, K. S. Stok, "Image Registration in Longitudinal Bone Assessment using Computed Tomography." doi.org/10.1007/s11914-023-00795-6
  (Published by *Current Osteoporosis Reports*, June 2023)

- B. A. Besler, J. E. Schadow, **P. Durongbhan**, T. H. Steiner, R. J. Choo, M. A. Zulliger, M. Wilke, K. Atal, C. Firminger, A. Quintin, B. Koller, R. Müller, D. Nesic, K. S. Stok, "Quantitative Measures of Bone Shape, Cartilage Morphometry and Joint Alignment are Associated with Disease in an ACLT and MMx Rat Model of Osteoarthritis." doi.org/10.1016/j.bone.2021.115903
  (Published by *Bone*, May 2021)

Lastly, the following list shows, in reverse chronological order, all poster and oral presentations involving the candidate during the course of this doctoral training:

- **P. Durongbhan**, H. Liu, J. E. Schadow, E. Boersma, K. S. Stok, "A longitudinal imaging protocol for 3D quantitative morphometric analysis of the mouse knee," *17th International Workshop on Osteoarthritis Imaging (IWOAI)*, 28-30 June 2023, Lausanne, Switzerland.

- **P. Durongbhan**, C. E. Davey, K. S. Stok, "A model-invariant approach for 3D assessment of structural changes in preclinical animal models of OA," *17th International Workshop on Osteoarthritis Imaging (IWOAI)*, 28-30 June 2023, Lausanne, Switzerland.

- **P. Durongbhan**, H. Liu, M. O. Silva, J. E. Schadow, R. Y. N. Kour, C. E. Davey, K. S. Stok, "A microCT imaging protocol for longitudinal assessment of 3D joint quantitative morphometric analysis (QMA) of the mouse knee," *9th World Congress of Biomechanics*, 10-14 July 2022, Taipei, Republic of China.

- **P. Durongbhan**, C. E. Davey, K. S. Stok, "Quantification of cortical bone surface remodelling of the tibio-femoral joint in a rat osteoarthritis model," *23rd International Workshop on Quantitative Musculoskeletal Imaging (QMSKI)*, 13-17 June 2022, Noordwijk, the Netherlands.

- H. Liu, J. E. Schadow, **P. Durongbhan,** M. O. Silva, K. S. Stok, "Three-Dimensional Quantitative Morphometric Analysis (QMA) for Longitudinally Tracking Tibiofemoral Microstructure in a Preclinical Mouse Model," *ESA-SRB-ANZBMS 2021*, 22-24 November 2021, Conference held virtually.

- **P. Durongbhan**, M. O. Silva, J. E. Schadow, K. S. Stok, "Time-Lapse Quantitative Characterisation of Whole-Joint Morphometric Changes in a Collagenase-Induced Osteoarthritis Mouse Model," *ESA-SRB-ANZBMS 2021*, 22-24 November 2021, Conference held virtually.

- M. O. Silva, **P. Durongbhan**, J. E. Schadow, K. S. Stok, "Micro-Computed Tomography Reveals Early Bone Structural Changes in Osteoarthritis Progression in a Collagenase-Induced Mouse Model," *ESA-SRB-ANZBMS 2021*, 22-24 November 2021, Conference held virtually.

- M. S. B. Rathnayake, M. A. Boos, **P. Durongbhan**, K. S. Stok, "A Novel Image-Guided Micromechanical Evaluation Method to Study Cell-Matrix Development in Tissue-Engineered Constructs," *6th World Congress of the Tissue Engineering and Regenerative Medicine International Society*, 15-19 November 2021, Conference held virtually.

- **P. Durongbhan**, M. O. Silva, N. Ansari, R. Y. N. Kour, C. E. Davey, K. S. Stok, "A Novel Micro-Computed Tomography Imaging Protocol for Reproducible Quantitative Morphometric Analysis (QMA) of the Mouse Knee," *2021 ANZORS Annual Scientific Conference*, 6-8 October 2021, Conference held virtually.

- **P. Durongbhan**, C. E. Davey, K. S. Stok, "Robust Alignment of Rabbit and Rat Joint Scans for Preclinical Osteoarthritis Studies," *26th Congress of the European Society of Biomechanics*, 11-14 July 2021, Conference held virtually.

- **P. Durongbhan**, C. E. Davey, K. S. Stok, "Joint Alignment Software for Efficient and High-Quality 3D Quantitative Morphometric Analysis in Preclinical Rabbit and Rat," *2021 OARSI Virtual World Congress*, 29 April – 3 May 2021, Conference held virtually.

- M. O. Silva, **P. Durongbhan**, K. S. Stok, "Micro-Computed Tomography Reveals Structure Changes in an Induced Model of Osteoarthritis," *2019 Melbourne Mechanobiology Symposium*, 7-8 November 2019, Melbourne, Australia.

- M. O. Silva, **P. Durongbhan**, K. S. Stok, "Imaging Porous Channels in the Osteochondral Interface: Investigating a Nanoparticle-Based Contrast Agent," *Biomed Link 2019*, 6 November 2019, Melbourne, Australia.

Acknowledgement

I would have laughed if you had asked me at the end of 2017 whether I would contemplate writing another thesis within this lifetime. I am now laughing, in 2023, at my old self for brushing off the idea of a doctoral degree so quickly. I still find it surreal to be wrapping up another thesis since, and I could not have done it without the support of many people.

First and foremost, I thank my principal supervisor, Associate Professor Kathryn Stok, to whom I owe a great debt. Thank you for having faith in my abilities and skills at a time when others have not; for offering me opportunities to engage in many exciting works throughout my PhD; and for constantly looking out for me throughout these past years. It has been a great pleasure working under your supervision. With your guidance and encouragement, I can genuinely see how I have grown as a researcher and as a person.

I also want to express my deep gratitude to my co-supervisor, Dr Katie Davey, whose contribution has shaped a significant part of my PhD. Thank you for offering me the chance to put my electrical engineering background to good use and for your persistence and patience when it comes to my work. I also thank Professor Anthony Burkitt for being the chair of my advisory committee and for being supportive through my review meetings.

My experience would not have been completed without all my friends at the office. Thank you: Manula and Mateus for paving the path towards PhD completion at our research group; Manuela, Jemima, and Nil for being my voice of reason; Rui, Long, and Hanna for always helping me out whenever I needed; and Emma and Mil for the intellectually stimulating discussions we regularly had. It was fantastic experience working and learning from you all.

To my collaborators: Dr Tor Hildebrand and Peter Suter at Lucid Concepts AG, thank you for your kind and generous software support through XamFlow; and to Dr Serena Bonaretti, thank you for supporting me and for your motivating leadership at the ORMIR community.

To my inspiring teachers: Miss Kornkanok Srimanta, Professor Jitkomut Songsiri, and Professor Yifan Zhao, thank you for being a role model and for showing me how exciting research can be; and to Master Firmin Lee for making me the proficient writer I am today.

Beyond the office, lab, and classrooms, I would like to thank my friends from near and far. To the Monday Social Club: P-Sunt, P-Oey, P-Nan, P-Meaw, P-Kris, P-Pax, and P-Fon, thank you for making my life in Melbourne vibrant and lively. To all my friends: Pok, Anne, Team, Goody, Pea, P-Koko, and Park, thank you for always being there for me. And to Coach Ian, for being a great friend and for helping me build the mental and physical capacity to get through this degree, thank you.

My degree is funded by the University of Melbourne, the Australian Research Council, and by extension, the Australian taxpayers, to whom I also owe my thanks.

Finally, I want to thank my family for their kindness. To my partner, my sister, my aunt, and my grandmother, thank you. To my parents, I hope I have made you proud; I would not have managed to get through without your additional financial and mental support. It has not always been easy being around a workaholic who is constantly consumed by work, and for your patience and love, I thank you.

It was not easy to complete a PhD in a foreign country while going through a global pandemic. With everyone's kind support and encouragement, I managed to push through – and for that, I am truly grateful.

Table of contents

List of figures[1]

[1] Figures containing third party copyrighted materials are denoted by an asterisk (*); all permissions have been obtained for reuse in this thesis.

List of tables

List of key abbreviations

CA4+	cationic iodinated contrast agent for contrast-enhanced microCT
CI	confidence interval
L	lateral
M	medial
microCT	micro-computed tomography
MLE	maximum likelihood estimates
MRI	magnetic resonance imaging
NO	contralateral control (non-operated) joint
NS	sample without osteophyte
OA	osteoarthritis
OARSI	Osteoarthritis Research Society International
OP	operated joint
OS	sample with osteophyte
PDM	point distributed model
QMA	quantitative morphometric analysis
SPHARM	spherical harmonic description method
SSM	statistical shape modelling
VOI	volume of interest

List of key parameters

Cg.At	mean cartilage attenuation (mg HA/ccm)
Cg.S	cartilage surface area (mm^2)
Cg.S/Cg.V	cartilage surface-to-volume ratio (mm^{-1})
Cg.Th	cartilage thickness (µm)
Cg.V	cartilage volume (mm^3)
Ct.Po	cortical porosity (%)
Ct.Th	cortical thickness (µm)
ICC	intraclass correlation coefficient
NRMSE	mean-normalised root-mean-squared error (%)
PE(%CV)	precision error (percent coefficient of variation) (%)
PE(SD)	precision error (standard deviation)
RMSE	root-mean-squared error
JSW	mean joint space width (µm)
JSV	joint space volume (mm^3)
α	angle in the XZ plane of the vector connecting the centre of mass of the tibia to the femur (°)
β	angle in the YZ plane of the vector connecting the centre of mass of the tibia to the femur (°)
γ	angle in the XY plane of the vector connecting the centre of mass of the tibia to the femur (°)
λ	magnitude of the vector connecting the centre of mass of the tibia to the femur (mm)

χ	distance travelled to first contact when virtually loading the femur onto the tibia (mm)
m	rate of increase of contact area under virtual loading (mm^2/mm)
k	shape parameter of the Gamma distribution
θ	scale parameter of the Gamma distribution

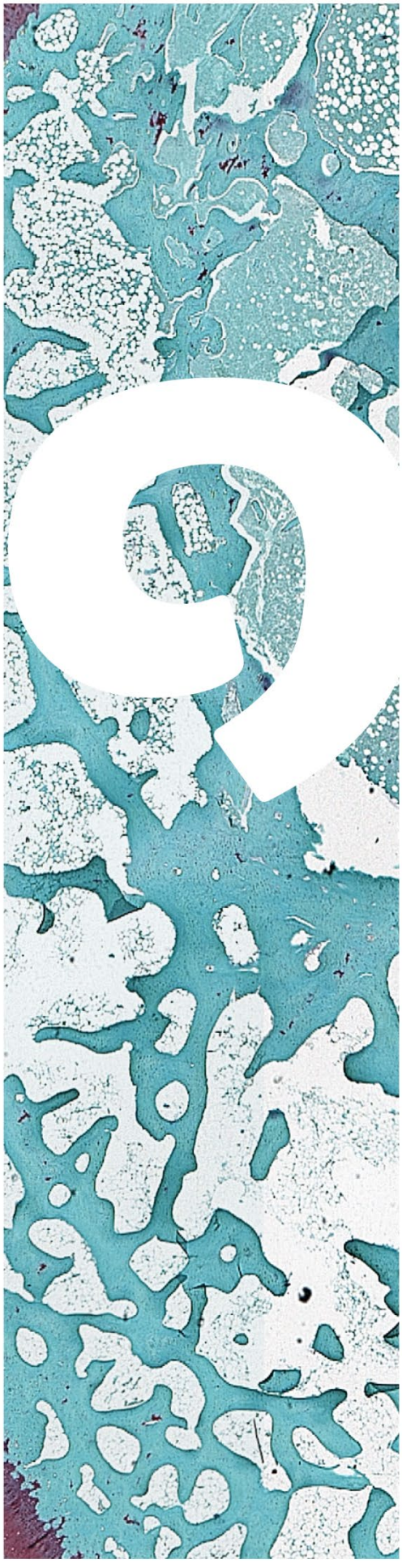

Chapter 1
Introduction

Chapter 1

1.1 Quantitative imaging in preclinical research of osteoarthritis

Medical imaging allows the non-invasive assessment of structural changes in chronic musculoskeletal diseases such as osteoarthritis (OA) [1]. Mainly affecting the knee, OA is characterised by structural degradation and abnormal remodelling of joint tissues such as cartilage and bone [2], which can be replicated and observed in preclinical imaging studies. Experimental knee OA can be induced in rabbits, rats, and mice, from which disease progression and therapeutic mediation can be monitored using 3D imaging modalities [3].

Magnetic resonance imaging (MRI) is often used in OA research for cartilage assessment [4]. However, recent studies have shown that subchondral bone changes are often the first detectable alterations which are hard to visualise with MRI [5]. Bone morphometry assessment in small animals can be done using micro-computed tomography (microCT), which offers micrometre resolutions and is the current gold standard [6]. Traditionally unable to clearly visualise cartilage and soft tissues due to poor attenuation, the introduction of contrast agents has dramatically improved the visualisation of cartilage in microCT [7]–[10]. This has created new opportunities where all relevant OA structural changes, both in the bone and cartilage, can be assessed using a single imaging modality.

Structural alterations of joint tissues can be examined through quantitative morphometric analysis (QMA) of the acquired contrast-enhanced microCT images. Recent studies have shown that morphological measures of the cartilage and bone are sensitive to OA in rabbit and rat models, with whole-joint features, such as joint space width and joint alignment, also shown to provide sensitive markers of OA biomechanical changes [11], [12].

As elastic links capable of complex motion, each joint components (i.e., femur and tibia) can move relative to one another, and differences in joint pose during image acquisition can influence measurement results [13]. Combined with subsequent processing tools and analysis pipelines that traditionally rely on manual expertise and parametric tuning between studies, QMA results often encounter reproducibility issues which are technically challenging and time-consuming to tackle.

1.2 Thesis objectives and outline

The overall aim of this thesis is to examine how improvements in image processing protocols can lead to reproducible and dynamic quantitative analysis of joint morphology. In this work, reproducibility issues in the acquisition, processing, and analysis routines are tackled by addressing the following hypotheses:

1. Introduction of contrast agents and control of knee pose with a positioning device during microCT acquisition allows reproducible and accurate *in situ* QMA of cartilage and joint.

2. Automating the image processing pipeline through morphological representation using spherical harmonics improves the efficiency and reproducibility of joint QMA.

3. An empirical probabilistic approach provides an automatic and model invariant solution to statistically capture morphological changes due to OA by detecting osteophyte activity.

To address these hypotheses, the following research aims were formulated and will form the basis of this doctoral work:

Aim 1: Develop a whole animal positioning device and a cationic contrast agent injection protocol for *in situ* microCT morphological assessment of the mouse knee.

Aim 2: Develop an automatic workflow based on spherical harmonics and persistent homology to process microCT images for joint QMA.

Aim 3: Develop an empirical probabilistic approach for an automatic and invariant QMA of osteophyte activity.

This thesis begins by briefly providing some fundamental concepts and background information in **Chapter 2**. As QMA is a broad and active research area involving multiple imaging modalities and computational methods, **Chapter 3** presents a literature review of commonly used QMA methods for structural assessment of OA in MRI and computed tomography (CT) studies. The review discusses QMA of cartilage, subchondral bone, and the joint as a whole unit by describing various metrics and their measurement techniques while providing a perspective on how the research field could benefit from open-source and reproducible coding practices. **Chapter 4** presents a contrast-enhanced microCT image acquisition protocol for *in situ* QMA of the mouse knee using the developed positioning device

and contrast agent injection routine (Aim 1). **Chapter 5** introduces an automatic image processing pipeline, using spherical harmonics for morphological representation, for reproducible and efficient joint QMA (Aim 2). **Chapter 6** describes the developed novel empirical probabilistic approach for QMA of osteophyte activity using 3D thickness transform and empirical distribution fitting (Aim 3). **Chapter 7** provides a concluding synthesis of the thesis achievements, highlighting the innovations, limitations, and future directions of this research work.

References

[1] A. Guermazi, D. Hayashi, F. W. Roemer, and D. T. Felson, "Osteoarthritis: A Review of Strengths and Weaknesses of Different Imaging Options," *Rheum. Dis. Clin. North Am.*, vol. 39, no. 3, pp. 567–591, 2013, doi: 10.1016/j.rdc.2013.02.001.

[2] D. B. Burr and M. A. Gallant, "Bone remodelling in osteoarthritis," *Nat. Rev. Rheumatol.*, vol. 8, no. 11, pp. 665–673, Nov. 2012, doi: 10.1038/nrrheum.2012.130.

[3] T. M. Piscaer, G. J. V. M. Van Osch, J. A. N. Verhaar, and H. Weinans, "Imaging of experimental osteoarthritis in small animal models," *Biorheology*, vol. 45, no. 3–4, pp. 355–364, Jan. 2008, doi: 10.3233/BIR-2008-0482.

[4] A. Guermazi *et al.*, "Imaging in Osteoarthritis," *Rheum. Dis. Clin. North Am.*, vol. 34, no. 3, pp. 645–687, 2008, doi: 10.1016/j.rdc.2008.04.006.

[5] R. J. Lories and F. P. Luyten, "The bone–cartilage unit in osteoarthritis," *Nat. Rev. Rheumatol. 2010 71*, vol. 7, no. 1, pp. 43–49, Dec. 2010, doi: 10.1038/nrrheum.2010.197.

[6] M. L. Bouxsein, S. K. Boyd, B. A. Christiansen, R. E. Guldberg, K. J. Jepsen, and R. Müller, "Guidelines for assessment of bone microstructure in rodents using micro-computed tomography," *J. Bone Miner. Res.*, vol. 25, no. 7, pp. 1468–1486, Jun. 2010, doi: 10.1002/jbmr.141.

[7] B. A. Lakin, D. J. Ellis, J. S. Shelofsky, J. D. Freedman, M. W. Grinstaff, and B. D. Snyder, "Contrast-enhanced CT facilitates rapid, non-destructive assessment of cartilage and bone properties of the human metacarpal," *Osteoarthr. Cartil.*, vol. 23, no. 12, pp. 2158–2166, Dec. 2015, doi: 10.1016/j.joca.2015.05.033.

[8] L. N. M. Hayward, C. M. J. de Bakker, L. C. Gerstenfeld, M. W. Grinstaff, and E. F. Morgan, “Assessment of contrast-enhanced computed tomography for imaging of cartilage during fracture healing,” *J. Orthop. Res.*, vol. 31, no. 4, pp. 567–573, Apr. 2013, doi: 10.1002/jor.22265.

[9] M. A. Boos, M. W. Grinstaff, S. R. Lamandé, and K. S. Stok, “Contrast-Enhanced Micro–Computed Tomography for 3D Visualization and Quantification of Glycosaminoglycans in Different Cartilage Types,” *Cartilage*, vol. 13, no. 2_suppl, pp. 486S-494S, Dec. 2021, doi: 10.1177/19476035211053820.

[10] B. A. Lakin *et al.*, “Contrast-enhanced CT using a cationic contrast agent enables non-destructive assessment of the biochemical and biomechanical properties of mouse tibial plateau cartilage,” *J. Orthop. Res.*, vol. 34, no. 7, pp. 1130–1138, Jul. 2016, doi: 10.1002/jor.23141.

[11] K. S. Stok *et al.*, “Three-Dimensional Quantitative Morphometric Analysis (QMA) for In Situ Joint and Tissue Assessment of Osteoarthritis in a Preclinical Rabbit Disease Model,” *PLoS One*, vol. 11, no. 1, p. e0147564, Jan. 2016, doi: 10.1371/journal.pone.0147564.

[12] B. A. Besler *et al.*, “Quantitative measures of bone shape, cartilage morphometry and joint alignment are associated with disease in an ACLT and MMx rat model of osteoarthritis,” *Bone*, vol. 146, p. 115903, Feb. 2021, doi: 10.1016/j.bone.2021.115903.

[13] S. Boutroy *et al.*, “Importance Of Hand Positioning In 3D Joint Space Morphology Assessment,” *Arthritis Rheum. Rheum.*, vol. 65, pp. S840–S841, 2013.

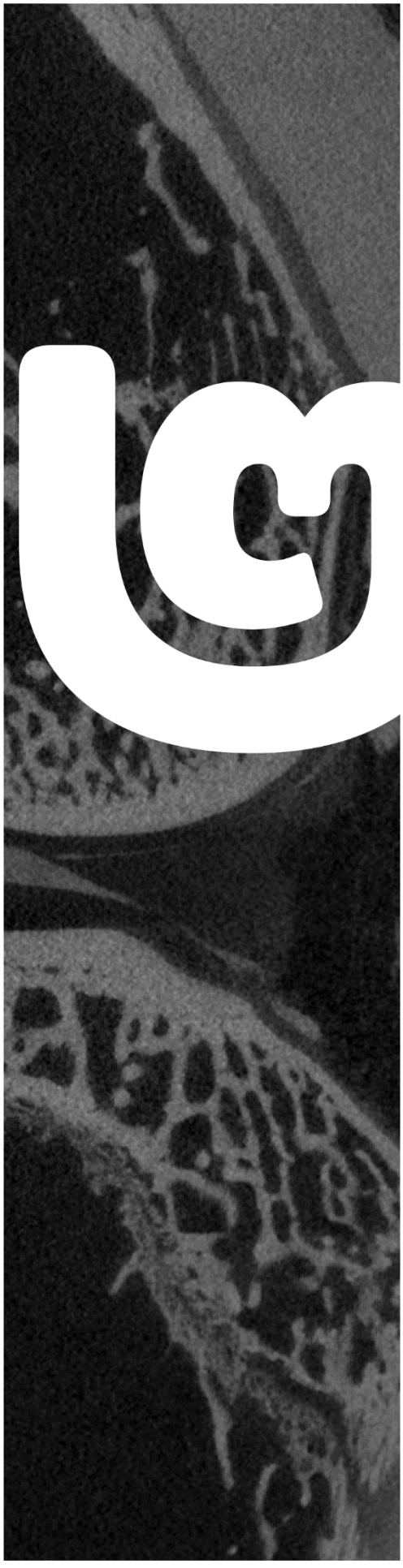

Chapter 2
Background

Chapter 2

2.1 Introduction

This chapter aims to provide background knowledge to aid readers in their understanding of this thesis. Fundamental information relevant to the image acquisition, processing, and analysis methods used in this work is described here in brief.

2.2 Image acquisition

2.2.1 Animal models of osteoarthritis (OA)

Osteoarthritis (OA) is the most widespread musculoskeletal disease in the world, affecting millions of people worldwide. Mainly affecting the knee, OA is a complex chronic disease that develops progressively over decades, affecting all structures of the synovial joint through tissue degeneration, abnormal bone remodelling, cartilage loss, and synovial inflammation, with joint failure as its final outcome [1]. Commonly considered to be a passive wear-and-tear disease, studies have demonstrated that OA is an active and dynamic disease resulting from an imbalance between repair and destruction of joint tissues [2]. Despite recent advances, the exact biochemical and biomechanical pathways leading to OA remains elusive, and more research remains to be done.

Preclinical research using small animal models of OA allows the scale and progression of joint damage to be replicated such that disease detection, observation of progression, and modulation of symptoms can be performed within a shorter period of time [3]. Currently, multiple animal models are available to replicate both primary (spontaneous) and secondary (trauma) OA in humans, each with their own benefits and limitations [4]. While spontaneous OA progression has been described in a number of species, especially in genetically modified mice strains, OA in these models often proceeds slowly and tends to be more variable in the outcomes, resulting in costly studies in terms of time and animal involved [5]. Alternatively, experimental trauma OA can be induced in small animals through surgical interventions in the knee, such as anterior cruciate ligament or medial collateral ligament transection, meniscectomy, and the introduction of meniscal tear, leading to joint instability and OA

development [4]. Trauma OA can also be induced chemically through intra-articular injection of compounds such as papain, collagenase, and monosodium iodoacetate, which alters homeostasis and leads to the destruction of joint structures and induction of OA [4].

Small animals are often used to investigate basic pathophysiology and to screen for therapeutic interventions before translation to large animal models and subsequent human clinical trials [6]. Advantages of small animal models include relatively low cost, ease of handling and housing, and rapid development and progression of OA [6]. Rats, mice, guinea pigs, and rabbits are commonly used [7]. These animal models are generally observed through destructive histological methods and biochemical assays, which are time-consuming and detrimental to animal welfare as large numbers are needed to follow the disease progression over time [7]. Recent developments of new high-resolution imaging technologies have enabled longitudinal *in vivo* observation of disease progression in each individual small animal. Biochemical changes can be monitored using high-resolution positron emission tomography or fluorescence techniques, while structural and biomechanical changes can be monitored using high-field magnetic resonance imaging (MRI) or micro-computed tomography (microCT) [7].

2.2.2 Micro-computed tomography (microCT)

MicroCT is a 3D non-invasive and non-destructive imaging technique that takes multiple X-ray projection images at different angles and applies tomographic reconstruction algorithms to produce the final 3D model [8]. A higher-resolution variant of the computed tomography (CT) modality, microCT offers micrometre resolutions that make it ideal for structural assessments in small animals where subchondral trabecular bone and cartilage thickness are in submillimetre ranges [6], [9].

The relatively short imaging time and cost-effectiveness of microCT have made it a popular technique used to investigate *in vitro* specimens and *in vivo* longitudinal studies of small animals [10]. With excellent visualisation of osseous tissues, microCT is often used as the gold standard for bone density and morphological assessments [11]. Cartilage is traditionally challenging to visualise in microCT due to its weak X-ray attenuation (Figure 2-1a). However, with the assistance of radiopaque contrast agents, microCT visualisation, segmentation, and assessments of cartilage can be achieved (Figure 2-1b).

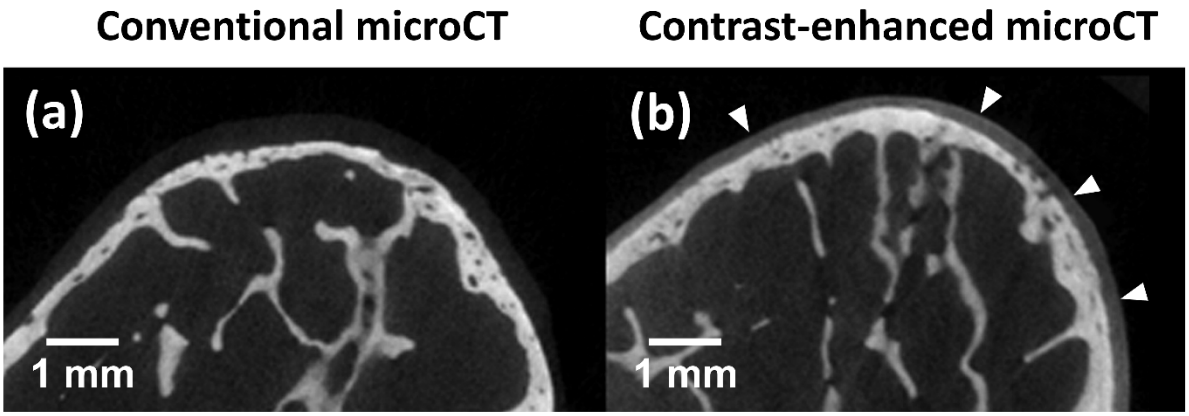

Figure 2-1: MicroCT sagittal cross-section of a human mandibular condyle before (a) and after (b) contrast enhancement. Articular cartilage (white arrow heads) showed higher attenuation owing to the immersion of anionic contrast medium (Hexabrix - ioxaglate).[2]

2.2.3 Contrast agents in microCT imaging

Contrast agents allow the observation and assessment of various soft tissues in microCT. Using elements with high atomic weight for X-ray attenuation, contrast agent binds with or perfused through soft tissues, providing enhanced visualisation as a result [12]. Various heavy elements (e.g., iodine, gold, and lanthanide) can be used to synthesise contrast agents, and the resulting molecules can be separated into two general categories: non-ionic and ionic molecules [13].

Ionic contrast agents are of particular interest in preclinical research of OA, where they could be used for compositional assessment of sulphated glycosaminoglycan (sGAG) content in articular cartilage, a key marker for OA [14]. sGAG are negatively charged and, thus, are attracted to or repelled by ionic contrast agents [13]. Traditionally done through destructive biochemical and histological assays, quantification of sGAG content and assessment of cartilage morphology can now be non-invasively done using ionic contrast agents in *ex vivo* studies [15], [16].

Altogether, contrast-enhanced microCT using ionic contrast agents allows direct quantification of bone and cartilage morphology in small animal models of OA, presenting a promising image acquisition method for future *in situ* and *in vivo* investigations.

[2] Adapted from G. A. P. Renders et al. (2014) Contrast-enhanced microCT (EPIC-μCT) ex vivo applied to the mouse and human jaw joint. Dentomaxillofacial Radiology, 43(2). https://doi.org/10.1259/dmfr.20130098 [32] with permission.

2.3 Image processing

As 3D microCT images are produced, numerous pre- and post-processing steps are involved to further improve their quality and consistency for further analysis. The processing workflow can be highly nonlinear, where the operations involved vary based on study objectives.

This thesis presents an automatic image processing workflow based on joint morphology, where techniques such as point distributed model (PDM) based on spherical harmonic description (SPHARM), statistical shape modelling (SSM), and persistent homology are used. This section describes the background of these methods in brief, and more details on how they were implemented in the workflow can be found in the respective chapters.

2.3.1 Spherical harmonic description (SPHARM)

Spherical harmonic description (SPHARM) is a mathematical framework for representing and analysing 3D shapes and surfaces. It is commonly used in computer graphics, medical imaging, and computational anatomy for tasks such as shape analysis, surface parameterisation, and surface registration. SPHARM offers a hierarchical parametric representation and global description of 3D object surfaces with spherical topology [17]. Its basic idea is to represent a 3D shape as a sum of spherical harmonics, which are orthogonal functions defined on the surface of a sphere. The spherical harmonics are used to approximate the surface of the 3D shape and capture its geometry and shape information. The coefficients of the spherical harmonics in the representation are then used to describe the shape and can be used for shape analysis and comparison.

The work presented in this thesis uses SPHARM parameterisation approach as outlined by Brechbühler et al. [17], which computes SPHARM coefficients by optimising equal area mapping of 3D voxel mesh onto a unit sphere in a separate parameter domain. The basis functions of the parameterised surface are spherical harmonics in the form of Laplace's spherical basis functions, Y_l^m, which is characterised by degree, l, and order, m. Some of the first low order terms of the described spherical harmonics are shown in Figure 2-2, where it can be seen that a higher spherical harmonics degree, l, would lead to more complex forms of basis functions, allowing more details of the objects to be represented. Conversely, by limiting the degree, l, limited details of the object would be represented.

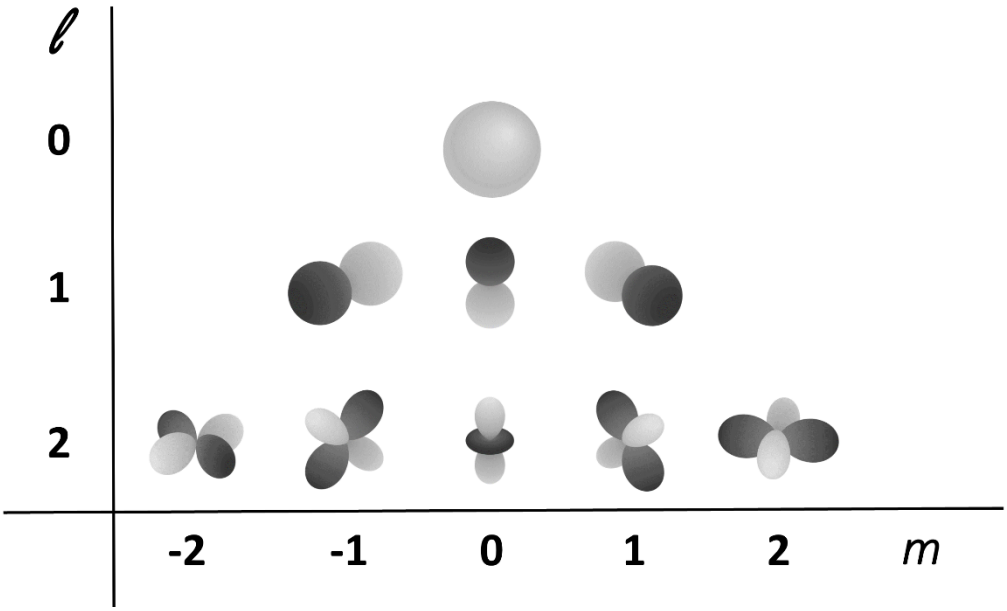

Figure 2-2: Visual representations of real spherical harmonics for the first few low values of l and m.[3]

By performing uniform icosahedron-subdivision of the spherical parameterisation, a Point Distribution Model (PDM) based on SPHARM: SPHARM-PDM can be obtained as seen in Figure 2-3 where SPHARM-PDMs of a proximal rabbit tibia are shown at different degrees, l.

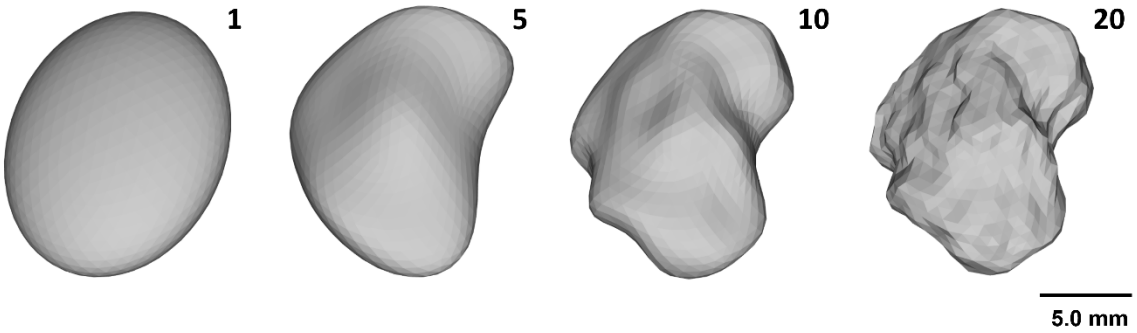

Figure 2-3: SPHARM representation of a proximal rabbit tibia at different degrees.[3]

[3] Adapted from P. Durongbhan et al. (2022) SPHARM-PDM based image preprocessing pipeline for quantitative morphometric analysis (QMA) for in situ joint assessment in rabbit and rat models. Scientific Reports, 12, 1113. https://doi.org/10.1038/s41598-021-04542-8 [33] with permission.

2.3.2 Statistical shape modelling (SSM) using SPHARM-PDM

Statistical shape modelling (SSM) is a branch of computer vision and medical image analysis that aims to quantify and model the variability of object shapes [18]. In SSM, a shape is represented as a set of landmarks or points of interest. The landmarks are chosen to be representative of the shape and are placed on the shape in a consistent manner for each shape in the dataset. The variability of the shapes is represented by a statistical distribution, which is obtained by analysing the displacement of the landmarks from a common reference coordinate system.

As a parameterisation approach, SPHARM-PDM can be used in SSM applications where each point of the PDM is used as an SSM landmark. Correspondence between the same landmark points between samples is optimised and mapped. By averaging the spatial location of each landmark, a statistical model of the object's shape is created, allowing the comparison between parameters of the model, synthesis of new shapes, or visualisation of the shape variability in each cohort. Implemented as an open-sourced framework, an SSM framework using SPHARM-PDM [19] has seen widespread adoption in studies investigating the morphometry of brain structures using MRI [20]–[25].

2.3.3 Persistent homology

Persistent homology is a method used to analyse the topology of shapes and spaces, providing a way to study the changes in the topological features of a space as a function of a parameter, such as scale, height, or resolution [26].

In this thesis, persistent homology is used to analyse the topological features of the tibial plateau. Features are identified as 'peaks' based on their 'height' measured from the base of the tibial plateau. By filtering through to lower resolutions, features corresponding to peaks are gradually eliminated, from minor to major, until none remains. Persistent homology tracks the evolution of these features throughout the process and assigns persistence values based on how long each feature persists in the filtration. Two features with the longest persistence were labelled as medial and lateral tubercles, and the minimum between peaks was identified as the intercondylar eminence (Figure 2-4).

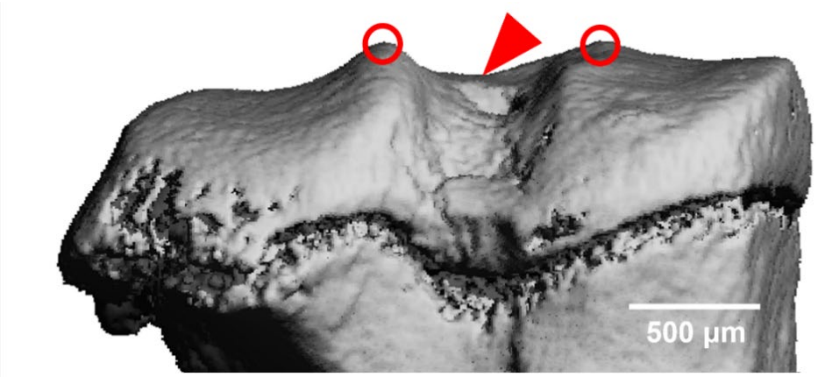

Figure 2-4: Frontal view of a mouse tibia showing medial and lateral tubercles (circled) with the highest persistence values and the identified intercondylar eminence (red arrows).

2.4 Analysis

2.4.1 Quantitative morphometric analysis (QMA)

From the processed images, a number of semi-quantitative and quantitative approaches are available for the analysis of biochemical and biomechanical changes. Quantitative analysis has the potential to be more objective and sensitive to pathological changes and often is preferable from a statistical point of view [27]. Quantitative morphometric analysis (QMA) of images extracts quantitative information about shape and structure. QMA can be used to reproducibly track the effect of OA on the morphology of joint tissues and may reveal fundamental knowledge on OA aetiology and progression, especially in early stages [28]. A number of QMA methods are available in the literature for different joint tissues and imaging methods, which are reviewed in more detail in Chapter 3.

2.4.2 Distribution fitting

In addition to traditional QMA, this work also aims to investigate how empirical probabilistic approaches, through distribution fitting, can be applied to statistically model morphological changes due to OA. Distribution fitting is a method used to model the distribution of data. The process is commonly done to model observations in the context of probability analysis to empirically determine a mathematical model and accompanying parameters that best represent the data, provide insights into its properties, and allow predictions to be made [29].

There are several types of distributions that can be used to fit data, including normal, exponential, Gamma, Poisson, and Weibull. Each distribution has specific characteristics and is appropriate for different types of data. For example, normal distributions are symmetrical and used for data that is continuous and symmetrical, while exponential distributions are used for data that represents the time between events [30].

The process of distribution fitting usually starts by choosing a set of candidate distributions and then using a statistical method, such as maximum likelihood estimation or moment matching, to estimate the parameters of the distributions. Once the parameters have been estimated, a goodness-of-fit test is used to determine which distribution fits the data best. The test compares the observed data with the predicted values generated by the model and measures the difference between them. Small differences indicate that the model is a good fit for the data [31].

This section has briefly described the processes involved in distribution fitting. An example distribution fitting result is shown in Figure 2-5 where a Gamma distribution (red line), described by shape (k) and scale (θ) parameters, is fitted to a histogram of 3D thickness values. Specific details on how the processes were applied for morphological analysis are presented in Chapter 6.

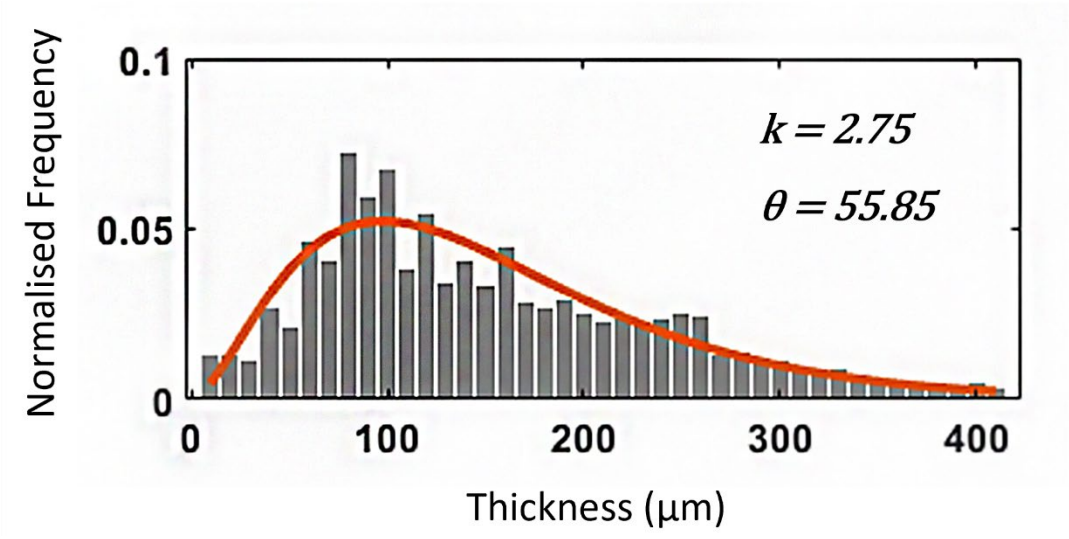

Figure 2-5: A distribution fitting result showing a Gamma distribution (red line), characterised by the specified shape (k) and scale (θ) parameters, fitted to a histogram of cortical thickness values of a rat femur.

References

[1] S. Glyn-Jones *et al.*, "Osteoarthritis," *Lancet*, vol. 386, no. 9991, pp. 376–387, 2015, doi:

10.1016/S0140-6736(14)60802-3.

[2] D. J. Hunter and S. Bierma-Zeinstra, “Osteoarthritis,” *Lancet*, vol. 393, no. 10182, pp. 1745–1759, Apr. 2019, doi: 10.1016/S0140-6736(19)30417-9.

[3] E. Teeple, G. D. Jay, K. A. Elsaid, and B. C. Fleming, “Animal Models of Osteoarthritis: Challenges of Model Selection and Analysis,” *AAPS J.*, vol. 15, no. 2, pp. 438–446, Apr. 2013, doi: 10.1208/s12248-013-9454-x.

[4] K. Lampropoulou-Adamidou *et al.*, “Useful animal models for the research of osteoarthritis,” *Eur. J. Orthop. Surg. Traumatol.*, vol. 24, no. 3, pp. 263–271, Apr. 2014, doi: 10.1007/s00590-013-1205-2.

[5] C. B. Little and D. J. Hunter, “Post-traumatic osteoarthritis: from mouse models to clinical trials,” *Nat. Rev. Rheumatol. 2013 98*, vol. 9, no. 8, pp. 485–497, May 2013, doi: 10.1038/nrrheum.2013.72.

[6] A. M. McCoy, “Animal Models of Osteoarthritis: Comparisons and Key Considerations,” *Vet. Pathol.*, vol. 52, no. 5, pp. 803–818, Sep. 2015, doi: 10.1177/0300985815588611.

[7] T. M. Piscaer, G. J. V. M. Van Osch, J. A. N. Verhaar, and H. Weinans, “Imaging of experimental osteoarthritis in small animal models,” *Biorheology*, vol. 45, no. 3–4, pp. 355–364, Jan. 2008, doi: 10.3233/BIR-2008-0482.

[8] E. L. Ritman, “Current Status of Developments and Applications of Micro-CT,” *Annu. Rev. Biomed. Eng.*, vol. 13, no. 1, pp. 531–552, Aug. 2011, doi: 10.1146/annurev-bioeng-071910-124717.

[9] M. L. Bouxsein, S. K. Boyd, B. A. Christiansen, R. E. Guldberg, K. J. Jepsen, and R. Müller, “Guidelines for assessment of bone microstructure in rodents using micro-computed tomography,” *J. Bone Miner. Res.*, vol. 25, no. 7, pp. 1468–1486, Jun. 2010, doi: 10.1002/jbmr.141.

[10] S. J. Schambach, S. Bag, L. Schilling, C. Groden, and M. A. Brockmann, “Application of micro-CT in small animal imaging,” *Methods*, vol. 50, no. 1, pp. 2–13, Jan. 2010, doi: 10.1016/j.ymeth.2009.08.007.

[11] D. W. Holdsworth and M. M. Thornton, “Micro-CT in small animal and specimen

imaging," *Trends in Biotechnology*, vol. 20, no. 8. Elsevier Current Trends, pp. S34–S39, Aug. 01, 2002, doi: 10.1016/S0167-7799(02)02004-8.

[12] S. De Bournonville, S. Vangrunderbeeck, and G. Kerckhofs, "Contrast-enhanced microCT for virtual 3D anatomical pathology of biological tissues: A literature review," *Contrast Media Mol. Imaging*, vol. 2019, 2019, doi: 10.1155/2019/8617406.

[13] H. Lusic and M. W. Grinstaff, "X-ray-computed tomography contrast agents," *Chem. Rev.*, vol. 113, no. 3, pp. 1641–1666, Mar. 2013, doi: 10.1021/CR200358S.

[14] P. Ren, H. Niu, H. Cen, S. Jia, H. Gong, and Y. Fan, "Biochemical and Morphological Abnormalities of Subchondral Bone and Their Association with Cartilage Degeneration in Spontaneous Osteoarthritis," *Calcif. Tissue Int.*, vol. 109, no. 2, pp. 179–189, Aug. 2021, doi: 10.1007/S00223-021-00834-3.

[15] B. A. Lakin *et al.*, "Contrast-enhanced CT using a cationic contrast agent enables non-destructive assessment of the biochemical and biomechanical properties of mouse tibial plateau cartilage," *J. Orthop. Res.*, vol. 34, no. 7, pp. 1130–1138, Jul. 2016, doi: 10.1002/jor.23141.

[16] M. A. Boos, M. W. Grinstaff, S. R. Lamandé, and K. S. Stok, "Contrast-Enhanced Micro–Computed Tomography for 3D Visualization and Quantification of Glycosaminoglycans in Different Cartilage Types," *Cartilage*, vol. 13, no. 2_suppl, pp. 486S-494S, Dec. 2021, doi: 10.1177/19476035211053820.

[17] C. M. Brechbühler, G. Gerig, and O. Kubler, "Parametrization of closed surfaces for 3-D shape description," *Comput. Vis. Image Underst.*, vol. 61, no. 2, pp. 154–170, Mar. 1995, doi: 10.1006/cviu.1995.1013.

[18] T. F. Cootes, D. H. Cooper, C. J. Taylor, and J. Graham, "Trainable method of parametric shape description," *Image Vis. Comput.*, vol. 10, no. 5, pp. 289–294, Jun. 1992, doi: 10.1016/0262-8856(92)90044-4.

[19] M. Styner *et al.*, "Framework for the Statistical Shape Analysis of Brain Structures using SPHARM-PDM.," *Insight J.*, no. 1071, pp. 242–250, 2006, Accessed: Mar. 06, 2020. [Online]. Available: http://www.ncbi.nlm.nih.gov/pubmed/21941375.

[20] G. Gerig, M. Styner, M. E. Shenton, and J. A. Lieberman, “Shape versus size: Improved understanding of the morphology ofbrain structures,” in *Lecture Notes in Computer Science (including subseries Lecture Notes in Artificial Intelligence and Lecture Notes in Bioinformatics)*, Oct. 2001, vol. 2208, pp. 24–32, doi: 10.1007/3-540-45468-3_4.

[21] G. Gerig, M. Styner, D. Jones, D. Weinberger, and J. Lieberman, “Shape analysis of brain ventricles using SPHARM,” in *Proceedings of the Workshop on Mathematical Methods in Biomedical Image Analysis*, 2001, pp. 171–178, doi: 10.1109/mmbia.2001.991731.

[22] B. Paniagua *et al.*, “Lateral ventricle morphology analysis via mean latitude axis,” in *Medical Imaging 2013: Biomedical Applications in Molecular, Structural, and Functional Imaging*, Mar. 2013, vol. 8672, p. 86720M, doi: 10.1117/12.2006846.

[23] M. Styner, J. A. Lieberman, D. Pantazis, and G. Gerig, “Boundary and medial shape analysis of the hippocampus in schizophrenia,” 2004, doi: 10.1016/j.media.2004.06.004.

[24] D. Nain *et al.*, “Statistical shape analysis of brain structures using spherical wavelets,” in *2007 4th IEEE International Symposium on Biomedical Imaging: From Nano to Macro - Proceedings*, 2007, vol. 4, pp. 209–212, doi: 10.1109/ISBI.2007.356825.

[25] H. Kim, T. Mansi, A. Bernasconi, and N. Bernasconi, “Vertex-Wise Shape Analysis of the Hippocampus: Disentangling Positional Differences from Volume Changes,” 2011.

[26] S. Huber, “Persistent Homology in Data Science,” *3rd Int. Data Sci. Conf. (iDSC’20)*, May 2020.

[27] A. Guermazi *et al.*, “Imaging in Osteoarthritis,” *Rheum. Dis. Clin. North Am.*, vol. 34, no. 3, pp. 645–687, Aug. 2008, doi: 10.1016/J.RDC.2008.04.006.

[28] F. Eckstein, D. Burstein, and T. M. Link, “Quantitative MRI of cartilage and bone: degenerative changes in osteoarthritis,” *NMR Biomed.*, vol. 19, no. 7, pp. 822–854, Nov. 2006, doi: 10.1002/nbm.1063.

[29] M. L. Delignette-Muller and C. Dutang, “fitdistrplus: An R Package for Fitting Distributions,” *J. Stat. Softw.*, vol. 64, no. 4, pp. 1–34, Mar. 2015, doi: 10.18637/JSS.V064.I04.

[30] R. Bono, M. J. Blanca, J. Arnau, and J. Gómez-Benito, “Non-normal distributions commonly used in health, education, and social sciences: A systematic review,” *Front. Psychol.*, vol. 8, no. SEP, p. 1602, Sep. 2017, doi: 10.3389/FPSYG.2017.01602.

[31] R. D’Agostino, *Goodness-of-Fit Techniques*. 2017.

[32] G. A. P. Renders *et al.*, “Contrast-enhanced microCT (EPIC-µCT) ex vivo applied to the mouse and human jaw joint,” *Dentomaxillofacial Radiol.*, vol. 43, no. 2, Feb. 2014, doi: 10.1259/DMFR.20130098/ASSET/IMAGES/LARGE/DMFR.20130098.G006.JPEG.

[33] P. Durongbhan, C. E. Davey, and K. S. Stok, “SPHARM-PDM based image preprocessing pipeline for quantitative morphometric analysis (QMA) for in situ joint assessment in rabbit and rat models,” *Sci. Reports 2022 121*, vol. 12, no. 1, pp. 1–12, Jan. 2022, doi: 10.1038/s41598-021-04542-8.

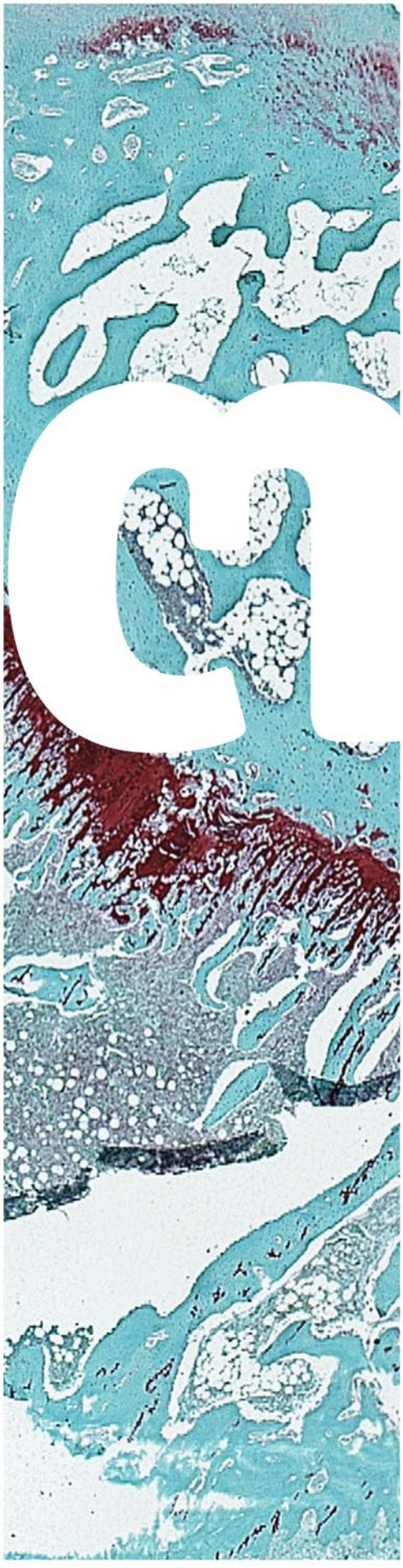

Chapter 3
Literature Review

Chapter 3

3.1 Chapter introduction

Morphometrics is a field of research focussing on examining, describing, and understanding shape and its variations in biology. Quantitative morphometric analysis (QMA) has become a fundamental methodology in clinical practice and research for diagnosing and monitoring various musculoskeletal conditions such as rheumatoid arthritis, osteoporosis, and osteoarthritis (OA). With differing strengths and drawbacks, imaging methods such as radiology, computed tomography (CT), and magnetic resonance imaging (MRI) are frequently used to quantify measurements of bone, cartilage, and joints. As an active research area covering various musculoskeletal conditions and modalities, many measurement approaches are available to assess OA. This chapter presents a broad review of QMA methods pertinent to the observation of structural changes in knee OA with a perspective on algorithm translation for reproducible QMA outcomes.

This chapter consists of the manuscript entitled "Quantitative morphometric analysis in tibiofemoral joint osteoarthritis imaging: a literature review" which has been **published** in Osteoarthritis Imaging, 3(1):100088 in March 2023.

Quantitative morphometric analysis in tibiofemoral joint osteoarthritis imaging: a literature review

https://doi.org/10.1016/j.ostima.2023.100088

Pholpat Durongbhan[1], James W. MacKay[2, 3], Jemima E. Schadow[1], Catherine E. Davey[1], Kathryn S. Stok[1]

[1]Department of Biomedical Engineering, The University of Melbourne, Parkville, Australia

[2]Department of Radiology, University of Cambridge, Cambridge, UK

[3]Norwich Medical School, University of East Anglia, Norwich, UK

3.2 Abstract

Objective: To highlight published quantitative morphometric analysis (QMA) methods for assessing tibiofemoral joint osteoarthritis in magnetic resonance imaging and computed tomography and underline the need for open and interoperable protocols for quantitative image analysis.

Design: A literature search on PubMed/MEDLINE and Web of Science of keywords relating to QMA in magnetic resonance imaging and computed tomography in the context of tibiofemoral osteoarthritis in the past 23 years (2000-2022). The search was based on, but not limited to: “quantitative morphometric analysis” or “quantitative image analysis” in combination with “osteoarthritis”, “articular cartilage”, “subchondral bone”, “tibiofemoral joint”, “joint”, “CT”, and “MRI”. The search provided 73 relevant publications that were manually screened and sorted for QMA methods. Further search to extract key functions of the underlying algorithms was performed.

Result: MRI is generally used for QMA of articular cartilage and joint contact area, while CT is generally used for QMA of subchondral bone and joint space width. Studies have shown that QMA algorithms can be adapted to new tissues and modalities. However, many methods are not easily accessible, and there exists a fragmentation of computational tools and platforms in the research field.

Conclusion: QMA is an active research area, and many techniques from one modality can be readily extended to another. Adoption of open-source practices can allow algorithms developed for other imaging modalities to be shared, making it possible to bridge the knowledge gap for structures and pathological features for which QMA has not yet been investigated and increase research output overall.

Keywords: cartilage, bone, magnetic resonance imaging, computed tomography, knee, morphometry

3.3 Introduction

Medical imaging is a powerful tool for the diagnosis and subsequent monitoring of osteoarthritis (OA). As a disease characterised by structural changes to joint tissues, advanced imaging modalities such as magnetic resonance imaging (MRI) and computed tomography (CT) can be used for non-invasive assessment of OA progression in 3D [1]. Among them, MRI, with no radiation exposure, is the imaging method of choice for evaluating cartilage, synovial, and internal derangements of the joint, while CT, with varying levels of radiation dose [2], can clearly visualise subchondral bone structure and their interaction with surrounding soft tissues [3], [4]. Conventionally, clinical MRI and CT produce images with resolutions up to 0.5 mm and are usually evaluated qualitatively alongside other markers. However, high-resolution variants such as high-field (more than 1.5 T [5]) microMRI (resolutions < 100 µm), and microCT (resolutions < 0.5 µm) are increasingly being deployed in preclinical and discovery OA research [6], [7], allowing quantitative morphometric analysis (QMA) to quantify morphological and structural changes in joint tissues with higher sensitivity than before.

The application of QMA to high-resolution data has the potential to detect small structural changes in the early stages of OA that would be difficult to detect using qualitative assessments. Longitudinal *in vivo* applications of QMA could also reveal how joint tissues remodel relative to one another, filling in fundamental knowledge gaps in OA pathophysiology. As an active research area, many works have applied QMA for OA assessment [8], and numerous QMA techniques have been proposed for multiple joint tissues. Several proposals attempted to quantify similar pathological traits in different imaging modalities, with some features having multiple measurement approaches [9], [10]. Workflows often consist of a combination of proprietary software, provided by device manufacturers, and in-house algorithms, written in a multitude of languages, leading to a fragmentation of computational tools in the field. It can be challenging for researchers to navigate and access these tools, with many groups having to reimplement their own QMA solutions based on existing literature as a result.

Currently, there are published guidelines for the acquisition and reporting of QMA metrics using MRI [9], [11], [12] and CT [10], [13], [14]. However, there is no literature review that focuses on the breadth of the field with a perspective on workflow fragmentation and algorithm adaptations to new tissues and modalities. Thus, this review aims to highlight

published QMA methods for analysing tibiofemoral joint (TFJ) OA and underline the need for open and interoperable protocols for quantitative image analysis. As the most investigated joint in OA research [15], this review will focus on highlighting QMA methods developed and applied to the TFJ. Relevant QMA applications in other joints are described if accompanying details on TFJ are scarce and translations to TFJ could be readily performed. Two widely studied tissues of the TFJ: articular cartilage and subchondral bone, as well as the gross morphology of the whole joint, are addressed in each section of this review. An introduction to the morphological changes caused by OA and relevant image acquisition and preprocessing are presented for each section. This is followed by a brief presentation of related definitions and calculation approaches of the QMA parameters. The review concludes with a perspective on QMA developments in the field of OA imaging.

3.4 Method

This paper is a narrative review of QMA methods that can be applied to the assessment of TFJ OA using MRI and CT. Included studies were identified through manual and electronic searches of literature on PubMed/MEDLINE and Web of Science, using keywords relating to QMA in the context of OA (Supplementary Table 3-S1) over the past 23 years (2000-2022). Studies using both human and animal models of OA were included, with no exclusions made regarding the *in vivo*, *in situ*, or *ex vivo* nature of those studies. As a review dedicated to morphological metrics, approaches including compositional analysis, machine learning, and artificial intelligence are not discussed.

The search revealed 73 relevant records and was completed on 20 November 2022. These were manually reviewed and categorised with respect to: imaging modality (MRI/CT), joint type, study type (preclinical/clinical), as well as QMA according to the joint structures and their reference algorithm citations. These QMA parameters and citations were used in subsequent literature searches to extract key functions of the underlying algorithms. The extracted parameters and their algorithms are further summarised and discussed.

Due to different abbreviations and nomenclature between MRI- and CT-based literature, the nomenclatures for morphological variables used in both fields are presented in brackets after their introduction in this narrative review. CT-based indices are presented first, followed by MRI-based indices. When proposals exist in one modality but not the other, only one abbreviation is presented. MRI-based nomenclature follows the proposal by Eckstein et al.

[11] for QMA performed on MRI scans. CT-based nomenclature follows the ASBMR nomenclature standard [16] for QMA parameters performed on CT images. Original abbreviations are presented if they were not covered by these guidelines. Additionally, tables listing the metrics in this review, along with the manuscript describing their calculation method in detail, are presented for each section.

3.5 QMA of articular cartilage

The progressive degeneration, manifesting as the softening, fibrillation, and erosion, of articular cartilage is a hallmark of OA. Cross-sectional studies have reported reductions in cartilage thickness, with longitudinal studies reporting progressive losses of cartilage volume during OA progression [17]. Traditionally undetectable with radiography and CT imaging techniques, articular cartilage can be visualised with these modalities using *in vivo* or *in situ* contrast agents, such as ioxaglate (Hexabrix) [18], CA4+ [19], sodium iodide (NaI) [20], and silicon oxide (SiO_2) microbeads (Figure 3-1a) [21]. On the other hand, due to its high water content, structural changes of the cartilage can be easily observed using MRI (Figure 3-1b). Segmentation of the cartilage can be challenging due to its small thickness, especially in preclinical microCT studies using small animal models of OA. Once the boundary is segmented (Figure 3-1c), QMA of the articular cartilage can be performed.

QMA of the articular cartilage is common in MRI literature [12], and there is a comprehensive system of standard definitions for the different volume of interest according to anatomical subregions, which provides a reporting guideline for cartilage QMA in MRI studies [11]. These definitions (Figure 3-1d) include medial tibia (MT), lateral tibia (LT), central lateral femoral condyle (cLF), and central medial femoral condyle (cMF) and can be applied to datasets using various methods such as mesh analysis [22], atlas mapping [23], statistical shape modelling (SSM) [24], [25], and other in-house routines [26]. There are currently no similar guidelines for CT studies of articular cartilage QMA, but regional assessments using anatomical direction (medial, lateral, anterior, posterior, etc.) are often reported.

Once the appropriate volume of interest has been selected, the calculation of cartilage volume (Cg.V, VC) is a relatively straightforward task and can be achieved by numerical integration of all segmented cartilage voxels [27], [28]. For surface-based measurements, however, surface generation using algorithms such as marching cubes [29], common in CT-

based studies (Figure 3-1e), and B-spline surface fitting, common in MRI-based studies (Figure 3-1f), must be performed prior to analysis. From the constructed surface, the overall cartilage surface area (Cg.S, AC), surface-to-volume ratio in studies using CT (Cg.S/Cg.V), volume-to-surface ratio in studies using MRI (VCtAB), and principal curvature of the cartilage surface [30] can be obtained. Additional subregions based on cartilage surface, such as total subchondral bone area (tAB), cartilage covered area of the subchondral bone (cAB), and the denuded area of the subchondral bone (dAB), can also be derived [11] (Figure 3-1d).

In addition to volume- and surface-based measurements, 3D thickness of the cartilage is also reported. Measuring thickness in 3D can be done by performing a 3D distance transform on the segmented object; however, there is a divergence in the algorithms used between CT- and MRI-based studies. CT thickness measurements are commonly derived from the 3D sphere fitting approach of Hildebrand and Rüegsegger [31] (Figure 3-1g), which was initially developed to measure thickness in bone QMA, and are usually reported as the thickness of the entire cartilage volume of interest (Cg.Th, ThC). On the other hand, MRI thickness measurements commonly use a method based on 3D Euclidean distance transform as outlined by Stammberger et al. [32] (Figure 3-1h) and can be reported in relation to cartilage surface coverage, such as thickness of the cartilage area that is inclusive (ThCtAB), or exclusive (ThCcAB), of the denuded regions.

These thickness measurement approaches can be translated between modalities. In two validation studies of cartilage thickness measurements, the 3D Euclidean distance approach [32], common in MRI studies, was applied to contrast-enhanced CT dataset by Graichen et al. [33], and the 3D sphere fitting approach [31], common in CT studies, was applied to MRI by Michalak et al. [34]. Graichen et al. [33], using scans of similar resolution, reported no significant difference in cartilage thickness measured from the two modalities in general, while the differences observed by Michalak et al. [34] were attributed to the large difference in image resolution between their MRI and contrast-enhanced high-resolution peripheral quantitative CT (HR-pQCT) images (MRI resolution: 500 µm × 500 µm × 1400 µm, HR-pQCT resolution: 61 µm × 61 µm × 61 µm). All cartilage QMA metrics presented in this section are listed in Table 3-1.

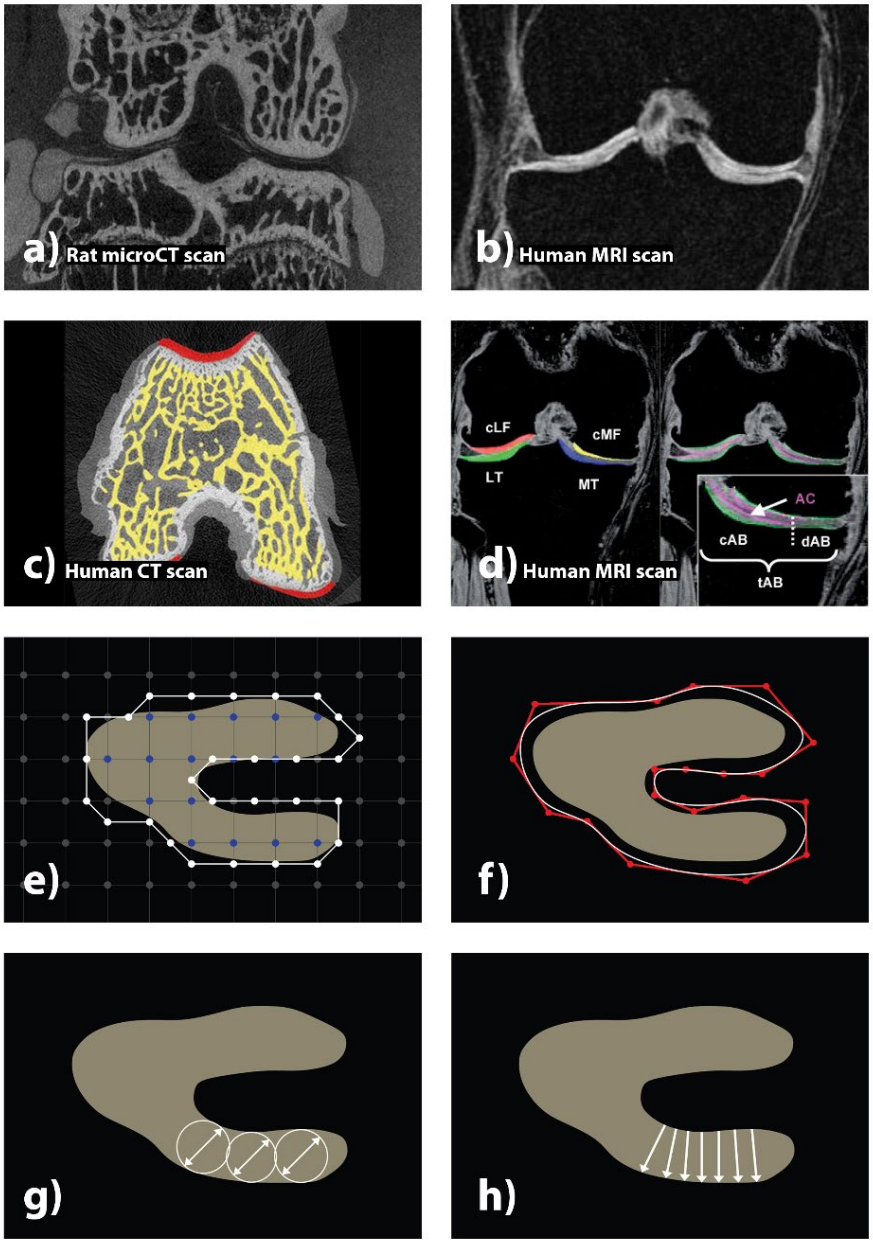

Figure 3-1: (a)[4] Coronal view of a contrast-enhanced microCT scan of the rat TFJ. (b)[5] Coronal view of a 1.5 T MRI scan of the human TFJ. (c)[6] A contrast-enhanced microCT scan showing segmented cortical bone (white), trabecular bone (yellow), and cartilage (red). (d)[4] A 3 T MRI scan showing segmented cartilage plates (left) with medial tibia enlarged (right) to highlight cartilage surface area (magenta line, AC), total surface area of the subchondral bone (green line, tAB), partially denuded area (dAB) and the area of the subchondral bone covered by cartilage (cAB). (e) Schematic of 3D surface generation using the marching cube algorithm common in CT studies [29]. *The algorithm proceeds through the scalar field (grey grid), taking eight neighbour locations (dots, blue: object, grey: background) at a time, then determining the polygons (white) needed to represent the part of the surface that passes through this cube. Individual polygons are then fused into the desired surface. (f) Schematic of surface generation using the b-spline fitting algorithm common in MRI studies. The algorithm constructs the total spline surface (white) defined from linear combinations of basis splines manipulated by control points/polygon (red). (g) Schematic of thickness measurement using 3D sphere fitting* [31] *common in CT studies where thickness is defined as the diameter of the largest sphere that can be fitted completely inside the structure. (h) Schematic of thickness measurement using 3D Euclidean distance transform* [32] *commonly used in MRI studies.*

[4] Reprinted from Bone, 146, B. A. Besler et al., Quantitative measures of bone shape, cartilage morphometry and joint alignment are associated with disease in an ACLT and MMx rat model of osteoarthritis, 115903, 2021, with permission from Elsevier. https://doi.org/10.1016/j.bone.2021.115903 [51].
[5] Reprinted from NMR in Biomedicine, 19, F. Eckstein et al., Quantitative MRI of cartilage and bone: degenerative changes in osteoarthritis, 822 – 854, 2006, with permission from John Wiley and Sons. https://doi.org/10.1002/nbm.1063 [115].
[6] Reprinted from Bone, 137, M. D. Newton et al., Automated MicroCT-based bone and articular cartilage analysis using iterative shape averaging and atlas-based registration, 115417, 2020, with permission from Elsevier. https://doi.org/10.1016/j.bone.2020.115417 [116].

Table 3-1: QMA parameters of articular cartilage

Imaging Mode Articular cartilage	Parameter	Abbrev.	Unit	Method detailed in
MRI	Volume	VC	mm^3	Peterfy et al. (1994) [27]
	Surface area	AC	cm^2	Hohe et al. (2002) [30]
	Surface curvature	-	m^{-1}	Hohe et al. (2002) [30]
	Surface area of the subchondral bone	tAB	cm^2	Eckstein et al. (2006) [17]
	Area of tAB covered by AC	cAB	cm^2	Eckstein et al. (2006) [17]
	Denuded cartilage area	dAB	cm^2	Eckstein et al. (2006) [17]
	Volume-to-surface ratio	VCtAB	mm	Eckstein et al. (2006) [17]
	Thickness	ThC	mm	Stammberger et al. (1999) [32]
	Thickness over the entire tAB	ThCtAB	mm	Eckstein et al. (2006) [17]
	Thickness over the entire cAB	ThCcAB	mm	Eckstein et al. (2006) [17]
	Cartilage homogeneity	-		Qazi et al. (2007) [35]
CT	Volume	Cg.V	mm^3	Xie et al. (2009) [28]
	Surface area	Cg.S	cm^2	Xie et al. (2009) [28]
	Surface to volume ratio	Cg.S/Cg.V	mm	Stok et al. (2016) [36]
	Thickness	Cg.Th	mm	Xie et al. (2009) [28]

Beyond cartilage measurements described above, QMA of calcified cartilage has been explored by Kauppinen et al. [37] and Rytky et al. [38], where the thickness of the calcified cartilage was investigated using microCT and 3D sphere fitting method [31]. With increasing evidence indicating that these tissues are highly interrelated [39], many cartilage QMA definitions are subsequently linked to those of the subchondral bone. As part of the same functional unit, QMA of the subchondral bone could provide complementary insights into cartilage structural changes as well.

3.6 QMA of subchondral bone

Cartilage and bone act together as a single unit to maintain joint homeostasis [40]. OA causes disruption to this balance, leading to elevated bone remodelling and bone loss in early OA, then to progressive increase in subchondral bone thickness, modification of trabecular architecture, and formation of new bone at the joint margins, i.e. osteophytes, in late-stage OA [41], [42].

As the traditional imaging method for visualising mineralised tissue, CT is the current gold standard for 3D bone structural analysis [8]. In particular, microCT has become a popular and well-established method for quantifying and analysing bone microarchitecture in preclinical studies due to its ability to clearly visualise trabecular structures [6] (Figure 3-2a). On the other hand, it is typically challenging to visualise mineralised bone using MRI due to low signal intensity and insufficient resolution for trabecular analysis [43] (Figure 3-1b).

Due to resolution limitations, some bone QMA metrics obtained using clinical MRI are evaluated using 2D stereological approaches and are described as apparent structural measures [44], [45]. However, imaging of bone structures can still be achieved using high-field microMRI and adopting different acquisition sequences to selectively capture bone signal [46] (Figure 3-2b). For comparison, a separate study has scanned the same trabecular bone sample using microCT and high-field microMRI with slice-matched images are shown in Figure 3-2c and Figure 3-2d [47]. With bone adequately visualised, it is possible to apply direct 3D measurements of bone microarchitecture to MRI-based studies [47]–[50].

With many parameters involved in the QMA of the subchondral bone, this section is divided into three suTabsections: trabecular bone parameters, cortical bone parameters, and parameters describing subchondral bone as a whole, single unit. All bone QMA parameters discussed in this section are listed in Table 3-2.

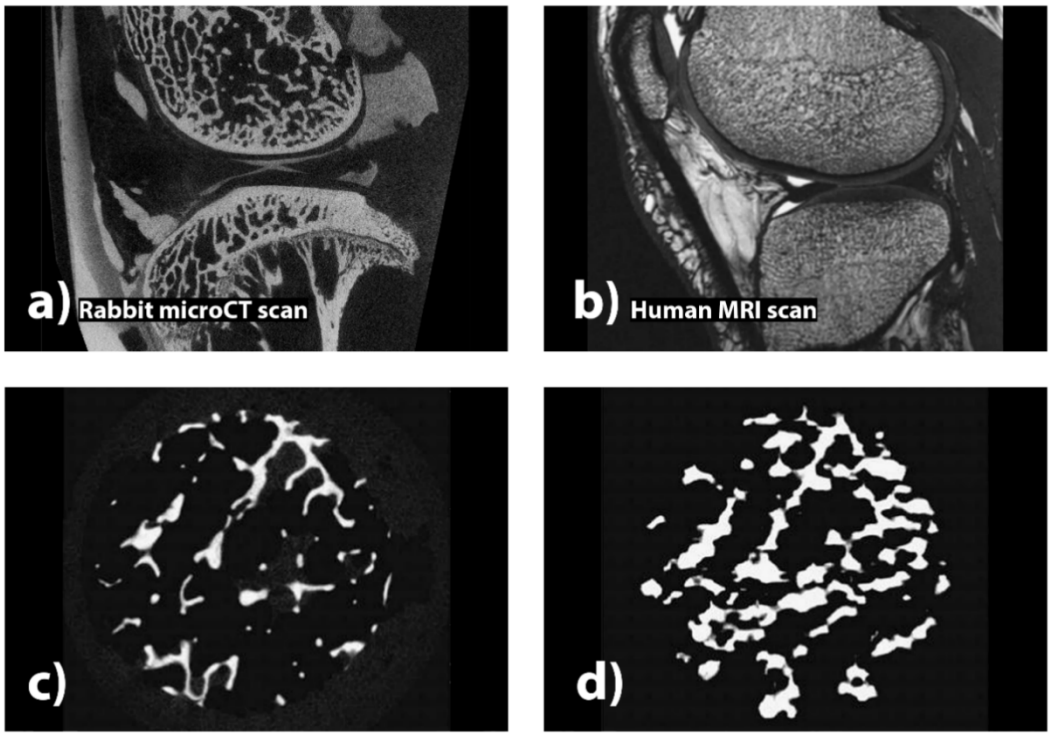

Figure 3-2: (a) Sagittal view of a contrast-enhanced microCT scan of the rabbit TFJ. (b)[7] Sagittal view of a 3 T MRI scan of the human TFJ using FIESTA-c sequence. (c)[8], (d)[8] Slice-matched, cross-sectional, grayscale images of a bone sample from the human femoral head acquired using microCT (isotropic resolution: 22 µm) and 3 MRI with FGRE sequence (in-plane resolution: 117 µm x 117 µm, axial resolution: 300 µm), respectively.

3.6.1 Subchondral trabecular bone measures

Once segmented, trabecular bone volume can be described by the numerical integration of all voxels in the volume of interest (TV) or just the bone voxels of interest to yield bone volume (BV), from which the bone volume fraction (BV/TV) can be calculated. In MRI, apparent bone volume fraction (app.BV/TV) can also be derived using the same definition [44]. For surface-based metrics, surface generation using the marching cube algorithm [29] (Figure 3-1e) is often done in CT-based studies [36], [51], [52]. Measurements such as bone surface (BS, tAB) [52] and structural model index (SMI) [53] (Figure 3-3a), which quantifies the plate and rod composition of the trabecular structure can, then, be derived from the generated surfaces.

In MRI-based studies, an approach called digital topological analysis (DTA) has been proposed by Saha et al. [54], [55]. Instead of fitting surface to volume, DTA decomposes volumetric data

[7] Reprinted by permission from Springer Nature Customer Service Centre GmbH: Springer Osteoporosis International, Osteoporotic changes of subchondral trabecular bone in osteoarthritis of the knee: a 3-T MRI study, K. Chiba et al., 2011. https://doi.org/10.1007/s00198-011-1585-2 [117].
[8] Reprinted by permission from Springer Nature Customer Service Centre GmbH: Springer Calcified Tissue International, Quantification of Trabecular Bone Structure Using Magnetic Resonance Imaging at 3 Tesla—Calibration Studies Using Microcomputed Tomography as a Standard of Reference, C. A. Sell et al., 2005. https://doi.org/10.1007/s00223-004-0111-3 [47].

into basic surface, curve, and junction (i.e. crossing) structures for analysis. Using DTA, surface parameters such as surface-to-curve ratio (SCR), erosion index (EI), and markers of trabecular number (skeleton density, Sk.D [49]) can be quantified. DTA can also be expanded to volumetric topological analysis (VTA) by applying a fuzzy distance transform [56]. With VTA, thickness-based metrics such as trabecular thickness (Tb.Th), trabecular separation, also known as trabecular spacing (Tb.Sp), the assignment of thickness to plate and rod structures detected through DTA, and measurements of plate-width (PW) and plate-to-rod ratio (PRR) can be derived [57]–[59]. This suite of measurements was shown to be translatable to multidetector row CT and cone beam microCT in a validation study by Chen et al. [60]. They found that trabecular QMA results from multidetector row CT have excellent reproducibility (intraclass correlation coefficient > 0.94) but were different to cone beam microCT results due to differing resolutions. Other MRI-based studies that use mean intercept length (MIL) also report apparent trabecular thickness (app.Tb.Th) from which apparent trabecular separation (app.Tb.Sp) and apparent trabecular number (app.Tb.N) can be derived [45].

Direct quantification of thickness is often achieved in CT-based studies using a 3D distance transform method based on sphere fitting [31]. Trabecular thickness (Tb.Th) [31] and separation (Tb.Sp) [52] can be directly quantified, as shown in Figure 3-3b and Figure 3-3c, respectively. Trabecular number (Tb.N) is calculated as the inverse of the mean 3D distance between the mid-axes of the trabecular structure, as shown in Figure 3-3d [52]. These methods were applied to high-resolution MRI data in a validation study by Laib et al. [48]. They reported that MRI measurements of trabecular number, thickness, and separation using the sphere fitting method [31] were found to be closer to baseline measurements from microCT than traditional apparent approaches.

Other parameters for trabecular morphometry include measures that quantify the connectedness of the trabecular bone as connectivity density (Conn.D) [61] in CT and trabecular bone pattern factor (TBPf) [62] and other DTA-based parameters [50] in MRI. Degree of anisotropy (DA) measures how oriented the trabecular structures are and can be evaluated in both MRI [48] and CT [52] using the mean intercept length approach [63]. While many studies have focused on reporting QMA of the trabecular structures, QMA of the cortical bone is also to reported for a more comprehensive understanding of subchondral bone changes.

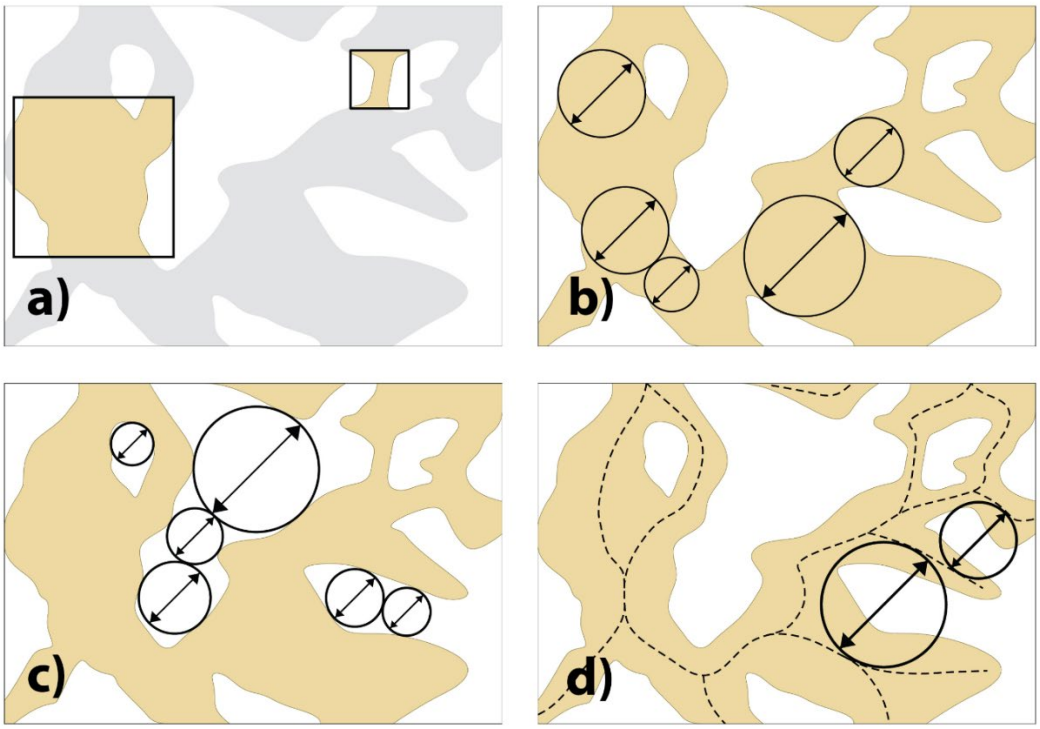

Figure 3-3: (a) Schematic highlighting plate-like (left cutout) and rod-like (right cutout) structures of the trabecular bone, the volumetric ratio of which determines the structural model index (SMI) [53]. *(b), (c), (d) Schematic highlighting applications of a 3D distance transform based on sphere fitting approach* [31] *to measure trabecular thickness (Tb.Th), trabecular separation (Tb.Sp), and trabecular number (Tb.N), respectively.*

3.6.2 Subchondral cortical bone measures

Cortical QMA metrics using CT are often evaluated at the metaphysis and diaphysis of long bones [10]. However, these approaches can also be applied to the study of the subchondral cortical bone to reveal important structural changes at the osteochondral interface [64]. Thickness-based measurements derived from the 3D sphere fitting approach [31] (Figure 3-3) are often used to evaluate cortical thickness (Ct.Th) and, where resolution is sufficient to visualise cortical pores, cortical porosity (Ct.Po), total pore volume (Ct.Po.V), pore number (Po.N), and mean cortical pore diameter (Ct.Po.Dm) [10], [65]. These parameters may be helpful in analysing the subchondral cortical bone plate where incremental vascularisation and bone remodelling activity is observed with OA [66] and could be analysed together with QMA of the calcified cartilage, as earlier described.

Other cortical metrics that exist for the analysis of the metaphysis and diaphysis can also be applied to the subchondral bone. Area measurements are reported, such as total cross-sectional area (Tt.Ar) and cortical bone area (Ct.Ar), from which the cortical bone area fraction can be derived (Ct.Ar/Tt.Ar). Even though a volume is acquired in CT, evaluating average cross-sectional geometry measurements allows for comparison across studies with scan volumes of different sizes [10].

3.6.3 Whole bone measures

Besides studies of subchondral bone microarchitecture, gross morphology analysis can also identify changes and deformation to the overall bone shape, such as osteophytes, a hallmark feature of OA. Hakky et al. [67] have developed a semi-automated method for segmenting and quantifying osteophyte volume from a longitudinal MRI dataset and quantified its volumetric changes (ΔV) over 48 months. Using microCT, Stok et al. [36] presented two whole bone QMA parameters linked to changes in bone shape observed in samples with OA; an angle to indicate the relative difference in erosion between the lateral and medial femoral condyles (ρ) and an angle to quantitatively measure the presence and severity of osteophytes at bone margins (σ).

Alternatively, others have focused on performing statistical modelling of the bone shape. Studies such as those by Bowes et al. [68] (MRI) have used SSM to analyse changes to the local surface area of the bone, while Pedoia et al. [69] (MRI) and Lynch et al. [70] (CT) have applied SSM to clinical knee OA datasets. By observing changes to the gross morphology of the subchondral bone, an SSM study suggested that variations to surface geometry could lead to changes in joint mechanical loading and subsequent changes to the gross morphology of the whole joint and, potentially, lead to OA [71].

Table 3-2: QMA parameters of subchondral bone

Imaging Mode Trabecular bone	Parameter	Abbrev.	Unit	Method detailed in
MRI	Volume fraction	BV/TV	%	Saha et al. (2000) [54]
	Surface-to-curve ratio	SCR	-	Saha et al. (2000) [54]
	Erosion index	EI	-	Saha et al. (2000) [54]
	Skeleton density	Sk.D	-	Chang et al. (2015) [49]
	Thickness	Tb.Th	mm	Chang et al. (2018) [50]
	Trabecular spacing	Tb.Sp	mm	Chang et al. (2018) [50]
	Plate width	PW, Tb.PW	µm	Saha et al. (2000) [58], Chen et al. (2016) [57], and Saha et al. (2015) [59]
	Plate-to-rod ratio	PRR, Tb.PR	-	Chen et al. (2016) [57] and Saha et al. (2015) [59]
	Apparent volume fraction	app.BV/TV	%	Majumdar et al. (1995) [44]
	Apparent thickness	app.Tb.Th	µm	Majumdar et al. (1997) [45] and Laib et al. (2001) [48]
	Apparent separation	app.Tb.Sp	µm	Majumdar et al. (1997) [45] and Laib et al. (2001) [48]
	Apparent number	app.Tb.N	$m\ m^{-1}$	Majumdar et al. (1997) [45] and Laib et al. (2001) [48]
	Pattern factor	TBPf	-	Hahn et al. (1992) [62]
	Degree of anisotropy	DA	-	Harrigan and Mann (1984) [63]
CT	Volume	BV	mm^3	Hildebrand et al. (1999) [52]
	Surface area	BS	mm^2	Hildebrand et al. (1999) [52]
	Surface to volume ratio	BS/BV	mm^{-1}	Hildebrand et al. (1999) [52]
	Volume fraction	BV/TV	%	Hildebrand et al. (1999) [52]
	Thickness	Tb.Th	mm	Hildebrand and Rüegsegger (1997) [31]
	Trabecular separation	Tb.Sp	mm	Hildebrand et al. (1999) [52]
	Trabecular number	Tb.N	mm^{-1}	Hildebrand et al. (1999) [52]
	Connectivity density	Conn.D	mm^{-3}	Odgaard and Gundersen (1993) [61]
	Degree of anisotropy	DA	-	Harrigan and Mann (1984) [63]
	Structural anisotropy: mean intercept length	MIL	-	Whitehouse (1974) [72]
	Structural anisotropy: volume orientation	VO	-	Kohler et al. (2005) [65]
	Structure model index	SMI	-	Hildebrand and Rüegsegger (1997) [53]

Cortical bone

CT	Total cortical volume	Ct.TV	mm^3	Burghardt et al. (2010) [65]
	Cortical bone volume	Ct.BV	mm^3	Burghardt et al. (2010) [65]
	Total cross-sectional area inside the periosteal envelope	Tt.Ar	mm^2	Burghardt et al. (2010) [65]
	Cortical Area	Ct.Ar	mm^2	Burghardt et al. (2010) [65]
	Cortical area fraction	Ct.Ar/Tt.Ar	%	Bouxsein et al. (2010) [10]
	Thickness	Ct.Th	mm	Kohler et al. (2005) [65]
	Porosity	Ct.Po	%	Burghardt et al. (2010) [65]
	Total pore volume	Ct.Po.V	mm^3	Burghardt et al. (2010) [65]
	Pore number	Po.N	n	Bouxsein et al. (2010) [10]
	Mean cortical pore diameter	Ct.Po.Dm	µm	Burghardt et al. (2010) [65]

Whole bone

MRI	Change in osteophyte volume	ΔV	mm^3	Hakky et al. (2015) [67]
CT	Inclination angle of the femoral condyles	ρ	°	Stok et al. (2016) [36]
	Osteophyte angle	σ	°	Stok et al. (2016) [36]
	Surface area of the subchondral bone	tAB	cm^2	Bowes et al. (2015) [68]

3.7 QMA of the whole joint

As a multifactorial disease affecting various structures, OA causes macroscopic changes to the overall morphometry of the joint [4]. Disruptions to normal mechanical interaction of joint tissues are essential to the study of OA pathogenesis. Interactions between joint biomechanics and joint morphology in the context of OA have been widely studied. However, not much is understood about which specific whole joint morphological changes are relevant and what their impacts on joint biomechanics are [73]. Joint space narrowing, malalignment, and joint instability all seem to be strongly correlated to OA in one way or the other [74], [75]. Quantitative imaging allows the observation of whole joint features and could help uncover its role in OA.

Studies using 3D imaging of the whole joint are usually distinguished from one another by their image acquisition protocols with considerations including joint pose and loading conditions [73]. Weight-bearing CT and MRI allow for the assessment of actual relative position and interaction between each joint component under loading stress and could be helpful in identifying conditions or deformities which may manifest only under weight-bearing conditions [76]. This section will detail three whole joint morphological parameters that are frequently reported in quantitative studies: joint contact area, joint space width, and joint alignment. Whole joint QMA parameters described in this section are listed in Table 3-3.

3.7.1 Joint contact area

Joint contact area is usually defined as the contact surface between the femoral and tibial cartilage during loading. It is often used to evaluate mechanical stress at articulating surfaces and was shown to be a strong predictor of OA [77], [78]. As the modality commonly used to visualise cartilage, most works on joint contact area are reported using MRI [79]–[82]. The scans are assessed at sequential, static, and loaded angles of knee flexion, and can be used to evaluate average contact stress, as well as cartilage deformation and contact area during loading. Joint contact surface is commonly assessed in terms of cartilage contact area and contact point which provide information on load transfer and articular contact stress.

The contact area of each cartilage plate can be determined by multiplying each manually drawn contact line by slice thickness [83], or by fitting surfaces to the segmented cartilage

and summing up the contact surface area [84]–[86] (Figure 3-4a). Another approach is to segment each cartilage plate separately and, using the same coordinate system, expand each adjacent cartilage plate by a voxel and define the overlapping voxels as the contact surface [81], [82], [87]. While not all studies report contact points, those that do typically evaluate it as the centroid of the contact area [86]–[88] or the shortest perpendicular distance from the tibial plateau to the femur [88].

No equivalent work is reported using CT due to difficulty in visualising cartilage. However, Stok et al. [36] proposed parameters to quantify contact area changes under virtual loading in contrast-enhanced microCT images for a rabbit OA model (Figure 3-4b). It is measured by shifting each segmented cartilage plate of the femur towards the tibia in a stepwise (voxel) manner and plotting the overlapping cartilage regions for each step. The shifting distance performed until the first incidence of overlap for the lateral and medial sides $(\chi_{\mathrm{L}}, \chi_{\mathrm{M}})$ and the rate at which the contact area increases (*m*) are reported. With cartilage visualisation in CT an ongoing research topic, many studies have instead focused on evaluating the joint space width as a method to observe whole joint morphometry.

3.7.2 Joint space width

Joint space width (JSW) is traditionally measured from 2D radiographs as a surrogate assessment of cartilage loss in OA patients and provides a responsive measure of OA progression in clinical settings [89], [90]. However, Marsh et al. [91] (using weight-bearing MRI) and Fritz et al. [92] (using weight-bearing CT), by applying 3D Euclidean distance to measure JSW, have indicated that JSW from 3D images could be more useful, showing more apposition of the cartilage and bone while functionally loaded, than JSW from weight-bearing radiographs. Alternatively, a recent work by Makki et al. [93] measured manually segmented 3D JSW (Figure 3-4c) using a partial differential equation approach for measuring thickness [94]. In their work, thickness is defined as the length of trajectories which run from one boundary to the other, and which follow a smooth vector field constructed in the region between those boundaries. Solving and summing the solutions of these partial differential equations yield the thickness of the region.

On the other hand, there has been a number of recent works quantifying JSW and joint space volume (JSV) in CT [95]–[97] (Figure 3-4d). There are minor differences between each

approach, though all are based on dilating the bone masks until the combined mask fills the joint space. The original bone masks are, then, subtracted from the combined mask to obtain the joint space mask, whose thickness is measured based on the 3D sphere fitting distance transform [31], and whose JSV is quantified in the same way as other volumetric QMA parameters. Through algorithm sharing among authors, these JSW methods were benchmarked, compiled, and published into a consensus approach for measuring JSW in metacarpophalangeal joints [98] with good scan-rescan reliability and a strong agreement between results from first- and second-generation HR-pQCT. The consensus method has been recently translated and applied for the assessment of JSW in microCT scans of rabbit [99], rat [51], and mouse [100] TFJ.

An alternative JSW measurement method has been performed in weight-bearing CT in a recent study by Turmezei et al. [101] by means of joint space mapping. Here, instead of applying morphological operations, each bone (femur/tibia) is projected onto the other to locate articulating areas, which would be used to define the joint space between them. These areas on both bones are matched, and JSW is defined as the distance between each mapped vertex. Similarly, Charon et al. [102] have also demonstrated that SSM can be used to create joint space maps to analyse the articulating surface and JSW using cone beam CT.

3.7.3 Joint alignment

In addition to JSW measurements, joint alignment is a measure based on traditional clinical assessments of knee radiography. Axial malalignment is associated with faster progression of radiographic OA changes [74]. Varus malalignment, in particular, was shown to increase the incidence risk of OA [103]. Measuring joint alignment in 3D using MRI and CT has potential to uncover information not available in 2D radiography, such as twist and tilt angles of the joint.

There are many studies that point towards a correlation between varus/valgus malalignment using radiographs and cartilage assessment using MRI [104]–[106]. However, there has been no MRI-based assessment of joint alignment so far. There has been a study that observed joint alignment in CT [107], but the evaluation was performed in 2D by measuring angles within specific slices. The lack of 3D imaging work on joint alignment is possibly due to the challenges of maintaining a consistent VOI and joint pose in 3D during acquisition and subsequent processing.

Maintaining consistent pose using foam wedges, Stok et al. [36] proposed two measures of joint alignment in 3D from microCT images of OA rabbit knees; namely, a joint centre of mass (Figure 3-4e) and an angle of twist. Joint centre of mass is defined as the vector connecting the centre of mass of the femur to the centre of mass of the tibia with length, λ and orientation in the form of angles with regard to the x-axis (α), y-axis (β), and z-axis (γ), respectively; while the angle of twist (τ) is defined as the difference in the yaw angle needed to align the femur and tibia to their common orientations. These metrics were demonstrated to be sensitive to OA.

More work remains to be done in the QMA of joint alignment for the results to match the reproducibility and robustness found in clinical radiographic assessments. Other radiographic techniques for quantifying joint malalignment could also be adjusted and applied to MRI and CT to assist with alignment and positioning issues. Work by Iranpour-Boroujeni et al. [108] could potentially be translated to handle 3D images by automating the landmark placement process.

Table 3-3: QMA parameters of whole joint

Imaging Mode	Parameter	Abbrev.	Unit	Method detailed in
MRI	Joint space width	JSW	mm	Makki et al. (2019) [93]
	Contact area under loading	-	mm^2	DeFrate et al. (2004) [88]
	Contact point under loading	-	mm	DeFrate et al. (2004) [88]
CT	Joint space width	JSW	mm	Stok et al. (2020) [98], Turmezei et al. (2021) [109], and Fritz et al. (2022) [92]
	Joint space volume	JSV	μm^3	Stok et al. (2020) [98]
	Cartilage contact area under virtual loading: rate of increase	m	mm^2/mm	Stok et al. (2016) [36]
	Cartilage contact area under virtual loading: distance loaded until first contact	χ	mm	Stok et al. (2016) [36]
	Centre of mass	λ	mm	Stok et al. (2016) [36]
	Centre of mass	α	°	Stok et al. (2016) [36]
	Centre of mass	β	°	Stok et al. (2016) [36]
	Centre of mass	γ	°	Stok et al. (2016) [36]
	Twist angle	τ	°	Stok et al. (2016) [36]

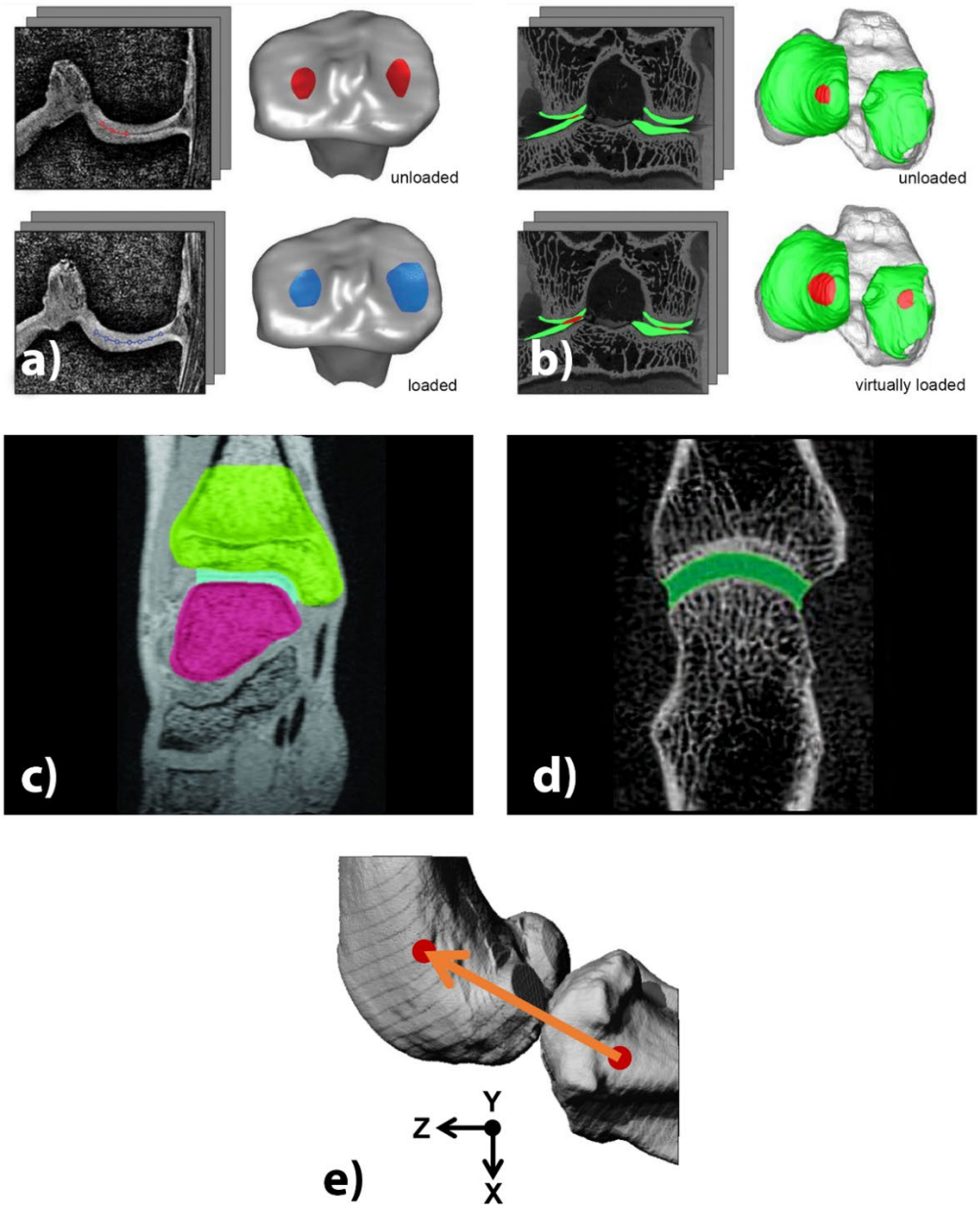

Figure 3-4: (a)[9] Measurement of joint contact area under loading in 3 T MRI scan of human TFJ joint as described by Shin et al. [85] *with contact area in unloaded (red) and loaded (blue) conditions shown. (b)[10] Measurement of joint contact area under virtual loading from microCT scan of rabbit TFJ joint as described by Stok et al.* [36]*, where segmented cartilage plates (green) were virtually shifted, and their contact area tracked (red). (c)[11] Measurement of joint space width (cyan) between tibia (green) and talus (pink) using manual segmentation of 3 T MRI scan of human tibiotalar joint as described by Makki et al.* [93]*. (d)[12] Measurement of joint space width (green)* [97] *from high-resolution peripheral quantitative computed tomography scan of the human metacarpophalangeal joint. (e) Measurement of joint alignment in segmented microCT scan of mouse TFJ joint using joint centre of mass, defined as the vector (orange) connecting the centres of mass (red) of the tibia and the femur with magnitude (λ) and angles (α, β, γ) measured against the x, y, and z axes of the Cartesian coordinate system, respectively.*

[9] Reprinted from Journal of Magnetic Resonance Imaging, 34, C. S. Shin et al., In vivo tibiofemoral cartilage-to-cartilage contact area of females with medial osteoarthritis under acute loading using MRI, 1405 – 1413, 2011, with permission from John Wiley and Sons. https://doi.org/10.1002/jmri.22796 [85].
[10] Adapted from K. S. Stok et al. (2016) Three-Dimensional Quantitative Morphometric Analysis (QMA) for In Situ Joint and Tissue Assessment of Osteoarthritis in a Preclinical Rabbit Disease Model. PLOS ONE, 11: e0147564. https://doi.org/10.1371/journal.pone.0147564 [36] with permission.
[11] Copyright 2019 IEEE. Reprinted, with permission, from K. Makki et al. (2019) 4D in vivo quantification of ankle joint space width using dynamic MRI. 2019 41st Annual International Conference of the IEEE Engineering in Medicine and Biology Society (EMBC), 2115-2118. https://doi.org/10.1109/EMBC.2019.8856687 [93].
[12] Reprinted by permission from Springer Nature Customer Service Centre GmbH: Springer Annals of Biomedical Engineering, Quantitative In Vivo HR-pQCT Imaging of 3D Wrist and Metacarpophalangeal Joint Space Width in Rheumatoid Arthritis, A. J. Burghardt et al., 2013. https://doi.org/10.1007/s10439-013-0871-x [97].

3.8 Perspective on QMA development

Advances in 3D image acquisition and processing techniques have facilitated the non-invasive assessment of various joint structures using MRI and CT for OA research. This has enabled more precise extraction of quantitative morphometric information for different joint tissues that allows researchers to understand and identify structural changes due to OA with higher sensitivity and specificity. Techniques such as SSM, beyond its use for analysing shape variations, can also assist in batch processing by taking advantage of correspondence maps between samples [24], [99]. These methods, combined with applications of deep learning for segmentation [38], [110] and processing [111], can improve the efficiency and accuracy of QMA measurements and lay a solid foundation of features and indices for future clinical and research applications.

This review has highlighted that QMA is an active research area, and many QMA techniques from one modality can be translated to another, as shown by Laib et al. [48] in their application of CT trabecular analysis methods to MRI and Chen et al. [60] in their application of MRI trabecular analysis methods to CT. New, unexplored quantification of structural features in one modality can also benefit from existing algorithms in the other. Given appropriate visualisation, there is potential for MRI studies to perform direct quantifications of subchondral bone structures using algorithms developed for CT; while contrast-enhanced CT studies can analyse denuded cartilage area and volume, as well as define regional subdivisions of the cartilage to precisely track local changes due to OA.

However, it was noted during the literature search that many of the described methods are not easily accessible. Analysis methods are often implemented as a combination of routines using proprietary software and in-house scripts, with some SSM routines patented. This could lead to difficulty in comparing algorithm output, redundant implementations of the same QMA metrics, and fragmentation of computational tools in the research field. By making scripts open-source and readily accessible, standardised and consensus methods can be developed and improved by the community, such as the consensus JSW analysis approach in high-resolution peripheral quantitative CT studies [98], the spherical harmonics SSM framework [112], and many open-sourced deep learning segmentation methods [113].

Other coordinated efforts to develop publicly available research datasets, such as the Osteoarthritis Initiative (OAI), have seen success in progressing OA research over the past decade [114]. Similar advances could also be achieved with the formalisation and adoption of open-source software development practices within the field. Organisations such as the International Society of Osteoarthritis Imaging (ISOAI) and the Open and Reproducible Musculoskeletal Imaging Research (ORMIR) community could play a key role in providing a platform for discussion and coordination towards a more efficient research field overall.

3.9 Conclusion

Due to the different advantages and disadvantages associated with each imaging method, traditionally, no single imaging method can capture all joint structures with sufficient detail. MRI is generally used for QMA of articular cartilage, while CT is generally used for QMA of subchondral bone structures. However, recent developments point towards a full suite of quantitative measurements of all joint structures using a single imaging modality. Higher-resolution MRI technology and accompanying image processing techniques have allowed higher-resolution visualisation of subchondral bone structures. Similarly, CT-based contrast agents have enabled the visualisation of cartilage and soft tissues. Such advances have led to the emergence of various QMA propositions and applications. However, there is still redundancy and inefficiency in developing new QMA approaches due to the use of in-house scripts and proprietary software.

Adoption of open-source practices can allow algorithms developed for either imaging modality to be shared. This makes it possible to close the knowledge gap where QMA for certain structures and pathological features has not been explored. Further community coordination on workflow interfacing and coding practices can facilitate the development of new workflow and increase research output overall.

3.10 Acknowledgement

This work was supported by the Discovery Projects scheme of the Australian Research Council (DP180101838). The authors would like to thank T. Lerspiphopporn for producing the schematics in this work.

References

[1] A. Guermazi *et al.*, “Imaging in Osteoarthritis,” *Rheum. Dis. Clin. North Am.*, vol. 34, no. 3, pp. 645–687, Aug. 2008, doi: 10.1016/J.RDC.2008.04.006.

[2] J. E. Costello, N. D. Cecava, J. E. Tucker, and J. L. Bau, “CT Radiation Dose: Current Controversies and Dose Reduction Strategies,” *Am. J. Roentgenol.*, vol. 201, no. 6, pp. 1283–1290, Dec. 2013, doi: 10.2214/AJR.12.9720.

[3] F. W. Roemer *et al.*, “State of the Art: Imaging of osteoarthritis—revisited 2020,” *Radiology*, vol. 296, no. 1, pp. 5–21, Jul. 2020, doi: 10.1148/RADIOL.2020192498.

[4] R. W. Moskowitz, R. D. Altman, M. C. Hochberg, J. A. Buckwalter, and V. M. Goldberg, *Osteoarthritis, Diagnosis and Medical/surgical Management*, 4th ed. Philadelphia, PA: Williams & Wilkins, 2004.

[5] M. P. Wattjes and F. Barkhof, “High field MRI in the diagnosis of multiple sclerosis: High field-high yield?,” *Neuroradiology*, vol. 51, no. 5, pp. 279–292, May 2009, doi: 10.1007/S00234-009-0512-0.

[6] E. Donnelly, “Methods for assessing bone quality: A review,” in *Clinical Orthopaedics and Related Research*, Nov. 2011, vol. 469, no. 8, pp. 2128–2138, doi: 10.1007/s11999-010-1702-0.

[7] E. Lin and A. Alessio, “What are the basic concepts of temporal, contrast, and spatial resolution in cardiac CT?,” *J. Cardiovasc. Comput. Tomogr.*, vol. 3, no. 6, pp. 403–8, 2009, doi: 10.1016/j.jcct.2009.07.003.

[8] F. Eckstein, W. Wirth, and A. G. Culvenor, “Osteoarthritis year in review 2020: imaging,” *Osteoarthr. Cartil.*, vol. 29, no. 2, pp. 170–179, Feb. 2021, doi: 10.1016/J.JOCA.2020.12.019.

[9] F. W. Wehrli, H. K. Song, P. K. Saha, and A. C. Wright, “Quantitative MRI for the assessment of bone structure and function,” *NMR Biomed.*, vol. 19, no. 7, pp. 731–764, Nov. 2006, doi: 10.1002/nbm.1066.

[10] M. L. Bouxsein, S. K. Boyd, B. A. Christiansen, R. E. Guldberg, K. J. Jepsen, and R. Müller, “Guidelines for assessment of bone microstructure in rodents using micro-computed

tomography," *J. Bone Miner. Res.*, vol. 25, no. 7, pp. 1468–1486, Jun. 2010, doi: 10.1002/jbmr.141.

[11] F. Eckstein *et al.*, "Proposal for a nomenclature for Magnetic Resonance Imaging based measures of articular cartilage in osteoarthritis," *Osteoarthr. Cartil.*, vol. 14, no. 10, pp. 974–983, Oct. 2006, doi: 10.1016/j.joca.2006.03.005.

[12] W. Wirth, C. Ladel, · Susanne Maschek, A. Wisser, F. Eckstein, and · Frank Roemer, "Quantitative measurement of cartilage morphology in osteoarthritis: current knowledge and future directions," *Skelet. Radiol. 2022*, pp. 1–16, Nov. 2022, doi: 10.1007/S00256-022-04228-W.

[13] D. E. Whittier *et al.*, "Guidelines for the assessment of bone density and microarchitecture in vivo using high-resolution peripheral quantitative computed tomography," *Osteoporos. Int.*, vol. 31, no. 9, pp. 1607–1627, Sep. 2020, doi: 10.1007/S00198-020-05438-5.

[14] G. M. Campbell and A. Sophocleous, "Quantitative analysis of bone and soft tissue by micro-computed tomography: applications to ex vivo and in vivo studies," *Bonekey Rep.*, vol. 3, p. 564, Aug. 2014, doi: 10.1038/BONEKEY.2014.59.

[15] G. Musumeci, "Functional Anatomy in Knee Osteoarthritis: Patellofemoral Joint vs. Tibiofemoral Joint," *J. Funct. Morphol. Kinesiol.*, vol. 2, no. 1, p. 8, Feb. 2017, doi: 10.3390/jfmk2010008.

[16] D. W. Dempster *et al.*, "Standardized nomenclature, symbols, and units for bone histomorphometry: A 2012 update of the report of the ASBMR Histomorphometry Nomenclature Committee," *J. Bone Miner. Res.*, vol. 28, no. 1, pp. 2–17, Jan. 2013, doi: 10.1002/jbmr.1805.

[17] F. Eckstein, F. Cicuttini, J. P. Raynauld, J. C. Waterton, and C. Peterfy, "Magnetic resonance imaging (MRI) of articular cartilage in knee osteoarthritis (OA): morphological assessment," *Osteoarthr. Cartil.*, vol. 14, no. SUPPL. 1, pp. 46–75, Jan. 2006, doi: 10.1016/j.joca.2006.02.026.

[18] A. W. Palmer, R. E. Guldberg, and M. E. Levenston, "Analysis of cartilage matrix fixed charge density and three-dimensional morphology via contrast-enhanced

microcomputed tomography," *Proc. Natl. Acad. Sci. U. S. A.*, vol. 103, no. 51, pp. 19255–19260, Dec. 2006, doi: 10.1073/pnas.0606406103.

[19] N. S. Joshi, P. N. Bansal, R. C. Stewart, B. D. Snyder, and M. W. Grinstaff, "Effect of Contrast Agent Charge on Visualization of Articular Cartilage Using Computed Tomography: Exploiting Electrostatic Interactions for Improved Sensitivity," *J. Am. Chem. Soc.*, vol. 131, no. 37, pp. 13234–13235, Sep. 2009, doi: 10.1021/ja9053306.

[20] H. T. Kokkonen, J. S. Jurvelin, V. Tiitu, and J. Töyräs, "Detection of mechanical injury of articular cartilage using contrast enhanced computed tomography," *Osteoarthr. Cartil.*, vol. 19, no. 3, pp. 295–301, Mar. 2011, doi: 10.1016/j.joca.2010.12.012.

[21] T. H. Steiner *et al.*, "Preclinical investigation of the development of osteoarthritis-like degeneration in a rat trauma model using micro-computed tomography," *Osteoarthr. Cartil.*, vol. 20, pp. S50–S51, Apr. 2012, doi: 10.1016/j.joca.2012.02.599.

[22] W. Wirth and F. Eckstein, "A technique for regional analysis of femorotibial cartilage thickness based on quantitative magnetic resonance imaging," *IEEE Trans. Med. Imaging*, vol. 27, no. 6, pp. 737–744, Jun. 2008, doi: 10.1109/TMI.2007.907323.

[23] R. B. Frobell *et al.*, "The acutely ACL injured knee assessed by MRI: changes in joint fluid, bone marrow lesions, and cartilage during the first year," *Osteoarthr. Cartil.*, vol. 17, no. 2, pp. 161–167, Feb. 2009, doi: 10.1016/J.JOCA.2008.06.020.

[24] T. G. Williams *et al.*, "Anatomically corresponded regional analysis of cartilage in asymptomatic and osteoarthritic knees by statistical shape modelling of the bone," *IEEE Trans. Med. Imaging*, vol. 29, no. 8, pp. 1541–1559, Aug. 2010, doi: 10.1109/TMI.2010.2047653.

[25] T. G. Williams *et al.*, "Measurement and visualisation of focal cartilage thickness change by MRI in a study of knee osteoarthritis using a novel image analysis tool," *Br. J. Radiol.*, vol. 83, no. 995, pp. 940–948, Feb. 2010, doi: 10.1259/bjr/68875123.

[26] T. J. Mosher *et al.*, "Knee articular cartilage damage in osteoarthritis: Analysis of MR image biomarker reproducibility in ACRIN-PA 4001 multicenter trial," *Radiology*, vol. 258, no. 3, pp. 832–842, Mar. 2011, doi: 10.1148/RADIOL.10101174/ASSET/IMAGES/LARGE/101174T06.JPEG.

[27] C. G. Peterfy *et al.*, “Quantification of articular cartilage in the knee with pulsed saturation transfer subtraction and fat-suppressed MR imaging: Optimization and validation,” *Radiology*, vol. 192, no. 2, pp. 485–491, Aug. 1994, doi: 10.1148/radiology.192.2.8029420.

[28] L. Xie, A. S. P. Lin, M. E. Levenston, and R. E. Guldberg, “Quantitative assessment of articular cartilage morphology via EPIC-µCT,” *Osteoarthr. Cartil.*, vol. 17, no. 3, pp. 313–320, Mar. 2009, doi: 10.1016/j.joca.2008.07.015.

[29] W. E. Lorensen and H. E. Cline, “Marching cubes: A high resolution 3D surface construction algorithm,” *ACM SIGGRAPH Comput. Graph.*, vol. 21, no. 4, pp. 163–169, Aug. 1987, doi: 10.1145/37402.37422.

[30] J. Hohe, G. Ateshian, M. Reiser, K.-H. Englmeier, and F. Eckstein, “Surface size, curvature analysis, and assessment of knee joint incongruity with MRI in vivo,” *Magn. Reson. Med.*, vol. 47, no. 3, pp. 554–561, Mar. 2002, doi: 10.1002/mrm.10097.

[31] T. Hildebrand and P. Rüegsegger, “A new method for the model-independent assessment of thickness in three-dimensional images,” *J. Microsc.*, vol. 185, no. 1, pp. 67–75, Jan. 1997, doi: 10.1046/j.1365-2818.1997.1340694.x.

[32] T. Stammberger, F. Eckstein, K. Englmeier, and M. Reiser, “Determination of 3D cartilage thickness data from MR imaging: Computational method and reproducibility in the living,” *Magn. Reson. Med.*, vol. 41, no. 3, pp. 529–536, Mar. 1999, doi: 10.1002/(SICI)1522-2594(199903)41:3<529::AID-MRM15>3.0.CO;2-Z.

[33] H. Graichen *et al.*, “Validation of high-resolution water-excitation magnetic resonance imaging for quantitative assessment of thin cartilage layers,” *Osteoarthr. Cartil.*, vol. 8, no. 2, pp. 106–114, Mar. 2000, doi: 10.1053/JOCA.1999.0278.

[34] G. J. Michalak, R. Walker, and S. K. Boyd, “Concurrent Assessment of Cartilage Morphology and Bone Microarchitecture in the Human Knee Using Contrast-Enhanced HR-pQCT Imaging,” *J. Clin. Densitom.*, vol. 22, no. 1, pp. 74–85, Jan. 2019, doi: 10.1016/J.JOCD.2018.07.002.

[35] A. A. Qazi, J. Folkesson, P. C. Pettersen, M. A. Karsdal, C. Christiansen, and E. B. Dam, “Separation of healthy and early osteoarthritis by automatic quantification of cartilage

homogeneity," *Osteoarthr. Cartil.*, vol. 15, no. 10, pp. 1199–1206, Oct. 2007, doi: 10.1016/j.joca.2007.03.016.

[36] K. S. Stok *et al.*, "Three-Dimensional Quantitative Morphometric Analysis (QMA) for In Situ Joint and Tissue Assessment of Osteoarthritis in a Preclinical Rabbit Disease Model," *PLoS One*, vol. 11, no. 1, p. e0147564, Jan. 2016, doi: 10.1371/journal.pone.0147564.

[37] S. Kauppinen *et al.*, "3D morphometric analysis of calcified cartilage properties using micro-computed tomography," *Osteoarthr. Cartil.*, vol. 27, no. 1, pp. 172–180, Jan. 2019, doi: 10.1016/j.joca.2018.09.009.

[38] S. J. O. Rytky *et al.*, "Automated analysis of rabbit knee calcified cartilage morphology using micro-computed tomography and deep learning," *J. Anat.*, vol. 239, no. 2, pp. 251–263, Aug. 2021, doi: 10.1111/JOA.13435.

[39] M. Mahjoub, F. Berenbaum, and X. Houard, "Why subchondral bone in osteoarthritis? the importance of the cartilage bone interface in osteoarthritis," *Osteoporos. Int.*, vol. 23, no. 8 SUPPL, pp. 841–846, Dec. 2012, doi: 10.1007/S00198-012-2161-0.

[40] S. I. M. Lepage *et al.*, "Beyond Cartilage Repair: The Role of the Osteochondral Unit in Joint Health and Disease," *Tissue Eng. - Part B Rev.*, vol. 25, no. 2, pp. 114–125, Apr. 2019, doi: 10.1089/TEN.TEB.2018.0122.

[41] M. B. Goldring and S. R. Goldring, "Articular cartilage and subchondral bone in the pathogenesis of osteoarthritis," *Ann. N. Y. Acad. Sci.*, vol. 1192, no. 1, pp. 230–237, Apr. 2010, doi: 10.1111/j.1749-6632.2009.05240.x.

[42] G. Li *et al.*, "Subchondral bone in osteoarthritis: Insight into risk factors and microstructural changes," *Arthritis Res. Ther.*, vol. 15, no. 6, pp. 1–12, Dec. 2013, doi: 10.1186/ar4405.

[43] R. Dalvi, R. Abugharbieh, D. C. Wilson, and D. R. Wilson, "Multi-contrast MR for enhanced bone imaging and segmentation," in *Annual International Conference of the IEEE Engineering in Medicine and Biology - Proceedings*, 2007, pp. 5620–5623, doi: 10.1109/IEMBS.2007.4353621.

[44] S. Majumdar *et al.*, “Evaluation of technical factors affecting the quantification of trabecular bone structure using magnetic resonance imaging,” *Bone*, vol. 17, no. 4, pp. 417–430, Oct. 1995, doi: 10.1016/S8756-3282(95)00263-4.

[45] S. Majumdar *et al.*, “Correlation of Trabecular Bone Structure with Age, Bone Mineral Density, and Osteoporotic Status: In Vivo Studies in the Distal Radius Using High Resolution Magnetic Resonance Imaging,” *J. Bone Miner. Res.*, vol. 12, no. 1, pp. 111–118, Jan. 1997, doi: 10.1359/jbmr.1997.12.1.111.

[46] A. Aprovitola and L. Gallo, “Knee bone segmentation from MRI: A classification and literature review,” *Biocybern. Biomed. Eng.*, vol. 36, no. 2, pp. 437–449, Jan. 2016, doi: 10.1016/j.bbe.2015.12.007.

[47] C. A. Sell, J. N. Masi, A. Burghardt, D. Newitt, T. M. Link, and S. Majumdar, “Quantification of Trabecular Bone Structure Using Magnetic Resonance Imaging at 3 Tesla—Calibration Studies Using Microcomputed Tomography as a Standard of Reference,” *Calcif. Tissue Int.*, vol. 76, no. 5, p. 355, May 2005, doi: 10.1007/S00223-004-0111-3.

[48] A. Laib, O. Beuf, A. Issever, D. C. Newitt, and S. Majumdar, “Direct measures of trabecular bone architecture from MR images,” *Adv. Exp. Med. Biol.*, vol. 496, pp. 37–46, 2001, doi: 10.1007/978-1-4615-0651-5_5.

[49] G. Chang *et al.*, “7T MRI detects deterioration in subchondral bone microarchitecture in subjects with mild knee osteoarthritis as compared with healthy controls,” *J. Magn. Reson. Imaging*, vol. 41, no. 5, pp. 1311–1317, May 2015, doi: 10.1002/JMRI.24683.

[50] G. Chang *et al.*, “3-T MR Imaging of Proximal Femur Microarchitecture in Subjects with and without Fragility Fracture and Nonosteoporotic Proximal Femur Bone Mineral Density,” *https://doi.org/10.1148/radiol.2017170138*, vol. 287, no. 2, pp. 608–619, Feb. 2018, doi: 10.1148/RADIOL.2017170138.

[51] B. A. Besler *et al.*, “Quantitative measures of bone shape, cartilage morphometry and joint alignment are associated with disease in an ACLT and MMx rat model of osteoarthritis,” *Bone*, vol. 146, p. 115903, Feb. 2021, doi: 10.1016/j.bone.2021.115903.

[52] T. Hildebrand, A. Laib, R. Müller, J. Dequeker, and P. Rüegsegger, “Direct Three-

Dimensional Morphometric Analysis of Human Cancellous Bone: Microstructural Data from Spine, Femur, Iliac Crest, and Calcaneus," *J. Bone Miner. Res.*, vol. 14, no. 7, pp. 1167–1174, Jul. 1999, doi: 10.1359/jbmr.1999.14.7.1167.

[53] T. Hildebrand and P. Rüegsegger, "Quantification of Bone Microarchitecture with the Structure Model Index," *Comput. Methods Biomech. Biomed. Engin.*, vol. 1, no. 1, pp. 15–23, 1997, doi: 10.1080/01495739708936692.

[54] P. K. Saha, B. R. Gomberg, and F. W. Wehrli, "Three-Dimensional Digital Topological Characterization of Cancellous Bone Architecture," 2000. doi: 10.1002/(SICI)1098-1098(2000)11:1.

[55] P. K. Saha and B. B. Chaudhuri, "3D Digital Topology under Binary Transformation with Applications," *Comput. Vis. Image Underst.*, vol. 63, no. 3, pp. 418–429, May 1996, doi: 10.1006/CVIU.1996.0032.

[56] M. Prince, R. Bryce, E. Albanese, A. Wimo, W. Ribeiro, and C. P. Ferri, "The global prevalence of dementia: a systematic review and metaanalysis," *Alzheimers Dement*, vol. 9, no. 1, pp. 63-75.e2, 2013, doi: 10.1016/j.jalz.2012.11.007.

[57] C. Chen *et al.*, "Trabecular bone characterization on the continuum of plates and rods using in vivo MR imaging and volumetric topological analysis," *Phys. Med. Biol.*, vol. 61, no. 18, p. N478, Aug. 2016, doi: 10.1088/0031-9155/61/18/N478.

[58] P. K. Saha, Y. Xu, H. Duan, A. Heiner, and G. Liang, "Volumetric topological analysis: A novel approach for trabecular bone classification on the continuum between plates and rods," *IEEE Trans. Med. Imaging*, vol. 29, no. 11, pp. 1821–1838, Nov. 2010, doi: 10.1109/TMI.2010.2050779.

[59] P. K. Saha *et al.*, "Characterization of trabecular bone plate-rod microarchitecture using multirow detector CT and the tensor scale: Algorithms, validation, and applications to pilot human studies," *Med. Phys.*, vol. 42, no. 9, pp. 5410–5425, Sep. 2015, doi: 10.1118/1.4928481.

[60] C. Chen *et al.*, "Quantitative imaging of peripheral trabecular bone microarchitecture using MDCT," *Med. Phys.*, vol. 45, no. 1, pp. 236–249, Jan. 2018, doi: 10.1002/MP.12632.

[61] A. Odgaard and H. J. G. Gundersen, “Quantification of connectivity in cancellous bone, with special emphasis on 3-D reconstructions,” *Bone*, vol. 14, no. 2, pp. 173–182, Mar. 1993, doi: 10.1016/8756-3282(93)90245-6.

[62] M. Hahn, M. Vogel, M. Pompesius-Kempa, and G. Delling, “Trabecular bone pattern factor-a new parameter for simple quantification of bone microarchitecture,” *Bone*, vol. 13, no. 4, pp. 327–330, Jul. 1992, doi: 10.1016/8756-3282(92)90078-B.

[63] T. P. Harrigan and R. W. Mann, “Characterization of microstructural anisotropy in orthotropic materials using a second rank tensor,” *J. Mater. Sci.*, vol. 19, no. 3, pp. 761–767, Mar. 1984, doi: 10.1007/BF00540446.

[64] O. O. Adebayo *et al.*, “Role of subchondral bone properties and changes in development of load-induced osteoarthritis in mice,” *Osteoarthr. Cartil.*, vol. 25, no. 12, pp. 2108–2118, Dec. 2017, doi: 10.1016/J.JOCA.2017.08.016.

[65] A. J. Burghardt, H. R. Buie, A. Laib, S. Majumdar, and S. K. Boyd, “Reproducibility of direct quantitative measures of cortical bone microarchitecture of the distal radius and tibia by HR-pQCT,” *Bone*, vol. 47, no. 3, pp. 519–528, Sep. 2010, doi: 10.1016/j.bone.2010.05.034.

[66] M. Oliveira Silva, J. L. Gregory, N. Ansari, and K. S. Stok, “Molecular Signaling Interactions and Transport at the Osteochondral Interface: A Review,” *Front. Cell Dev. Biol.*, vol. 8, p. 750, Aug. 2020, doi: 10.3389/FCELL.2020.00750.

[67] M. Hakky, M. Jarraya, C. Ratzlaff, A. Guermazi, and J. Duryea, “Validity and responsiveness of a new measure of knee osteophytes for osteoarthritis studies: data from the osteoarthritis initiative,” *Osteoarthr. Cartil.*, vol. 23, no. 12, pp. 2199–2205, Dec. 2015, doi: 10.1016/J.JOCA.2015.07.003.

[68] M. A. Bowes, G. R. Vincent, C. B. Wolstenholme, and P. G. Conaghan, “A novel method for bone area measurement provides new insights into osteoarthritis and its progression,” *Ann. Rheum. Dis.*, vol. 74, no. 3, pp. 519–525, Mar. 2015, doi: 10.1136/ANNRHEUMDIS-2013-204052.

[69] V. Pedoia *et al.*, “Three-dimensional MRI-based statistical shape model and application to a cohort of knees with acute ACL injury,” *Osteoarthr. Cartil.*, vol. 23, no. 10, pp.

1695–1703, Oct. 2015, doi: 10.1016/J.JOCA.2015.05.027.

[70] J. T. Lynch *et al.*, "Statistical shape modelling reveals large and distinct subchondral bony differences in osteoarthritic knees," *J. Biomech.*, vol. 93, pp. 177–184, Aug. 2019, doi: 10.1016/J.JBIOMECH.2019.07.003.

[71] T. L. Bredbenner, T. D. Eliason, R. S. Potter, R. L. Mason, L. M. Havill, and D. P. Nicolella, "Statistical shape modeling describes variation in tibia and femur surface geometry between Control and Incidence groups from the Osteoarthritis Initiative database," *J. Biomech.*, vol. 43, no. 9, pp. 1780–1786, Jun. 2010, doi: 10.1016/J.JBIOMECH.2010.02.015.

[72] W. J. Whitehouse, "The quantitative morphology of anisotropic trabecular bone," *J. Microsc.*, vol. 101, no. 2, pp. 153–168, Jul. 1974, doi: 10.1111/j.1365-2818.1974.tb03878.x.

[73] D. R. Wilson, E. J. McWalter, and J. D. Johnston, "The Measurement of Joint Mechanics and Their Role in Osteoarthritis Genesis and Progression," *Rheum. Dis. Clin. North Am.*, vol. 39, no. 1, pp. 21–44, Feb. 2013, doi: 10.1016/j.rdc.2012.11.002.

[74] A. Heijink *et al.*, "Biomechanical considerations in the pathogenesis of osteoarthritis of the knee," *Knee Surgery, Sports Traumatology, Arthroscopy*, vol. 20, no. 3. pp. 423–435, Mar. 2012, doi: 10.1007/s00167-011-1818-0.

[75] R. D. Altman *et al.*, "Radiographic assessment of progression in osteoarthritis," *Arthritis Rheum.*, vol. 30, no. 11, pp. 1214–1225, Nov. 1987, doi: 10.1002/art.1780301103.

[76] F. Bruno *et al.*, "Weight-bearing MRI of the knee: a review of advantages and limits," *Acta Biomed.*, vol. 89, no. Suppl 1, p. 88, Jan. 2018, doi: 10.23750/ABM.V89I1-S.7011.

[77] N. A. Segal *et al.*, "Baseline articular contact stress levels predict incident symptomatic knee osteoarthritis development in the MOST cohort," *J. Orthop. Res.*, vol. 27, no. 12, pp. 1562–1568, Dec. 2009, doi: 10.1002/JOR.20936.

[78] D. D. Anderson, C. Van Hofwegen, J. L. Marsh, and T. D. Brown, "Is elevated contact stress predictive of post-traumatic osteoarthritis for imprecisely reduced tibial plafond fractures?," *J. Orthop. Res.*, vol. 29, no. 1, pp. 33–39, Jan. 2011, doi:

10.1002/JOR.21202.

[79] R. Von Eisenhart-Rothe, M. Siebert, C. Bringmann, T. Vogl, K. H. Englmeier, and H. Graichen, “A new in vivo technique for determination of 3D kinematics and contact areas of the patello-femoral and tibio-femoral joint,” *J. Biomech.*, vol. 37, no. 6, pp. 927–934, Jun. 2004, doi: 10.1016/j.jbiomech.2003.09.034.

[80] G. E. Gold, T. F. Besier, C. E. Draper, D. S. Asakawa, S. L. Delp, and G. S. Beaupre, “Weight-bearing MRI of patellofemoral joint cartilage contact area,” *J. Magn. Reson. Imaging*, vol. 20, no. 3, pp. 526–530, Sep. 2004, doi: 10.1002/jmri.20146.

[81] S. Hinterwimmer, R. Von Eisenhart-Rothe, M. Siebert, F. Welsch, T. Vogl, and H. Graichen, “Patella kinematics and patello-femoral contact areas in patients with genu varum and mild osteoarthritis,” *Clin. Biomech.*, vol. 19, no. 7, pp. 704–710, Aug. 2004, doi: 10.1016/j.clinbiomech.2004.04.011.

[82] S. Hinterwimmer *et al.*, “In vivo contact areas of the knee in patients with patellar subluxation,” *J. Biomech.*, vol. 38, no. 10, pp. 2095–2101, Oct. 2005, doi: 10.1016/j.jbiomech.2004.09.008.

[83] A. Hosseini, S. Van de Velde, T. J. Gill, and G. Li, “Tibiofemoral cartilage contact biomechanics in patients after reconstruction of a ruptured anterior cruciate ligament,” *J. Orthop. Res.*, vol. 30, no. 11, pp. 1781–1788, Nov. 2012, doi: 10.1002/jor.22122.

[84] V. V. Patel *et al.*, “Magnetic Resonance Imaging of Patellofemoral Kinematics with Weight-Bearing,” *J. Bone Jt. Surg. - Ser. A*, vol. 85, no. 12, pp. 2419–2424, Dec. 2003, doi: 10.2106/00004623-200312000-00021.

[85] C. S. Shin, R. B. Souza, D. Kumar, T. M. Link, B. T. Wyman, and S. Majumdar, “In vivo tibiofemoral cartilage-to-cartilage contact area of females with medial osteoarthritis under acute loading using MRI,” *J. Magn. Reson. Imaging*, vol. 34, no. 6, pp. 1405–1413, Dec. 2011, doi: 10.1002/jmri.22796.

[86] B. S. Borotikar and F. T. Sheehan, “In vivo patellofemoral contact mechanics during active extension using a novel dynamic MRI-based methodology,” *Osteoarthr. Cartil.*, vol. 21, no. 12, pp. 1886–1894, Dec. 2013, doi: 10.1016/j.joca.2013.08.023.

[87] A. M. Schmidt, D. J. Stockton, M. A. Hunt, A. Yung, B. A. Masri, and D. R. Wilson, "Reliability of tibiofemoral contact area and centroid location in upright, open MRI," *BMC Musculoskelet. Disord.*, vol. 21, no. 1, pp. 1–9, Dec. 2020, doi: 10.1186/s12891-020-03786-1.

[88] L. E. Defrate, H. Sun, T. J. Gill, H. E. Rubash, and G. Li, "In vivo tibiofemoral contact analysis using 3D MRI-based knee models," *J. Biomech.*, vol. 37, no. 10, pp. 1499–1504, Oct. 2004, doi: 10.1016/j.jbiomech.2004.01.012.

[89] W. M. Reichmann, J. F. Maillefert, D. J. Hunter, J. N. Katz, P. G. Conaghan, and E. Losina, "Responsiveness to change and reliability of measurement of radiographic joint space width in osteoarthritis of the knee: a systematic review," *Osteoarthr. Cartil.*, vol. 19, no. 5, pp. 550–556, May 2011, doi: 10.1016/J.JOCA.2011.01.023.

[90] P. S. Emrani *et al.*, "Joint space narrowing and Kellgren–Lawrence progression in knee osteoarthritis: an analytic literature synthesis," *Osteoarthr. Cartil.*, vol. 16, no. 8, pp. 873–882, Aug. 2008, doi: 10.1016/J.JOCA.2007.12.004.

[91] M. Marsh *et al.*, "Differences between X-ray and MRI-determined knee cartilage thickness in weight-bearing and non-weight-bearing conditions," *Osteoarthr. Cartil.*, vol. 21, no. 12, pp. 1876–1885, Dec. 2013, doi: 10.1016/J.JOCA.2013.09.006.

[92] B. Fritz, J. Fritz, S. F. Fucentese, C. W. A. Pfirrmann, and R. Sutter, "Three-dimensional analysis for quantification of knee joint space width with weight-bearing CT: comparison with non-weight-bearing CT and weight-bearing radiography," *Osteoarthr. Cartil.*, vol. 30, no. 5, pp. 671–680, May 2022, doi: 10.1016/j.joca.2021.11.019.

[93] K. Makki *et al.*, "4D in vivo quantification of ankle joint space width using dynamic MRI," in *2019 41st Annual International Conference of the IEEE Engineering in Medicine and Biology Society (EMBC)*, Jul. 2019, pp. 2115–2118, doi: 10.1109/EMBC.2019.8856687.

[94] A. J. Yezzi and J. L. Prince, "An Eulerian PDE Approach for Computing Tissue Thickness," *IEEE Trans. Med. Imaging*, vol. 22, no. 10, pp. 1332–1339, Oct. 2003, doi: 10.1109/TMI.2003.817775.

[95] C. Barnabe *et al.*, "Reproducible metacarpal joint space width measurements using 3D analysis of images acquired with high-resolution peripheral quantitative computed

tomography," *Med. Eng. Phys.*, vol. 35, no. 10, pp. 1540–1544, Oct. 2013, doi: 10.1016/j.medengphy.2013.04.003.

[96] S. Boutroy *et al.*, "Importance Of Hand Positioning In 3D Joint Space Morphology Assessment," *Arthritis Rheum. Rheum.*, vol. 65, pp. S840–S841, 2013.

[97] A. J. Burghardt *et al.*, "Quantitative in vivo HR-pQCT imaging of 3D wrist and metacarpophalangeal joint space width in rheumatoid arthritis," *Ann. Biomed. Eng.*, vol. 41, no. 12, pp. 2553–2564, 2013, doi: 10.1007/s10439-013-0871-x.

[98] K. S. Stok *et al.*, "Consensus approach for 3D joint space width of metacarpophalangeal joints of rheumatoid arthritis patients using high-resolution peripheral quantitative computed tomography," *Quant. Imaging Med. Surg.*, vol. 10, no. 2, pp. 314–325, Feb. 2020, doi: 10.21037/qims.2019.12.11.

[99] P. Durongbhan, C. E. Davey, and K. S. Stok, "SPHARM-PDM based image preprocessing pipeline for quantitative morphometric analysis (QMA) for in situ joint assessment in rabbit and rat models," *Sci. Reports 2022 121*, vol. 12, no. 1, pp. 1–12, Jan. 2022, doi: 10.1038/s41598-021-04542-8.

[100] P. Durongbhan *et al.*, "A microCT imaging protocol for reproducible and efficient quantitative morphometric analysis (QMA) of joint structures of the in situ mouse tibio-femoral joint," *Bone*, vol. 166, p. 116606, Nov. 2023, doi: 10.1016/J.BONE.2022.116606.

[101] T. D. Turmezei *et al.*, "Quantitative three-dimensional assessment of knee joint space width from weight-bearing CT," *Radiology*, vol. 299, no. 3, pp. 649–659, Jun. 2021, doi: 10.1148/RADIOL.2021203928.

[102] N. Charon, A. Islam, and W. Zbijewski, "Landmark-free morphometric analysis of knee osteoarthritis using joint statistical models of bone shape and articular space variability," *J. Med. Imaging*, vol. 8, no. 4, pp. 44001–44002, Jul. 2021, doi: 10.1117/1.JMI.8.4.044001.

[103] L. Sharma *et al.*, "Varus and valgus alignment and incident and progressive knee osteoarthritis," *Ann. Rheum. Dis.*, vol. 69, no. 11, pp. 1940–1945, Nov. 2010, doi: 10.1136/ARD.2010.129742.

[104] K. M. Friedrich *et al.*, “Does joint alignment affect the T2 values of cartilage in patients with knee osteoarthritis?,” *Eur. Radiol.*, vol. 20, no. 6, pp. 1532–1538, Jun. 2010, doi: 10.1007/s00330-009-1689-7.

[105] K. Moisio *et al.*, “Varus-valgus alignment reduced risk of subsequent cartilage loss in the less loaded compartment,” *Arthritis Rheum.*, vol. 63, no. 4, pp. 1002–1009, Apr. 2011, doi: 10.1002/art.30216.

[106] A. Williams, L. Sharma, C. A. McKenzie, P. V. Prasad, and D. Burstein, “Delayed gadolinium-enhanced magnetic resonance imaging of cartilage in knee osteoarthritis: Findings at different radiographic stages of disease and relationship to malalignment,” *Arthritis Rheum.*, vol. 52, no. 11, pp. 3528–3535, Nov. 2005, doi: 10.1002/art.21388.

[107] A. Hirschmann, F. M. Buck, S. F. Fucentese, and C. W. A. Pfirrmann, “Upright CT of the knee: the effect of weight-bearing on joint alignment,” *Eur. Radiol.*, vol. 25, no. 11, pp. 3398–3404, 2015, doi: 10.1007/s00330-015-3756-6.

[108] T. Iranpour-Boroujeni, J. Li, J. A. Lynch, M. Nevitt, and J. Duryea, “A new method to measure anatomic knee alignment for large studies of OA: data from the Osteoarthritis Initiative,” *Osteoarthr. Cartil.*, vol. 22, no. 10, pp. 1668–1674, Oct. 2014, doi: 10.1016/J.JOCA.2014.06.011.

[109] T. D. Turmezei, G. M. Treece, A. H. Gee, and K. E. Poole, “Cortical thickness mapping of the proximal femur: towards a new imaging biomarker of hip osteoarthritis,” *Osteoarthr. Cartil.*, vol. 21, p. S194, Apr. 2013, doi: 10.1016/j.joca.2013.02.408.

[110] Z. Zhou, G. Zhao, R. Kijowski, and F. Liu, “Deep convolutional neural network for segmentation of knee joint anatomy,” *Magn. Reson. Med.*, vol. 80, no. 6, pp. 2759–2770, Dec. 2018, doi: 10.1002/MRM.27229.

[111] V. Pedoia, B. Norman, S. N. Mehany, M. D. Bucknor, T. M. Link, and S. Majumdar, “3D convolutional neural networks for detection and severity staging of meniscus and PFJ cartilage morphological degenerative changes in osteoarthritis and anterior cruciate ligament subjects,” *J. Magn. Reson. Imaging*, vol. 49, no. 2, pp. 400–410, Feb. 2019, doi: 10.1002/JMRI.26246.

[112] M. Styner *et al.*, “Framework for the Statistical Shape Analysis of Brain Structures using

SPHARM-PDM.," *Insight J.*, no. 1071, pp. 242–250, 2006, Accessed: Mar. 06, 2020. [Online]. Available: http://www.ncbi.nlm.nih.gov/pubmed/21941375.

[113] A. Desai *et al.*, "A multi-institute automated segmentation evaluation on a standard dataset: Findings from the international workshop on osteoarthritis imaging segmentation challenge," *Osteoarthr. Cartil.*, vol. 28, pp. S304–S305, Apr. 2020, doi: 10.1016/j.joca.2020.02.477.

[114] F. Eckstein, C. K. Kwoh, and T. M. Link, "Imaging research results from the Osteoarthritis Initiative (OAI): a review and lessons learned 10 years after start of enrolment," *Ann. Rheum. Dis.*, vol. 73, no. 7, pp. 1289–1300, Jul. 2014, doi: 10.1136/ANNRHEUMDIS-2014-205310.

[115] F. Eckstein, D. Burstein, and T. M. Link, "Quantitative MRI of cartilage and bone: degenerative changes in osteoarthritis," *NMR Biomed.*, vol. 19, no. 7, pp. 822–854, Nov. 2006, doi: 10.1002/nbm.1063.

[116] M. D. Newton, L. Junginger, and T. Maerz, "Automated MicroCT-based bone and articular cartilage analysis using iterative shape averaging and atlas-based registration," *Bone*, vol. 137, p. 115417, Aug. 2020, doi: 10.1016/J.BONE.2020.115417.

[117] K. Chiba *et al.*, "Osteoporotic changes of subchondral trabecular bone in osteoarthritis of the knee: A 3-T MRI study," *Osteoporos. Int.*, vol. 23, no. 2, pp. 589–597, Feb. 2012, doi: 10.1007/S00198-011-1585-2.

Supplementary material

Supplementary Table 3-S1: Keywords used for the initial search of literature involving QMA application in the study of OA in tibiofemoral joint using MRI- or CT- based imaging modalities.

Keywords searched
quantitative morphometric analysis osteoarthritis tibia femur
osteoarthritis imaging analysis
quantitative morphometric analysis osteoarthritis preclinical
osteoarthritis quantitative imaging analysis
osteoarthritis quantitative analysis tibiofemoral joint
quantitative imaging measurement of osteoarthritis
osteoarthritis quantitative imaging modality analysis
articular cartilage morphology osteoarthritis
morphology of osteoarthritis subchondral bone
morphology of osteoarthritis articular cartilage
osteoarthritis morphology joint alignment
osteoarthritis joint orientation morphology
osteoarthritis joint angle morphology
osteoarthritis morphology surface contact area
quantitative assessment of osteoarthritis preclinical CT
osteoarthritis CT morphology tibiofemoral
quantitative MRI cortical bone in osteoarthritic knees
morphology MRI cortical bone in osteoarthritic knees
osteoarthritis joint space width MRI
osteoarthritis joint alignment morphology

Chapter 4
Acquisition

MicroCT imaging protocol for
in situ QMA of the mouse knee

Chapter 4

4.1 Chapter introduction

In quantitative morphometric analysis (QMA) of joint tissues, the relative position of each component (i.e., joint pose) influences important disease-specific structural outcomes extracted from the image. During micro-computed tomography (microCT) acquisition, shifting pose and positioning from one scan to the other could vary QMA results and lead to reproducibility issues. Furthermore, reproducibility and accuracy of cartilage QMA are also dependent on the consistent introduction of contrast agent. This chapter presents a solution to minimise the effect of positioning error and contrast agent injection on murine cartilage and joint QMA during the acquisition process.

This chapter is based on the manuscript entitled "A microCT imaging protocol for reproducible and efficient quantitative morphometric analysis (QMA) of joint structures of the *in situ* mouse tibio-femoral joint" which has been **published** in Bone, 166:116606 in January 2023. The image processing section of this manuscript was developed based on the automated image processing workflow which is presented in detail in Chapter 5.

A microCT imaging protocol for reproducible and efficient quantitative morphometric analysis (QMA) of joint structures of the *in situ* mouse tibio-femoral joint

https://doi.org/10.1016/j.bone.2022.116606

Pholpat Durongbhan[1], Mateus O. Silva[1], Zihui Li[1], Niloufar Ansari[1], R. Y. Nigel Kour[1,2], Catherine E. Davey[1], Kathryn S. Stok[1]

[1]Department of Biomedical Engineering, The University of Melbourne, Parkville, Australia

[2]Department of Mechanical Engineering, The University of Melbourne, Parkville, Australia

4.2 Abstract

Micro-computed tomography (microCT) offers a three-dimensional (3D), high-resolution technique for the visualisation and analysis of bone microstructure. Using contrast-enhanced microCT, this capability has been expanded in recent studies to include cartilage morphometry and whole joint measures, known together as quantitative morphometric analysis (QMA). However, one of the main challenges in quantitative analysis of joint images is sensitivity to joint pose and alignment, which may influence measures related to both joint space and joint biomechanics. Thus, this study proposes a novel microCT imaging protocol for reproducible and efficient QMA of in situ mouse tibio-femoral joint. This work consists of two parts: an in situ diffusion kinetics study for a known cationic iodinated contrast agent (CA4+) for QMA of the cartilage, and a joint positioning and image processing workflow for whole joint QMA. In the diffusion kinetics study, 8 mice were injected at both of their tibio-femoral joints with distinct CA4+ concentrations and diffusion times. The mice were scanned at different time points after injection, and evaluated using attenuation and cartilage QMA measures. Results show that cartilage segmentation and QMA could be performed for CA4+ solution at a concentration of 48 mg/ml, and that reliable measurement and quantification of cartilage were achieved after 5 min of diffusion following contrast agent injection. We established the joint positioning and image processing workflow by developing a novel positioning device to control joint pose during scanning, and a spherical harmonics-based image processing workflow to ensure consistent alignment during image processing. Both legs of seven mice were scanned 10 times, 5 prior to receiving CA4+ and 5 after, and evaluated using whole joint QMA parameters. Joint QMA evaluation of the workflow showed excellent reproducibility for both groups; intraclass correlation coefficients ranged from 0.794 to 0.930. These results confirm that the method can be reliably used without contrast agent as its introduction did not cause significant alteration to the measured parameters. Altogether, the proposed imaging protocol enables reproducible and efficient QMA of joint structures in preclinical models.

Keywords: micro-computed tomography; quantitative morphometric analysis; joint imaging; cartilage imaging; morphometry; imaging protocol

4.3 Introduction

Micro-computed tomography (microCT) is a three-dimensional (3D) imaging technique that applies isotropic voxel sizes in the range of 3-50 μm, and produces excellent visualisation of bone structures [1]. This allows monitoring of structural changes of the bone in both preclinical and clinical research, and has previously been used to quantitatively investigate structural changes and remodelling in an animal model of osteoporosis [2], bone response to implantation in healthy [3] and osteoporotic conditions [4], [5], as well as treatment outcomes for musculoskeletal diseases [6]–[8]. Despite its traditional use in imaging bone tissues, developments in new contrast agents have improved our ability to visualise cartilage for *ex vivo* evaluation with microCT [9]–[12], and have enabled quantitative analysis of bone and cartilage structures.

Recent studies [13], [14] from our group have taken advantage of this expanded capability and proposed a suite of seventeen quantitative morphometric analysis (QMA) measures, consisting of traditional bone (bone QMA) and cartilage structural measures (cartilage QMA), as well as novel 3D whole joint metrics (joint QMA) using contrast-enhanced microCT to assess *in situ* joint health in preclinical rat and rabbit models of knee osteoarthritis (OA). Joint QMA includes a joint centre of mass, a vector with magnitude (λ) and orientation (α, β, γ) relative to the principal Cartesian axes describing the relative tibio-femoral position, as well as an angle of twist (τ) between the femur and tibia, measures of joint space width ($JSW_{L/M}$), and a slope and intercept (*m*, χ) of joint contact area under *in silico* joint loading. These measurements were developed in combination with histological assessments to demonstrate sensitivity to structural damage due to OA.

As discussed in these works [13], [14], a primary issue for joint QMA is its high sensitivity to joint alignment. When imaging a non-rigid link (e.g. the tibio-femoral joint), the relative positions of rigid components may influence disease-specific structural parameters extracted from the image [15]. Thus, it is imperative that the relative position of each component be controlled reproducibly in order to compare data either from different animals, or in follow-up scans of the same animal. In previous *in situ* joint QMA studies [13], [14], this was achieved by placing a wedge (approx. 160° angle) behind the dissected knees to control flexion-extension during image acquisition. The images were, then, manually cropped to the defined

volume of interest centred around the joint. Subsequent manual image alignment was done to achieve orientation that enabled joint QMA measures that are reproducible and sensitive to OA.

More recently, automated image alignment was achieved using an approach based on spherical harmonics (SPHARM), mitigating the impact of operator differences and improving image processing efficiency [16]. However, the success of joint QMA results is still, in-part, reliant on the reproducibility of the initial pose of the joint during image acquisition and the correct manual selection of the volume of interest. Wedge placement has performed well in earlier studies involving dissected knees, but is neither anatomically nor biomechanically neutral for intact (undissected) joints in living animal. It is therefore not appropriate for live animal imaging, and also limits the relevance of joint pose results for biomechanical analysis. Consequently, there is still a need for a joint positioning device to control the joint pose for intact animal knees. Coupled with the SPHARM alignment procedures, we hypothesise that more meaningful, accessible, and reproducible joint QMA measurements can be produced.

The original QMA includes cartilage morphometry using intra-articular injection of SiO_2-micro beads, which is not suitable for live animal imaging. However, recent development of a non-toxic, cationic iodinated contrast agent (CA4+) for identification and quantification of glycosaminoglycan in cartilage has facilitated *in vivo* microCT imaging of cartilage [17], [18]. Recent studies [19], [20] have also shown that using CA4+ for contrast-enhanced microCT allows the quantitative assessment of 3D distribution and content of glycosaminoglycan in cartilage tissues. Like other contrast agents, CA4+ concentration and diffusion kinetics have been investigated in *ex vivo* microCT scans of dissected articular cartilage from human [19], bovine [20], [21] and murine [22], [23] samples. Despite the mouse being one of the most commonly used models in musculoskeletal research [24] there is currently no established protocol using CA4+ for imaging of cartilage in the intact whole murine joint.

When considering these issues altogether, there is potential for the development of a microCT imaging protocol that incorporates contrast agent injection and joint positioning control. This work proposes a novel protocol for contrast-enhanced microCT imaging of the mouse tibio-femoral joint that allows for efficient and reproducible measurement of cartilage and joint QMA. Using CA4+ concentrations previously explored in *ex vivo* murine work [22], the diffusion kinetics of CA4+ in the intact mouse tibio-femoral joint is investigated, and a

CA4+ concentration for cartilage visualisation in microCT imaging is determined. Furthermore, a mouse positioning device to control the tibio-femoral joint pose during image acquisition, in conjunction with an image processing workflow, is developed to complete the imaging protocol that allows for reproducible measurement of joint QMA in mouse models using contrast-enhanced microCT.

4.4 Materials and methods

This work is comprised of two components: a diffusion kinetics study of CA4+, and a novel joint positioning device with accompanying image processing workflow (Figure 4-1). A diffusion kinetics study was performed first to determine an appropriate concentration and diffusion time of the contrast agent for cartilage QMA. The results were then applied to the joint positioning workflow development.

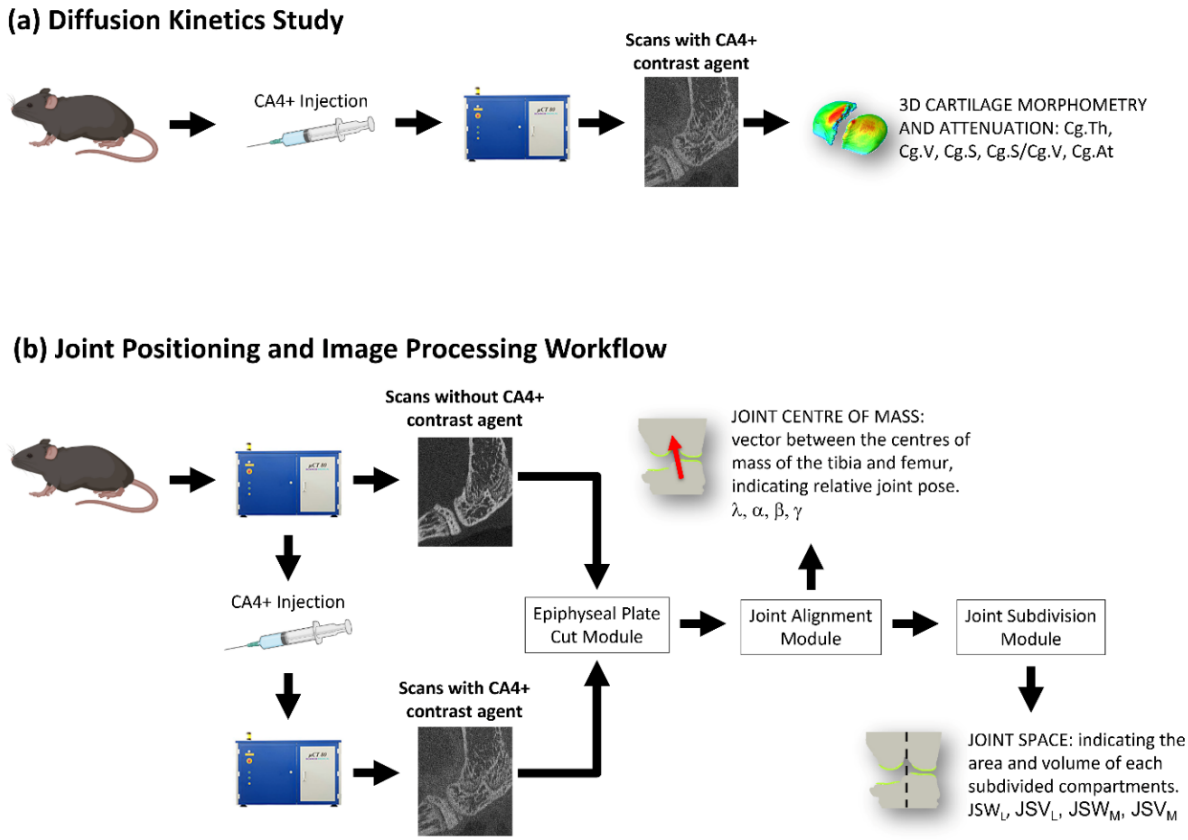

Figure 4-1: Overview schematic of the (a) diffusion kinetics and (b) joint positioning and image processing workflow. The diffusion kinetics study was performed to determine the appropriate CA4+ concentration and diffusion time for imaging of a mouse tibio-femoral joint. The results of the diffusion kinetics were incorporated study (b) into the joint positioning device and image processing workflow. Cg.Th: cartilage thickness; Cg.V: cartilage volume; Cg.S: cartilage surface area; Cg.S/Cg.V: cartilage surface-to-volume ratio; Cg.At: mean cartilage attenuation; λ: magnitude of the joint centre of mass; α, β, γ: orientation angle with respect to x,y,z-axis for the joint centre of mass; JSW: mean joint space width; JSV: joint space volume.

4.4.1 Animals and microCT scan protocols

Melbourne University Animal Ethics Committee approved all animal procedures (AEC# 1614078), which were conducted in accordance with the Australian code for the care and use of animals for scientific research. Fifteen healthy excess male C57BL/6 mice, all within 10 – 20 weeks of age and weighing between 26.9 to 34.2 grams, were sacrificed by cervical dislocation prior to each experiment. Eight mouse carcasses were used to investigate diffusion kinetics, and seven mouse carcasses were used to evaluate the reproducibility of the positioning device and image processing software.

Scans of the tibio-femoral joint were performed using microCT (vivaCT80, Scanco Medical AG, Brüttisellen, Switzerland). To keep the scan time short for frequently repeated scans, the diffusion kinetics study was performed using an integration time of 350 ms, 500 projections, 70 kVp peak voltage, 57 µA peak current, and no frame averaging with each scan taking approximately 10 minutes. To optimise scan quality, the positioning reproducibility study was performed using an integration time of 300 ms, 700 projections, 70 kVp peak voltage, and 114 µA peak current with each scan taking around 30 minutes. All scans were performed at a 10 µm nominal voxel size.

Each microCT scan was reconstructed as a 6.38 GB ISQ file with an x, y, and z dimension of 3198, 3198, and 335 voxels, respectively. The entire dataset of this study is approximately 650.76 GB in size. All scans were filtered using a constrained 3D Gaussian filter ($\sigma = 1.2$, $s = 1$). The menisci and patellae were manually contoured and removed.

4.4.2 Diffusion kinetics study

4.4.2.1 Sample preparation, injection, and imaging

A previous *ex vivo* diffusion kinetics study of the distal femur of the mouse, by Mashiatulla et al. [22], was performed with CA4+ at concentrations of 6, 12, 24, and 48 mg/ml. In that study, 12 mg/ml concentration was deemed optimal based on its clear separation of cartilage from underlying bone in the linear attenuation coefficient histograms. However, concentrations of 24 and 48 mg/ml provided the best signal-to-noise and contrast-to-noise ratio while still providing good cartilage separation as well. In anticipation of the presence of additional soft

tissue in intact joints used in this study, CA4+ at 48 mg/ml concentration was investigated in addition to 12 mg/ml.

CA4+ powder was prepared, as previously described by Joshi et al. [25] and dissolved using ultrapure water (Barnstead MicroPure Water Purification System, Thermo Fisher Scientific, Inc., Waltham, MA, USA), maintaining pH at 7.4 and osmolality at 400 ± 30 mOsm/kg. Each intact mouse tibio-femoral joint received 20 µl of CA4+ solution via intra-articular injection through the patellar tendon using 33G needles (Nanofil Application Kits, World Precision Instruments, Sarasota, FL, USA).

Eight mouse carcasses were randomly divided into two groups (n = 8 joint samples each; both left and right tibio-femoral joints were used). Each mouse was euthanised and processed sequentially. Each carcass was scanned without contrast agent immediately post-euthanasia, then, received an injection of either 12 or 48 mg/ml CA4+ solution into both tibio-femoral joints. The knee was flexed and extended for 30 cycles prior to scanning. The knee was, then, scanned using microCT in succession at 5, 15, 25, and 35 minutes after injection with no interscan period.

4.4.2.2 Validation

After image reconstruction and filtering, all microCT images were visually inspected to determine the enhancement of cartilage and the feasibility of cartilage segmentation. For each scan, tibial cartilage was manually segmented from the greyscale image using protocols previously developed and validated in previous works [13], [14]. The segmentation protocol involved identifying a subvolume which is defined as the region between the medial/lateral margin to the corresponding medial/lateral tubercle of the tibia. Manual contouring then followed regions of moderate attenuation as described by Bansal et al. [17], after which visual inspection was done to ensure accurate segmentation. Mean cartilage attenuation (Cg.At) was calculated [23], as well as cartilage QMA: cartilage thickness (Cg.Th), cartilage surface area (Cg.S), cartilage volume (Cg.V), and cartilage surface-to-volume ratio (Cg.S/Cg.V) [26].

4.4.3 Joint positioning and image processing workflow

4.4.3.1 Novel positioning device

The positioning device was designed to align and secure the ankle joint, tibia and femur along surfaces of the device for consistent landmark location and limb stabilisation, in order to reproducibly constrain the joint without incurring injury. The device was designed as dimensionless STL files (available as supplementary materials) which can be scaled to accommodate different microCT gantry and animal sizes via 3D printing. The device used in this study was made with 3D Fused Deposition Modelling (FDM) of polylactic acid (PLA) for a simple and rapid manufacturing process (Ender-3 Pro, Creality, Figure 4-2a).

The ankle joint of the mouse was secured to the base using a twist-tie ensuring consistent firmness of restraint and reducing likelihood of injury (Figure 4-2b). A middle bracket was then pulled forward gently to restrain and extend the tibia horizontally. Finally, the front bracket is pulled backwards to gently compress the thigh and align the anterior surface of the femur along the front bracket to create a 90° joint angle between the femur and tibia. The natural range of motion for a mouse knee is 45° to 90° flexion, where 90° is equivalent to the neutral position of a standing mouse (i.e. equivalent to full extension in humans) [27]. The mouse tail was inserted into the tail tunnel to assist with centring the mouse trunk on the animal bed.

The positioning device used in this study can accommodate a range of specimen sizes (up to 9.5 cm in body length, tail excluded) by allowing the front and middle brackets to slide back and forth relative to the base. After the desired position has been achieved, the three parts were then be fixed together with a screw by tightening a nut at the top of the device.

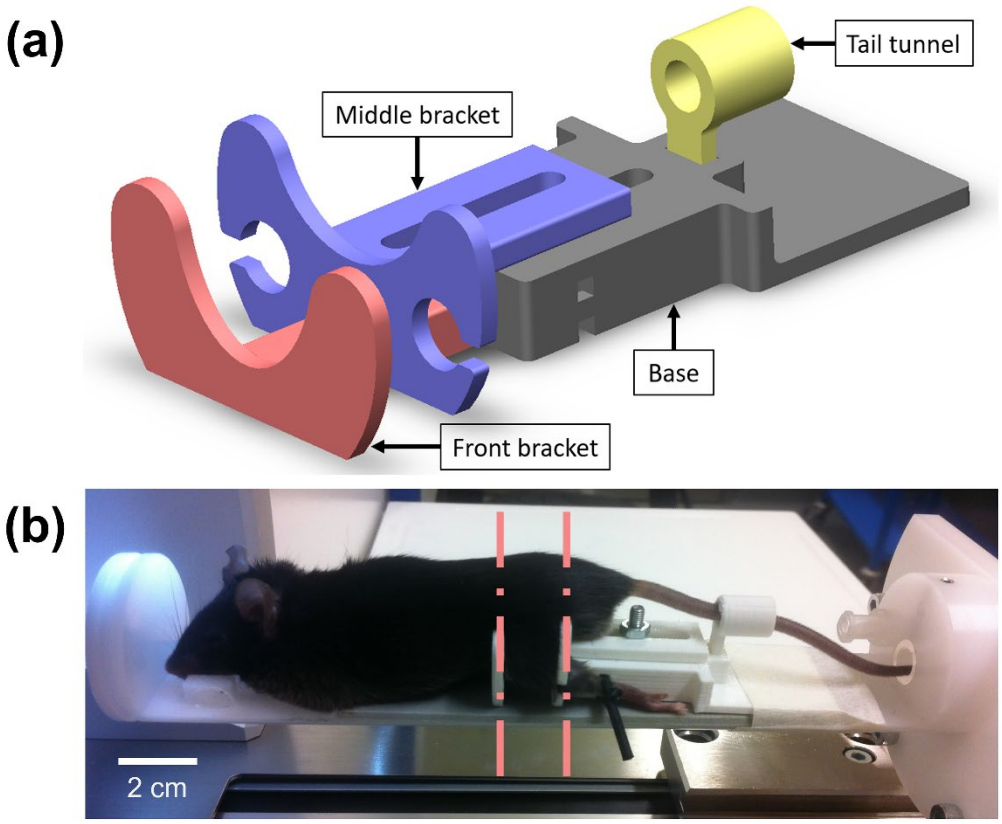

Figure 4-2: (a) The positioning device's structure and (b) its placement on the animal bed of the microCT (vivaCT80), with area between the dashed line showing the scanning region of interest.

4.4.3.2 Sample preparation

Seven mice (n = 14 tibio-femoral joint samples) carcasses were scanned 10 times each: 5 scans prior to receiving CA4+ injection and 5 scans after receiving CA4+ injection. The mice were removed and placed back in the positioning device between every scan. CA4+ concentration of 48 mg/ml was used, as determined from the diffusion kinetics experiment. Mice were placed in the positioning device, as described in Section 4.4.3.1. The scanning region of interest was defined to include the tibio-femoral joint (Figure 4-2b). Following reconstruction and Gaussian filtration, the femur and tibia were automatically segmented from the image as previously described for further processing [28].

4.4.3.3 Image preprocessing workflow

As the volume of interest for joint QMA metrics is defined with epiphyseal plates of the femur and the tibia as the upper and lower limit, respectively, joint images in earlier works had been manually cropped to remove the diaphysis and metaphysis prior to the manual processes of alignment and subdivision. Despite the automation of the latter two processes [16], a cropped

joint volume of interest was still expected as input. Consequently, direct application of the automated workflow was not possible, and manual volume of interest selection is still necessary.

In previous work we developed automated joint alignment and subdivision software, based on SPHARM statistical shape modelling and persistence homology [16] to mitigate orientation errors during image acquisition and ensure consistent joint QMA measurements. In this study, the software was expanded to perform epiphysis selection in a semi-automated manner. An average statistical shape was calculated from the dataset using SPHARM, and a 3D plane selected to crop at the epiphyseal plate of the average shape. Transformation between the average shape and each individual shape was determined, and the 3D cropping plane expressed in the coordinates of the individual shape. The resulting cropped shapes were then processed through the existing automated alignment workflow [16] without any further adjustment.

4.4.3.4 3D joint QMA validation

Two joint QMA parameters, both sensitive to tibio-femoral angle [13], [16], were used to evaluate the reproducibility of the positioning and processing protocol, namely, joint centre of mass and joint space. The joint centre of mass, a vector pointing from the centre of mass of the tibia to the femur with magnitude λ (mm), and orientation (α [°], β [°], and γ [°]), is measured along the three principal axes of the Cartesian coordinate system [13]. Measurement of joint space included mean joint space width ($JSW_{L/M}$, mm), and joint space volume ($JSV_{L/M}$, mm^3), was calculated for both the medial (M) and lateral (L) compartment of each joint [29]. Visual inspections were done for all joint QMA measurements to confirm accuracy prior to statistical analysis.

4.4.4 Statistics

4.4.4.1 Diffusion kinetics study

A preferred concentration of CA4+ and diffusion time between injection and scanning were chosen for the subsequent experiments based on their contrast enhancement of the cartilage and their ability to allow for consistent measurements of cartilage QMA. Values for Cg.Th, Cg.S, Cg.V, Cg.S/Cg.V, Cg.At between time points were plotted and their consistency observed visually.

4.4.4.2 Joint positioning device and image processing workflow development

Shapiro-Wilk's test was performed to verify that the data was normally distributed, using GraphPad Prism (Version 8.0.0, GraphPad Software, Inc., San Diego, CA, USA). To evaluate the impact of the CA4+ contrast agent, paired t-tests were applied between groups with, and without, CA4+ for the joint QMA variables (λ, α, β, γ, $JSW_{L/M}$, and $JSV_{L/M}$), where p-values less than 0.05 were considered significant. Reproducibility of the same QMA variables was assessed using RStudio (Version 0.95.258, RStudio, PBC., Boston, MA, USA). To test the absolute agreement between each measurement [30], precision error, expressed both in absolute value (PE(SD)) and as a coefficient of variation (PE%CV), and intraclass correlation coefficient (two-way random effects, consistency, multiple measurements ICC [31]) with 95% confidence interval (CI), were calculated. Reproducibility, measured as ICC with values ranging from 0 to 1, is classified as excellent for values higher than 0.75 [32]. Good, fair, and poor reproducibility are classified when ICC values range from 0.6 to 0.74, 0.40 to 0.59, and 0 to 0.4, respectively [32].

4.5 Results

4.5.1 Diffusion kinetics study

We first determined an appropriate concentration of the contrast agent for cartilage QMA for our study. With visual inspection, the contrast of the cartilage was not effectively enhanced by injecting 12 mg/ml CA4+ in the tibio-femoral joint, making cartilage segmentation and subsequent attenuation and QMA calculations unfeasible (Figure 4-3). Similarly, it was not possible to segment and process cartilage in pre-injection scans (Figure 4-3) due to poor visualisation. Cartilage attenuation was sufficient for samples injected with CA4+ solution at 48 mg/ml concentration (Figure 4-3), and were subsequently segmented and analysed. Figure 4-4 shows a representative example of a resulting segmented 3D bone structure of the mouse tibio-femoral joint (Figure 4-4a) and a typical thickness map of tibial cartilage (Figure 4-4b). Plots of cartilage QMA and mean attenuation for each time point (5, 15, 25, and 35 minutes after injection) are shown in Figure 4-5. Visual inspection showed that the resulting cartilage QMA parameters for each sample were consistent throughout each time point with cartilage attenuation slightly increasing as time progressed.

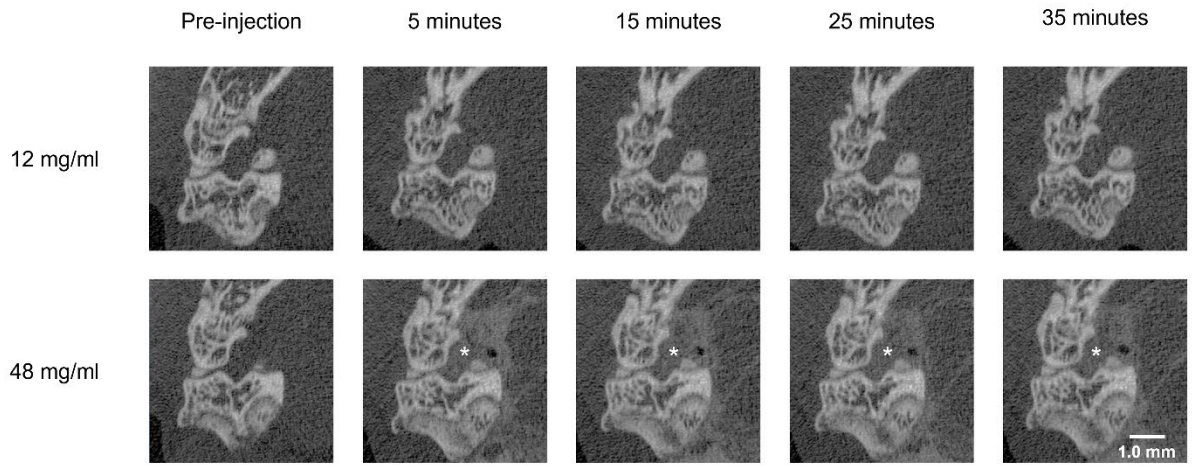

Figure 4-3: In the diffusion kinetics study of CA4+ in mouse articular cartilage, mice carcasses were injected intra-articularly with 12 or 48 mg/ml of CA4+ contrast agent, and imaged 5, 15, 25, and 35 minutes after injection. Representative microCT images of pre-injection and different time points are shown with asterisks (*) denote area with visible contrast agent. The 12 and 48 mg/ml injections were performed on different carcasses which were repositioned between pre- and post-injection scans. (n = 8 tibio-femoral joint samples per group)

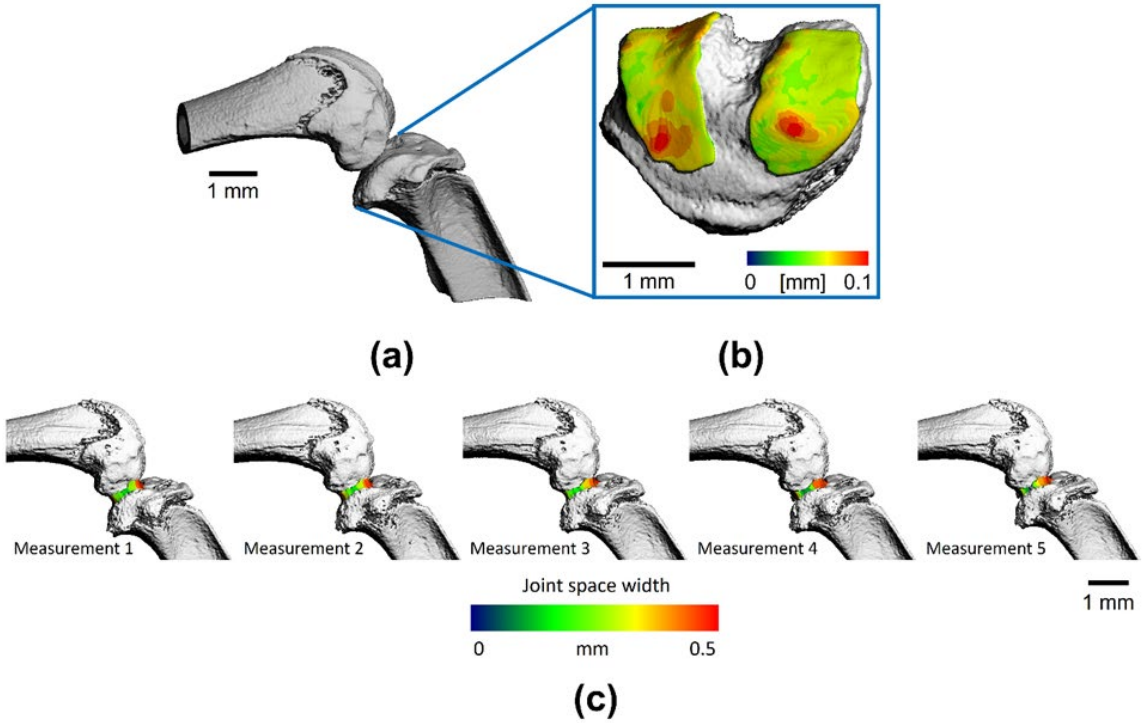

Figure 4-4: Typical results obtained using the imaging protocols proposed in this study, showing (a) a 3D structure of the mouse tibio-femoral joint, (b) a thickness map of the tibial cartilage, and (c) repeated measurements of the same sample with joint space width mapped.

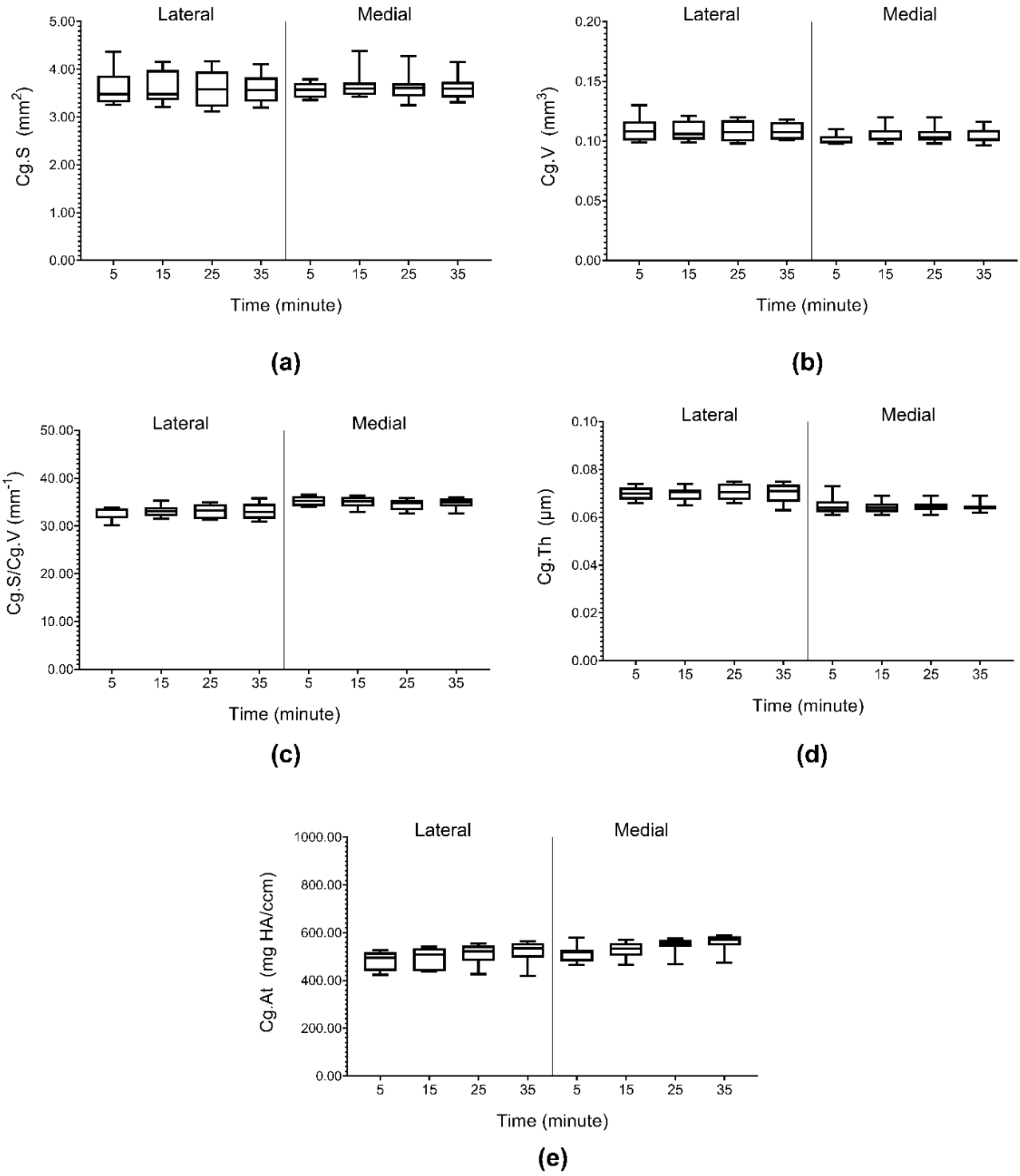

Figure 4-5: Cartilage QMA and attenuation results from the diffusion kinetics study at different time points for samples injected with CA4+ concentration of 48 mg/ml, showing cartilage measurements for (a) surface, (b) volume, (c) surface to volume ratio, (d) thickness, and (e) mean attenuation. Horizontal dash indicates the mean for each time point (n = 8 tibio-femoral joint samples).

4.5.2 Joint positioning and image processing workflow

Visual inspections confirmed accurate joint QMA results with typical result shown in Figure 4-4c. Reproducibility values of joint QMA measurements from samples using the joint positioning device and image processing workflow with, and without, CA4+ injections are shown in Table 4-1. Excellent reproducibility (ICC > 0.75) was achieved for all centre of mass and joint space measurements for both cases, with ICC ranging from 0.794 (JSW_L in samples with CA4+) to 0.930 (JSV_M in samples with CA4+). For both groups, precision errors, reported as PE(%CV), are all lower than 10% for all values except JSV_L and JSV_M (10.20% and 10.11% for samples without CA4+, 10.17% and 10.37% for samples with CA4+, respectively). Shapiro-Wilk's test of all measured joint QMA parameters found all normal distributions. Summary statistics of joint QMA for both groups are shown in Table 4-2, with paired t-test results showing no significant differences for all parameters between each group. Box plots of the centre of mass (Figure 4-6a and Figure 4-6b) and joint space measurements (Figure 4-6c and Figure 4-6d) are shown where groups with, and without, CA4+ are plotted side-by-side.

Table 4-1: Reproducibility of joint QMA parameters obtained from samples with, and without, CA4+ injection prior to scanning. Reproducibility is expressed in terms of intraclass correlation coefficients (ICC), and precision errors (PE) expressed in absolute and percentage of the coefficient of variation, of the repeated measure (n = 14 tibio-femoral joint samples, 5 repeated measurements each).

	Control					CA4+				
	ICC	Lower 95%	Upper 95 %	PE (SD)	PE (%CV)	ICC	Lower 95%	Upper 95 %	PE (SD)	PE (%CV)
Centre of mass										
λ (mm)	0.832	0.636	0.939	0.08	2.69%	0.815	0.600	0.933	0.08	0.07%
α (°)	0.912	0.810	0.968	4.08	6.81%	0.917	0.820	0.970	5.18	3.32%
β (°)	0.892	0.766	0.960	2.87	3.03%	0.886	0.752	0.958	3.76	2.93%
γ (°)	0.903	0.789	0.964	4.19	2.79%	0.920	0.827	0.971	5.28	3.32%
Joint space										
JSW (µm)										
Lateral	0.834	0.641	0.939	0.02	9.24%	0.794	0.554	0.925	0.02	8.33%
Medial	0.840	0.654	0.942	0.01	4.03%	0.825	0.609	0.939	0.01	4.63%
JSV (mm^3)										
Lateral	0.825	0.621	0.936	0.00001	10.20%	0.890	0.761	0.960	0.00001	10.17%
Medial	0.859	0.696	0.949	0.00001	10.11%	0.930	0.845	0.976	0.00001	10.37%

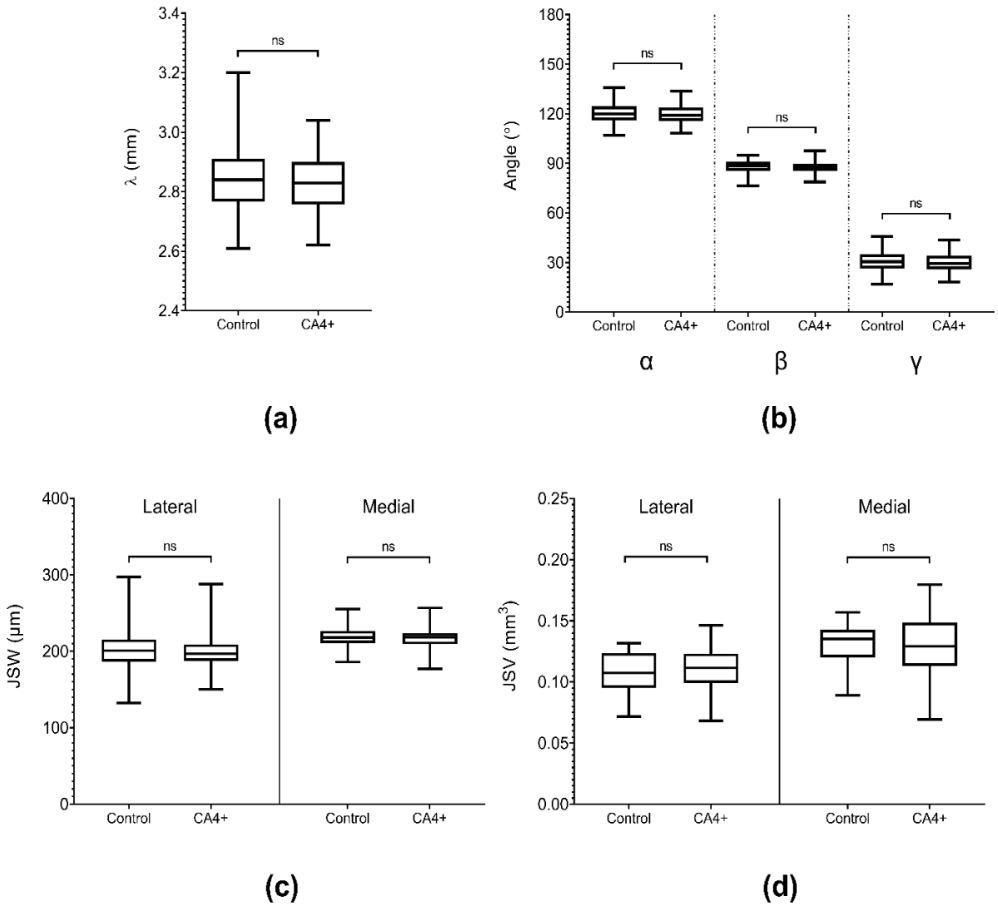

Figure 4-6: Joint QMA results for samples processed using joint positioning and image processing workflow, both with, and without, CA4+ contrast agent injection, showing measurements for (a) magnitude and (b) orientations of the centre of mass, and (c) joint space width where ns indicates no statistically significant difference (n = 14 tibio-femoral joint samples, 5 repeated measurements each).

*Table 4-2: Joint QMA parameters obtained from samples with, and without, CA4+ injection prior to imaging using the joint positioning and image processing workflow. Data expressed as mean ± SD, where ns indicates no statistically significant difference; * and ** indicates statistically significant differences between groups with p-values < 0.05 and 0.01, respectively (n = 14 tibio-femoral joint samples, 5 repeated measurements each).*

	Control		CA4+		
	mean	±SD	mean	±SD	p
Centre of mass					
λ (mm)	2.8	0.1	2.8	0.1	ns
α (˚)	120.6	5.9	120.0	5.2	ns
β (˚)	88.8	3.8	87.5	2.8	ns
γ (˚)	31.1	5.8	30.4	5.3	ns
Joint space					
JSW (µm)					
Lateral	202.4	21.2	198.5	16.4	ns
Medial	218.1	9.5	216.8	11.0	ns
JSV (mm³)					
Lateral	0.11	0.01	0.11	0.01	ns
Medial	0.13	0.01	0.13	0.02	ns

4.6 Discussions

This study proposes a novel microCT imaging protocol for reproducible 3D QMA measurements of intact mouse tibio-femoral joint. The protocol was developed by first studying, based on the results of previous study [22], the diffusion kinetics of CA4+ in intact whole joint to ensure appropriate cartilage visualisation for 3D QMA. This was followed by the design of a novel positioning device and the development of an accompanying image processing workflow to control joint pose and joint orientation during image acquisition and processing. The CA4+ concentration and diffusion time obtained from the diffusion kinetics study allow accurate segmentation that leads to sufficient measurements of cartilage attenuation and consistent quantification of cartilage 3D QMA parameters. The joint positioning and image processing workflow also gives highly reproducible 3D QMA measurements of the joint orientation, joint space width, and joint space volume of both the medial and lateral sites. Combined, the protocol shows that the contrast agent does not interfere with joint 3D QMA measurements in a statistically significant manner. These results demonstrate that controlled positioning and processing allows for comprehensive measurements of 3D QMA parameters [13], [14] using microCT in a reproducible and efficient approach.

4.6.1 Diffusion kinetics study

With a goal of future application of the protocol in live animal scanning, joint integrity must be preserved during the injection process. Thus, in this study, a contrast agent solution volume of 20 µl and a diffusion time of 35 minutes were of interest. This correlates to the maximum injection volume possible without extra-articular leakage [33] and the anaesthetic period of a live mouse under general anaesthesia [34], respectively. Previous CA4+ diffusion kinetics study in *ex vivo* cartilage samples used 12 mg/ml CA4+ solution and an incubation time of 30 to 40 min in micro-centrifuge tubes for cartilage segmentation and QMA from microCT images [22]. For *in situ* intact joints used in this study, however, cartilage contrast was not effectively enhanced using this protocol, due to additional soft tissue structures in the joint that can take up the contrast agent, including ligament and synovium, which were not present in the previous murine *ex vivo* studies [22], [23].

It was found that cartilage segmentation and subsequent QMA was possible using 48 mg/ml concentration of CA4+ solution. Visual inspection showed a slight increase in cartilage attenuation over time due to additional diffusion of the contrast agent into the cartilage tissue. Additional inspections of cartilage QMA results between each time point (5, 15, 25, and 35 minutes after injection) revealed consistent outcomes for all cartilage QMA measurements. With generally small standard deviation, average Cg.S, Cg.V, and Cg.Th evaluated in this study are all similar to those measured in other literature using contrast-enhanced micro- and nanoCT [9], [35], [36] (Cg.S/Cg.V were not reported in those studies). This indicated that visualisation sufficient for the segmentation and accurate QMA of the tibio-femoral joint cartilage could be achieved in the first 5 minutes post-injection using this concentration and protocol.

Limitations of the diffusion kinetics study is the limited number of joint samples and CA4+ concentrations used in this experiment. Even with a previously validated protocol [13], [14], manual cartilage segmentation from contrast-enhanced microCT image remains a time-consuming and visually challenging task for operators. For the 8 samples injected with a CA4+ concentration of 48 mg/ml, a total of 64 cartilage masks were processed at each of the 4 time points just for the tibia alone. Using the findings from this study as a starting point, coupled with future automation of the cartilage segmentation process, a larger study involving more animal samples and more of concentration values would be feasible. Future studies could then focus on applying these protocols to investigate its robustness in scans with cartilage damaged by diseases such as osteoarthritis. Additionally, with regards to the type of contrast agents, this study has focused solely on visualising the cartilage using CA4+. However, other contrast agents could also be considered for this purpose, and their performance measured against this study.

4.6.2 Joint positioning and image processing workflow

Although a reliable registration protocol has been established to control joint positioning and alignment for the purpose of comparing and quantifying changes between rigid structures (e.g. whole bone) in longitudinal microCT images [37], changes in joints, which are non-rigid links, are difficult to quantify accurately since the relative position (i.e. link angle) of joint components can influence structural parameters extracted from the image. It was previously

reported that a 30° shift in human metacarpophalangeal could lead to 16.4% difference in JSW measurement [15]. A consistent joint imaging protocol allows differences observed in the resulting QMA to be attributed to joint disease progression in mature animals rather than acquisition errors. Thus, this study has developed a novel mouse positioning device to control joint pose during image acquisition along with an image processing workflow that aligns the joint to the reference position as part of the imaging protocol and was validated by measuring joint QMA parameters (λ, α, β, γ, $JSW_{L/M}$, and $JSV_{L/M}$). Given that previous studies have validated the sensitivity of these measurements to joint changes caused by OA in rabbit and rat models [13], [14] and that all mice used in this study were healthy, the variations in these parameters could be attributed directly to the quality of the positioning device and the alignment workflow. It can be seen from Table 4-1 that all resulting joint QMA measurements from samples without contrast agent have excellent reproducibility (ICC > 0.75) with ICC ranging from 0.825 to 0.912. The resulting QMA also shows high measurement precision with low precision error (PE(%CV) < 10.37%, Table 4-1) and small standard deviation relative to its mean (Table 4-2). Combined with visual assessment, this points to the ability of the workflow to produce highly reproducible and accurate measurements in samples without contrast agent.

When considering joint QMA from samples injected with contrast agent, it can also be noted from Table 4-1 that the values of ICC and PE(%CV) remained excellent for all measures. Additionally, the paired t-test in Table 4-2 demonstrate that joint QMA obtained from samples with and without CA4+ are not significantly different. This points to the fact that contrast agent injection at this volume and concentration did not interfere with the joint space measurements or attenuation at bone margins which could lead to different bone segmentation results and joint QMA results. This is further demonstrated visually in Figure 4-6 and statistically in Table 4-2, where the mean of all joint QMA measurements in samples with CA4+ are no more than 2.8% different from their control counterpart while maintaining similar standard deviations as well.

Concerning the robustness of the image processing workflow, this work expanded the automatic framework first proposed in earlier work [16] by implementing an epiphyseal plate cut module while using the rest of the framework as previously reported. The original framework performed in a model-invariant manner, was validated in rabbit and rat datasets

without any adjustments. This work further validated that model-invariant property by implementing the alignment and subdivision module, without adjustments, in a new animal model to obtain highly reproducible joint QMA measurements.

4.6.3 Combined imaging protocol

Placing the results of this whole mouse imaging protocol (contrast agent injection, intact joint positioning device, and image processing workflow) in the context of those acquired using a foam wedge on dissected joint from earlier rabbit [13] and rat [14] studies, where joints were manually cropped at the epiphyseal plate, and processed using the automatic image processing workflow described in [16], it can be seen that the reproducibility of joint QMA from earlier studies (Table 4-S1) have slightly higher ICC and lower PE(%CV) than those obtained using this imaging protocol. This could be due to the difference in joint pose used in these studies where controlling the positions of excised joints was relatively easier to perform. In earlier studies [13], [14], rabbit and rat knees were excised and their pose controlled by placing a foam wedge with 160° angle before being placed in the sample tube for scanning. In this work, the entire mouse carcass was placed onto the positioning device and scanned as is. Nevertheless, all QMA measurements done in this study still demonstrated excellent reproducibility (ICC > 0.75) [32], bypassing the need to excise animal joints for scanning. Future studies of the preclinical mouse model of tibio-femoral joint disease could potentially make use of these cartilage and joint QMA results from healthy mice in this study as a baseline control to compare and build a database of pathological QMA.

It should be noted that even though the protocol in this study was designed to be used with the *in vivo* microCT (vivaCT80), high energy level (70 kVp) and long X-ray exposure time (300 ms integration time, 700 projections) were used. This allows the acquisition of images with high resolution and signal-to-noise ratio, at the cost of potentially exposing the animals to high levels of ionising radiation. However, a previous longitudinal study by Brouwers et al. [38] has indicated that the radiation exposure using those settings is still within the acceptable range. Their study used the same energy level (70 kVp) and longer exposure time (350 ms integration time, 1000 projections) to acquire images of the rat knee with *in vivo* microCT from the same manufacturer (vivaCT40) and reported no radiation effects on bone morphometry over 9 successive scans [38]. As radiation accumulates with each subsequent

scan and could affect structural developments, future longitudinal studies should consider the trade-off between image quality and radiation exposure.

With radiation exposure considered, the protocol can be deployed in future *in vivo* longitudinal studies of joint disease progression such as osteoarthritis in animal models. In addition to uncovering structural changes in the bone, cartilage, and the whole joint, this protocol can also unveil longitudinal changes to the glycosaminoglycan content in cartilage tissues [19], [20].

4.7 Conclusion

Reproducible quantitative morphometric analysis of the joint is dependent on consistent contrast agent injection, joint pose, and joint orientation. In this work, the diffusion kinetics of the contrast agent CA4+ was explored in intact whole joints, and a novel joint positioning device and accompanying image processing workflow was developed as part of the proposed imaging protocol using contrast-enhanced microCT for high quality and reproducible QMA of intact mouse tibio-femoral joints. Contrast agent concentration of 48 mg/ml and injection protocol explored in this study has allowed consistent measurements of cartilage QMA and attenuation while not inducing significant changes in joint orientation, joint space width, and joint space volume measurements. Additionally, the novel joint positioning and image processing workflow has led to reproducible and consistent measurements of joint QMA which can be deployed with or without contrast agent injection. This imaging protocol could facilitate future longitudinal comparison of microCT images in live animals for tracking dynamic structural changes in bone and cartilage, as well as changes to the whole joint, in the progression of joint diseases such as osteoarthritis, providing a valuable tool for understanding its development, especially in early stages.

4.8 Acknowledgement

This work was supported by the Discovery Projects scheme from Australian Research Council (DP180101838), an Early Career Researcher Grant from the University of Melbourne, and a 2018 Selby Research Award. We thank Benjamin Lakin, Jonathan D. Freedman, and Mark W. Grinstaff for their provision of CA4+ contrast agent.

References

[1] M. L. Bouxsein, S. K. Boyd, B. A. Christiansen, R. E. Guldberg, K. J. Jepsen, and R. Müller, "Guidelines for assessment of bone microstructure in rodents using micro-computed tomography," *J. Bone Miner. Res.*, vol. 25, no. 7, pp. 1468–1486, Jun. 2010, doi: 10.1002/jbmr.141.

[2] F. M. Lambers, G. Kuhn, F. A. Schulte, K. Koch, and R. Müller, "Longitudinal assessment of in vivo bone dynamics in a mouse tail model of postmenopausal osteoporosis," *Calcif. Tissue Int.*, vol. 90, no. 2, pp. 108–119, Feb. 2012, doi: 10.1007/S00223-011-9553-6.

[3] Z. Li *et al.*, "In vivo monitoring of bone architecture and remodeling after implant insertion: The different responses of cortical and trabecular bone," *Bone*, vol. 81, pp. 468–477, Dec. 2015, doi: 10.1016/j.bone.2015.08.017.

[4] Z. Li, G. Kuhn, M. Schirmer, R. Mü Ller, D. Ruffoni, and A. A. Zadpoor, "Impaired bone formation in ovariectomized mice reduces implant integration as indicated by longitudinal in vivo micro-computed tomography," 2017, doi: 10.1371/journal.pone.0184835.

[5] Z. Li, R. Müller, and D. Ruffoni, "Bone remodeling and mechanobiology around implants: Insights from small animal imaging," *J. Orthop. Res.*, vol. 36, no. 2, pp. 584–593, Nov. 2017, doi: 10.1002/jor.23758.

[6] U. Kettenberger, J. Ston, E. Thein, P. Procter, and D. P. Pioletti, "Does locally delivered Zoledronate influence peri-implant bone formation? - Spatio-temporal monitoring of bone remodeling in vivo," *Biomaterials*, vol. 35, no. 37, pp. 9995–10006, Dec. 2014, doi: 10.1016/j.biomaterials.2014.09.005.

[7] F. M. Lambers, G. Kuhn, C. Weigt, K. M. Koch, F. A. Schulte, and R. Müller, "Bone adaptation to cyclic loading in murine caudal vertebrae is maintained with age and directly correlated to the local micromechanical environment," *J. Biomech.*, vol. 48, no. 6, pp. 1179–1187, Apr. 2015, doi: 10.1016/j.jbiomech.2014.11.020.

[8] A. Roshan-Ghias, F. M. Lambers, M. Gholam-Rezaee, R. Müller, and D. P. Pioletti, "In vivo loading increases mechanical properties of scaffold by affecting bone formation

and bone resorption rates," *Bone*, vol. 49, no. 6, pp. 1357–1364, Dec. 2011, doi: 10.1016/j.bone.2011.09.040.

[9] M. Z. C. Ruan, B. Dawson, M.-M. Jiang, F. Gannon, M. Heggeness, and B. H. L. Lee, "Quantitative imaging of murine osteoarthritic cartilage by phase-contrast micro-computed tomography," *Arthritis Rheum.*, vol. 65, no. 2, pp. 388–396, Feb. 2013, doi: 10.1002/art.37766.

[10] T. M. Piscaer *et al.*, "In vivo imaging of cartilage degeneration using µCT-arthrography," *Osteoarthr. Cartil.*, vol. 16, no. 9, pp. 1011–1017, Sep. 2008, doi: 10.1016/J.JOCA.2008.01.012.

[11] L. N. M. Hayward, C. M. J. de Bakker, L. C. Gerstenfeld, M. W. Grinstaff, and E. F. Morgan, "Assessment of contrast-enhanced computed tomography for imaging of cartilage during fracture healing," *J. Orthop. Res.*, vol. 31, no. 4, pp. 567–573, Apr. 2013, doi: 10.1002/jor.22265.

[12] P. N. Bansal, N. S. Joshi, V. Entezari, M. W. Grinstaff, and B. D. Snyder, "Contrast Enhanced Computed Tomography can predict the glycosaminoglycan content and biomechanical properties of articular cartilage," *Osteoarthr. Cartil.*, vol. 18, no. 2, pp. 184–191, Feb. 2010, doi: 10.1016/J.JOCA.2009.09.003.

[13] K. S. Stok *et al.*, "Three-Dimensional Quantitative Morphometric Analysis (QMA) for In Situ Joint and Tissue Assessment of Osteoarthritis in a Preclinical Rabbit Disease Model," *PLoS One*, vol. 11, no. 1, p. e0147564, Jan. 2016, doi: 10.1371/journal.pone.0147564.

[14] B. A. Besler *et al.*, "Quantitative measures of bone shape, cartilage morphometry and joint alignment are associated with disease in an ACLT and MMx rat model of osteoarthritis," *Bone*, vol. 146, p. 115903, Feb. 2021, doi: 10.1016/j.bone.2021.115903.

[15] S. Boutroy *et al.*, "Importance Of Hand Positioning In 3D Joint Space Morphology Assessment," *Arthritis Rheum.*, vol. 65, pp. S840–S841, 2013.

[16] P. Durongbhan, C. E. Davey, and K. S. Stok, "SPHARM-PDM based image preprocessing pipeline for quantitative morphometric analysis (QMA) for in situ joint assessment in rabbit and rat models," *Sci. Rep.*, vol. 12, p. 1113, Jan. 2022, doi: 10.1038/s41598-021-

04542-8.

[17] P. N. Bansal *et al.*, “Cationic contrast agents improve quantification of glycosaminoglycan (GAG) content by contrast enhanced CT imaging of cartilage,” *J. Orthop. Res.*, vol. 29, no. 5, pp. 704–709, May 2011, doi: 10.1002/JOR.21312.

[18] R. C. Stewart *et al.*, “Contrast-enhanced CT with a High-Affinity Cationic Contrast Agent for Imaging ex Vivo Bovine, Intact ex Vivo Rabbit, and in Vivo Rabbit Cartilage,” *Radiology*, vol. 266, no. 1, pp. 141–150, Jan. 2013, doi: 10.1148/radiol.12112246.

[19] B. A. Lakin, D. J. Ellis, J. S. Shelofsky, J. D. Freedman, M. W. Grinstaff, and B. D. Snyder, “Contrast-enhanced CT facilitates rapid, non-destructive assessment of cartilage and bone properties of the human metacarpal,” *Osteoarthr. Cartil.*, vol. 23, no. 12, pp. 2158–2166, Dec. 2015, doi: 10.1016/j.joca.2015.05.033.

[20] M. A. Boos, M. W. Grinstaff, S. R. Lamandé, and K. S. Stok, “Contrast-Enhanced Micro–Computed Tomography for 3D Visualization and Quantification of Glycosaminoglycans in Different Cartilage Types,” *Cartilage*, vol. 13, no. 2_suppl, pp. 486S-494S, Dec. 2021, doi: 10.1177/19476035211053820.

[21] B. A. Lakin, D. J. Grasso, R. C. Stewart, J. D. Freedman, B. D. Snyder, and M. W. Grinstaff, “Contrast enhanced CT attenuation correlates with the GAG content of bovine meniscus,” *J. Orthop. Res.*, vol. 31, no. 11, p. n/a-n/a, Jul. 2013, doi: 10.1002/jor.22421.

[22] M. Mashiatulla *et al.*, “Murine articular cartilage morphology and compositional quantification with high resolution cationic contrast-enhanced μCT,” *J. Orthop. Res.*, vol. 35, no. 12, pp. 2740–2748, Dec. 2017, doi: 10.1002/jor.23595.

[23] B. A. Lakin *et al.*, “Contrast-enhanced CT using a cationic contrast agent enables non-destructive assessment of the biochemical and biomechanical properties of mouse tibial plateau cartilage,” *J. Orthop. Res.*, vol. 34, no. 7, pp. 1130–1138, Jul. 2016, doi: 10.1002/jor.23141.

[24] M. H. Gregory, N. Capito, K. Kuroki, A. M. Stoker, J. L. Cook, and S. L. Sherman, “A review of translational animal models for knee osteoarthritis.,” *Arthritis*, vol. 2012, p. 764621, Dec. 2012, doi: 10.1155/2012/764621.

[25] N. S. Joshi, P. N. Bansal, R. C. Stewart, B. D. Snyder, and M. W. Grinstaff, “Effect of Contrast Agent Charge on Visualization of Articular Cartilage Using Computed Tomography: Exploiting Electrostatic Interactions for Improved Sensitivity,” *J. Am. Chem. Soc.*, vol. 131, no. 37, pp. 13234–13235, Sep. 2009, doi: 10.1021/ja9053306.

[26] K. S. Stok and R. Müller, “Morphometric characterization of murine articular cartilage-Novel application of confocal laser scanning microscopy,” *Microsc. Res. Tech.*, vol. 72, no. 9, pp. 650–658, Sep. 2009, doi: 10.1002/jemt.20713.

[27] X. Hu, J. P. Charles, T. Akay, J. R. Hutchinson, and S. S. Blemker, “Are mice good models for human neuromuscular disease? Comparing muscle excursions in walking between mice and humans,” *Skelet. Muscle*, vol. 7, no. 1, pp. 1–14, Nov. 2017, doi: 10.1186/S13395-017-0143-9.

[28] K. S. Stok *et al.*, “Revealing the interplay of bone and cartilage in osteoarthritis through multimodal imaging of murine joints,” *Bone*, vol. 45, no. 3, pp. 414–422, Sep. 2009, doi: 10.1016/j.bone.2009.05.017.

[29] K. S. Stok *et al.*, “Consensus approach for 3D joint space width of metacarpophalangeal joints of rheumatoid arthritis patients using high-resolution peripheral quantitative computed tomography,” *Quant. Imaging Med. Surg.*, vol. 10, no. 2, pp. 314–325, Feb. 2020, doi: 10.21037/qims.2019.12.11.

[30] T. Kohler, M. Beyeler, D. Webster, and R. Müller, “Compartmental bone morphometry in the mouse femur: reproducibility and resolution dependence of microtomographic measurements.,” *Calcif. Tissue Int.*, vol. 77, no. 5, pp. 281–90, Nov. 2005, doi: 10.1007/s00223-005-0039-2.

[31] T. K. Koo and M. Y. Li, “A Guideline of Selecting and Reporting Intraclass Correlation Coefficients for Reliability Research,” *J. Chiropr. Med.*, vol. 15, no. 2, pp. 155–163, Jun. 2016, doi: 10.1016/j.jcm.2016.02.012.

[32] D. V. Cicchetti, “Guidelines, Criteria, and Rules of Thumb for Evaluating Normed and Standardized Assessment Instruments in Psychology,” *Psychol. Assess.*, vol. 6, no. 4, pp. 284–290, 1994, doi: 10.1037/1040-3590.6.4.284.

[33] R. Akagi *et al.*, “Effective knock down of matrix metalloproteinase-13 by an intra-

articular injection of small interfering RNA (siRNA) in a murine surgically-induced osteoarthritis model," *J. Orthop. Res.*, vol. 32, no. 9, pp. 1175–1180, Sep. 2014, doi: 10.1002/JOR.22654.

[34] A. Tsukamoto, K. Serizawa, R. Sato, J. Yamazaki, and T. Inomata, "Vital signs monitoring during injectable and inhalant anesthesia inmice," *Exp. Anim.*, vol. 64, no. 1, p. 57, 2015, doi: 10.1538/EXPANIM.14-0050.

[35] G. Kerckhofs, J. Sainz, M. Wevers, T. Van De Putte, and J. Schrooten, "Contrast-enhanced nanofocus computed tomography images the cartilage subtissue architecture in three dimensions," *Eur. Cell. Mater.*, vol. 25, pp. 179–189, 2013, doi: 10.22203/ECM.V025A13.

[36] P. Das Neves Borges, A. E. Forte, T. L. Vincent, D. Dini, and M. Marenzana, "Rapid, automated imaging of mouse articular cartilage by microCT for early detection of osteoarthritis and finite element modelling of joint mechanics," *Osteoarthr. Cartil.*, vol. 22, no. 10, pp. 1419–1428, Oct. 2014, doi: 10.1016/J.JOCA.2014.07.014.

[37] F. A. Schulte, F. M. Lambers, G. Kuhn, and R. Müller, "In vivo micro-computed tomography allows direct three-dimensional quantification of both bone formation and bone resorption parameters using time-lapsed imaging," *Bone*, vol. 48, no. 3, pp. 433–442, Mar. 2011, doi: 10.1016/J.BONE.2010.10.007.

[38] J. E. M. Brouwers, B. Van Rietbergen, and R. Huiskes, "No effects of in vivo micro-CT radiation on structural parameters and bone marrow cells in proximal tibia of wistar rats detected after eight weekly scans," *J. Orthop. Res.*, vol. 25, no. 10, pp. 1325–1332, Oct. 2007, doi: 10.1002/JOR.20439.

Supplementary material

Reproducibility results from earlier study automating the image processing workflow

Supplementary Table 4-S1: Reproducibility of relevant joint QMA parameters from the earlier study automating the image processing workflow using rat and rabbit data [16]. Values are in terms of intraclass correlation coefficient (ICC) and precision errors (PE) expressed in absolute and a percentage of the coefficient of variation of the repeated measure.

Rat [16] (10 µm voxel size, 21 tibiofemoral joint samples, 4 repeated scans each)					
	ICC	Lower 95%	Upper 95 %	PE (SD)	PE (%CV)
Centre of mass					
α (°)	0.955	0.891	0.986	1.90	1.80%
β (°)	0.958	0.899	0.987	1.45	1.62%
γ (°)	0.951	0.884	0.985	1.67	1.06%
Joint space					
JSW (µm)					
Lateral	0.946	0.871	0.983	0.01	0.86%
Medial	0.943	0.866	0.982	0.01	2.26%
JSV (mm^3)					
Lateral	0.952	0.886	0.985	0.04	2.41%
Medial	0.905	0.785	0.970	0.09	5.44%
Rabbit [16] (18 µm voxel size, 6 tibiofemoral joint samples, 4 repeated scans each)					
	ICC	Lower 95%	Upper 95 %	PE (SD)	PE (%CV)
Centre of mass					
α (°)	0.936	0.796	0.990	1.87	1.96%
β (°)	0.920	0.753	0.987	1.63	1.82%
γ (°)	0.934	0.790	0.989	1.29	0.76%
Joint space					
JSW (µm)					
Lateral	0.907	0.719	0.985	0.05	2.61%
Medial	0.941	0.811	0.991	0.04	2.20%
JSV (mm^3)					
Lateral	0.955	0.853	0.993	0.01	3.96%
Medial	0.907	0.717	0.985	0.01	4.17%

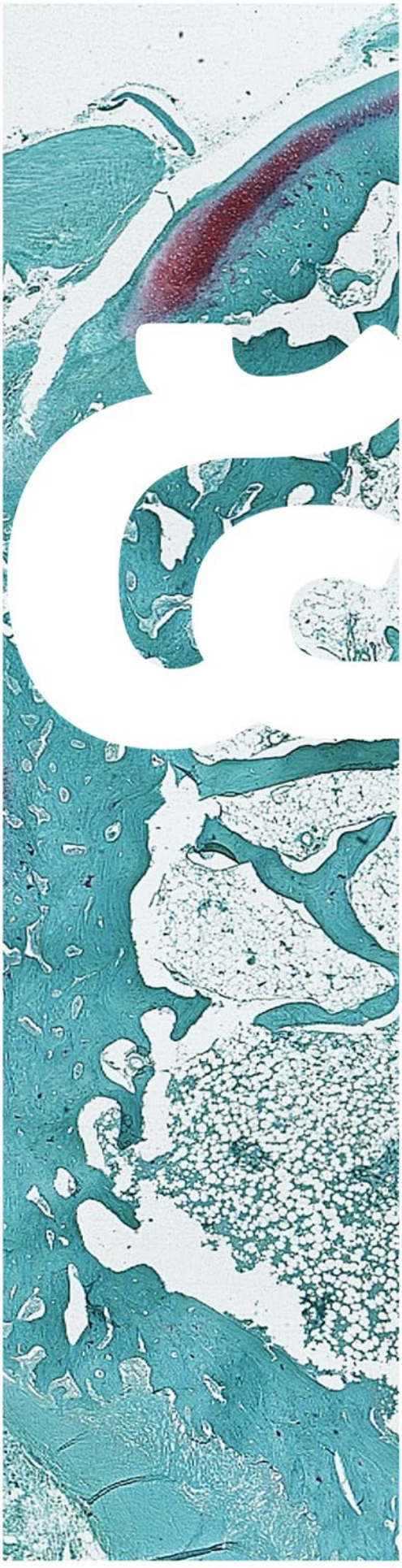

Chapter 5
Processing

Automatic QMA workflow based on morphological representation

Chapter 5

5.1 Chapter introduction

Many joint quantitative morphometric analysis (QMA) metrics are defined relative to the coordinate system of the acquired images. Differences between the orientation of each joint relative to their local coordinate system lead to alignment errors in joint QMA measurements. To obtain reproducible joint QMA, joint images must be aligned to a common reference coordinate system which is constant from one scan to the other. Adjusting for this alignment error was traditionally performed manually, which is time-consuming and prone to operator bias. This chapter presents an automatic solution using morphological representation to correct these alignment shifts for reproducible and efficient QMA of the joint.

This chapter is based on the manuscript entitled "SPHARM-PDM based image preprocessing pipeline for quantitative morphometric analysis (QMA) for in situ joint assessment in rabbit and rat models" which has been **published** in Scientific Reports, 12(1):1113 in January 2022.

SPHARM-PDM based image preprocessing pipeline for quantitative morphometric analysis (QMA) for in situ joint assessment in rabbit and rat models

https://doi.org/10.1038/s41598-021-04542-8

Pholpat Durongbhan[1], Catherine E. Davey[1], Kathryn S. Stok[1]

[1]Department of Biomedical Engineering, The University of Melbourne, Parkville, Australia

5.2 Abstract

The accessibility of quantitative measurements of joint morphometry depends on appropriate tibial alignment and volume of interest (VOI) selection of joint compartments; often a challenging and time-consuming manual task. In this work, we developed a novel automatic, efficient, and model-invariant image preprocessing pipeline that allows for highly reproducible 3D quantitative morphometric analysis (QMA) of the joint. The pipeline addresses the problem by deploying two modules: an alignment module and a subdivision module. Alignment is achieved by representing the tibia in its basic form using lower degree spherical harmonic basis functions and aligning using principal component analysis. The second module subdivides the joint into lateral and medial VOIs via a watershedding approach based on persistence homology. Multiple repeated micro-computed tomography scans of small (rat) and medium (rabbit) animal knees were processed using the pipeline to demonstrate model invariance. Existing QMA was performed to evaluate the pipeline's ability to generate reproducible measurements. Intraclass correlation coefficient and mean-normalised root-mean-squared error of more than 0.75 and lower than 9.5%, respectively, were achieved for joint centre of mass, joint contact area under virtual loading, joint space width, and joint space volume. Processing time and technical requirements were reduced compared to manual processing in previous studies.

5.3 Introduction

Recent advances in 3-dimensional (3D) image acquisition methods have allowed high-resolution medical images to be readily available, both clinically and preclinically [1]. This, coupled with an exponential increase in computing capability of modern devices, has led to rapid developments in the field of 3D quantitative morphometric analyses and has allowed researchers and clinicians to observe disease progression and evaluate their treatments with higher precision and sensitivity than before [2]. In the context of quantitative analysis of musculoskeletal tissues, many morphometric measures have been developed for computed tomography (CT) [3]–[6] and magnetic resonance (MR) [7]–[10] images to evaluate tissue and structural changes of the bone and cartilage. Recent studies [11], [12] have proposed a suite of 17 quantitative morphometric analysis measures (QMA) describing structures of the joint to assess it as a single organ and have demonstrated its reproducibility and sensitivity in assessing joint health in preclinical small and medium animal models using *ex vivo* micro-computed tomography (microCT) datasets of intact rat and rabbit knee joints. The QMA consisted of traditional structural measures of the bone and cartilage, as well as novel 3D whole joint measures (joint QMA) that include an angle to quantify osteophytes presence and activity (σ), an angle to indicate erosion between lateral and femoral condyles (ρ), a vector defining altered angulation (λ, α, β, γ), measures of joint space width (JSW), and a slope and intercept (m, χ) of joint contact area under virtual loading.

As discussed in earlier works [11], [12], one of the main issues surrounding joint QMA is that it is highly sensitive to the correct alignment of the joint to a common position, as well as the appropriate subdivision of the joint into its medial and lateral components for separate joint QMA measurements of each side. The common orientation is defined as the position where the long axis of the tibia is aligned with the vertical z-axis while the rest of the joint is rigidly transformed accordingly to preserve the original relative pose of all joint components. Previously, this was achieved by manually aligning one joint sample as a reference. All other samples were then registered and transformed onto that reference using B-spline interpolation [13] to reduce rotational errors [14]. Selection of the volume of interest (VOI) of the joint's medial and lateral sides was subsequently done manually by an expert through visual inspection of the 3D images according to appropriate anatomical features.

However, the manual nature of the initial alignment process, as well as the selection of the medial and lateral joint VOI has meant the quality of the joint QMA measurements is highly dependent on the skills and training of the operators to achieve high reproducibility and disease discriminating quality. Moreover, the diversity of animal models involved in preclinical OA research introduces a variety of imaging resolutions [15]–[18]. Consequently, settings for image processing operations such as dilation, erosion, closing, opening, and others, in the workflow must also be manually adjusted to achieve a reliable result. This is a non-trivial task that prohibits the use of a simple adaptation between models [19], and is a time-consuming process that can occupy skilled operators for several weeks per study and present significant challenges to the robust application of joint QMA measurements in studies involving larger volumes of data and new joint models.

To tackle these challenges, this study presents an image processing pipeline that can automatically perform appropriate joint alignment and subdivision for efficient and high-quality 3D joint QMA while remaining robust across multiple small animal models. This study aims to estimate the shape and pose of the tibia and, by extension, the joint, based on a shape analysis technique called the spherical harmonic description method (SPHARM) [20], which employs spherical harmonic descriptors in distinction to the traditional registration-based approach. Medial and lateral subdivision of the VOI is implemented by locating the dividing point using a watershedding approach based on persistent homology [21], which is a topological data analysis method that identifies points with strong features. This study hypothesises that the pipeline will allow measurements of 3D joint QMA parameters with precision and reproducibility comparable to that of earlier studies that used manual alignment [11], [12], while achieving faster implementation and maintaining precision across species. Specifically, this study aims to compare measurement precision and reproducibility, as well as the overall processing time between the presented novel method and the manual processing approach on the same datasets which were published previously [11], [12].

5.4 Materials and methods

5.4.1 Animals and microCT scan protocols

Datasets were obtained from previous studies of intact *ex vivo* joints from rat [12] and rabbit [11]and are described in detail in the respective publications. The rat dataset consists of microCT scans (SCANCO Medical AG, Brüttisellen, Switzerland) of 21 tibio-femoral joints from 11 age-matched, Wistar rats. With a typical medial-lateral width of the tibia of 8.09 ± 0.62 mm, they were scanned with an isotropic nominal resolution of 10 µm. The rat dataset has an average image size in x, y, and z dimension of 1652.36 ± 221.39, 1416.59 ± 242, 943.5 ± 200.33 voxels and an average total number of voxels of $2.13x10^9 \pm 3.09x10^8$, respectively. The rabbit dataset consists of microCT scans of 6 tibio-femoral joints from 6 age-matched, New Zealand white rabbits. With a typical medial-lateral width of the tibia around 19.10 ± 0.59 mm, they were obtained with an isotropic voxel size of 18 µm, average image size in the x, y, and z dimension of 2017.00 ± 43.14, 2017.00 ± 43.14, 1891.83 ± 462.15 voxels and an average total number of voxels of $7.65x10^9 \pm 1.59x10^9$, respectively. During image acquisition of both datasets, initial joint positioning was controlled by placing a wedge (approx. 160° angle) behind the knee to control flexion-extension. The femoral condyles and the tibial plateau were included in the volume of interest, with the upper limit defined as the epiphyseal bone of the femur and the lower limit defined as the epiphyseal bone of the tibia (approx. 35-40 mm in rabbits and 12-15 mm in rats). Both datasets were filtered using a constrained 3D Gaussian filter (window, σ = 1.2, support, s = 1) after image reconstruction.

For each joint, four scans were performed. PRE scans were obtained by scanning joints without any contrast agent, while three repeat scans (labelled HEX1, HEX2, and HEX3) were obtained after a single intraarticular injection of SiO2-microbeads (0-20 µm diameter) (SWARCO Vestglass GmbH, Recklinghausen, Germany) to allow the visualisation of the cartilage. The three repeat scans were carried out to test for reproducibility with re-positioning between each scan.

5.4.2 Preprocessing pipeline for joint QMA

The developed image preprocessing pipeline consists of 2 main components: an alignment module and a subdivision module. Filtered and segmented 3D binarised images of the femur,

tibia, and their respective cartilage volumes are required inputs for the workflow. These images served as inputs for the alignment module. The resulting aligned, binarised images are used as inputs for the subdivision module which is the final module of the workflow. The images output from the pipeline are aligned and split into medial and lateral VOI and are ready for submission to the existing joint QMA analysis modules. An overview of the pipeline and the joint QMA measurements used to evaluate each process, are summarised in Figure 5-1.

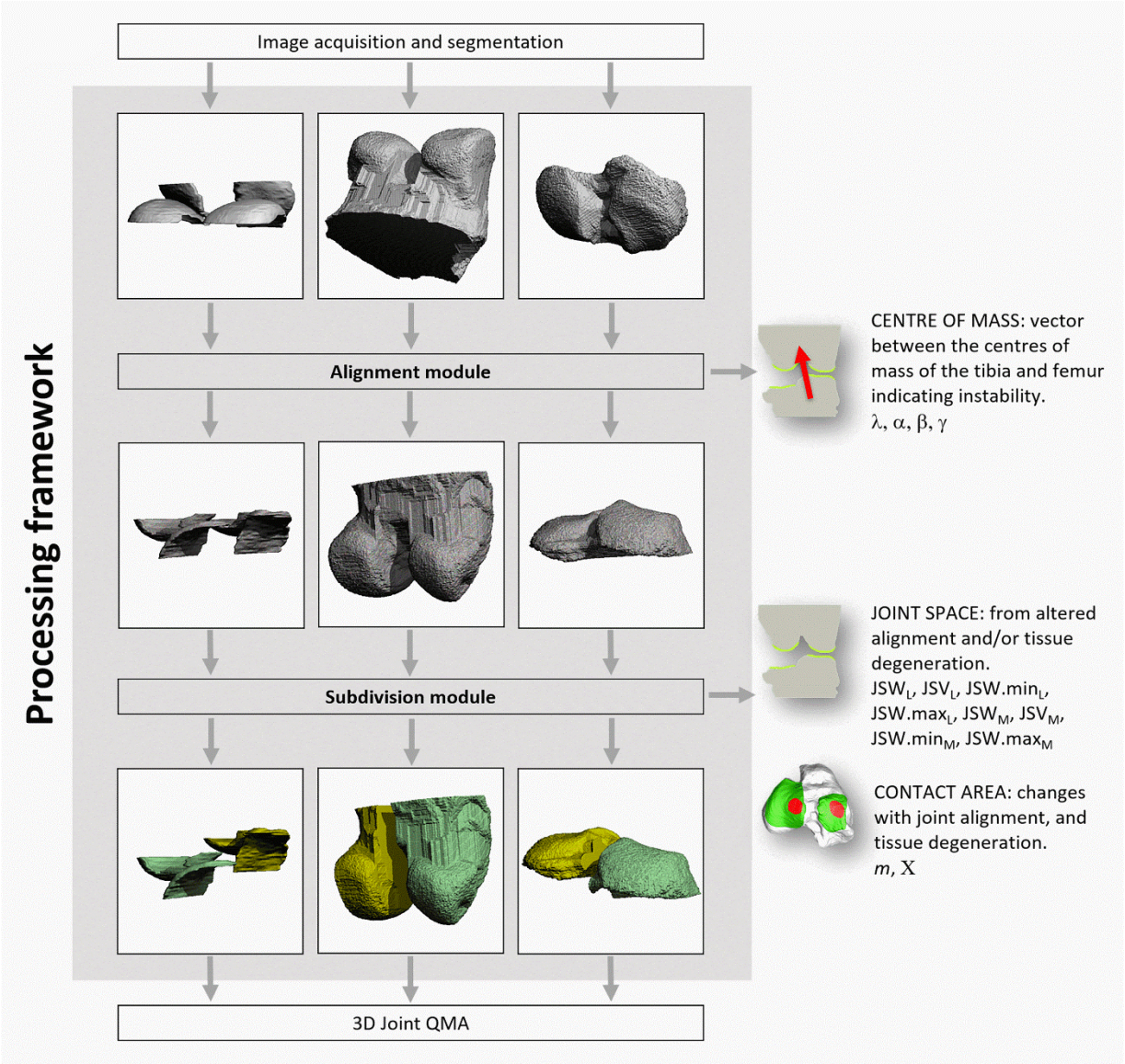

Figure 5-1: Overview of the pipeline as well as the relevant QMA used to evaluate each process. 3D microCT masks of cartilage (left column), femur (central column), and tibia (right column) of a typical rat knee is used to highlight each process's input and result. Each of the outputs of the subdivision module (bottom row) is split into medial (yellow) and lateral (green) volume of interests

5.4.2.1 Alignment module

Joint alignment method in this work estimated the tibia's elementary shape and pose using SPHARM [20]. In brief, SPHARM provides a hierarchical and multi-scale boundary description of objects with spherical topology. It computes an area-preserving mapping of the object's 3D voxel mesh onto a sphere in a separate parameter domain. The basis functions of the sphere are spherical harmonics, so that SPHARM describes the object as a set of basis function weights. By truncating the number of basis functions used in the description, different levels of object detail can be represented.

The mathematics of SPHARM and the parameterisation computation according to Brechbühler [22] employs Laplace's spherical basis functions, $Y_l^m(\theta, \varphi)$, characterised by degree, l and order, m, for $\theta \in [0, \pi]$ and $\varphi \in [0,2\pi]$, such that

$$Y_l^m(\theta, \varphi) = \sqrt{\frac{2l+1}{4\pi}\frac{(l-m)!}{(l+m)!}} P_l^m \cos\theta \, e^{im\varphi} \qquad \text{Equation 4-1}$$

$$Y_l^{-m}(\theta, \varphi) = (-1)^m Y_l^{m*}(\theta, \varphi) \qquad \text{Equation 4-2}$$

where $Y_l^{m*}(\theta, \varphi)$ denotes the complex conjugate of Y_l^m and P_l^m describes the associated Legendre polynomials. Some of the low order real spherical harmonics as derived from the above equation are visualised in Supplementary Figure 5-S1. This highlights the hierarchical representation of spherical objects where a higher spherical harmonics degree of l would lead to more complex forms of θ and φ and, thus, allows more details of the objects to be represented. Vice versa, by limiting the degree l to lower degree, the object detail would be reduced, up to the point where the object is represented by a sphere at $l = 0$.

To express the object's surface using the described spherical harmonics, the three coordinate functions are decomposed and the surface $\boldsymbol{V}(\theta, \varphi) = (x(\theta, \varphi), y(\theta, \varphi), z(\theta, \varphi))^T$ takes the form of:

$$\boldsymbol{V}(\theta, \varphi) = \sum_{l=0}^{\infty} \sum_{m=-l}^{l} \boldsymbol{c}_l^m \, Y_l^m(\theta, \varphi) \qquad \text{Equation 4-3}$$

where the coefficients $\boldsymbol{c}_l^m$ are 3D vectors of the three coordinates functions, obtained using a minimum squared error approach. Therefore, the values of the basis functions at each point in the discretised parameterised domain are gathered in the matrix, $z = \left(z_{i,j(l,m)}\right) = Y_l^m(\theta_i, \varphi_i)$ where $j(l, m)$ is a function assigning an index to every pair (l, m) and i denotes

the indices of n_{vert} points to be approximated. The coordinates of these points are arranged in the vector $\boldsymbol{v} = (\boldsymbol{V}_1, \boldsymbol{V}_2, \dots, \boldsymbol{V}_{n_{vert}})^T$ and all coefficients are gathered in the vector $\boldsymbol{c} = (\boldsymbol{c}_0^0, \boldsymbol{c}_1^{-1}, \boldsymbol{c}_1^0, \dots)^T$. The coefficients that best approximate the points from a least-square perspective are obtained by:

$$\boldsymbol{c} = (z^T z)^{-1} z^T \boldsymbol{v} \qquad \text{Equation 4-4}$$

Using spherical harmonic basis functions, a hierarchical surface description is obtained that includes further details as more basis functions are added according to degree l and order m (see Figure 5-2a and Figure 5-2b).

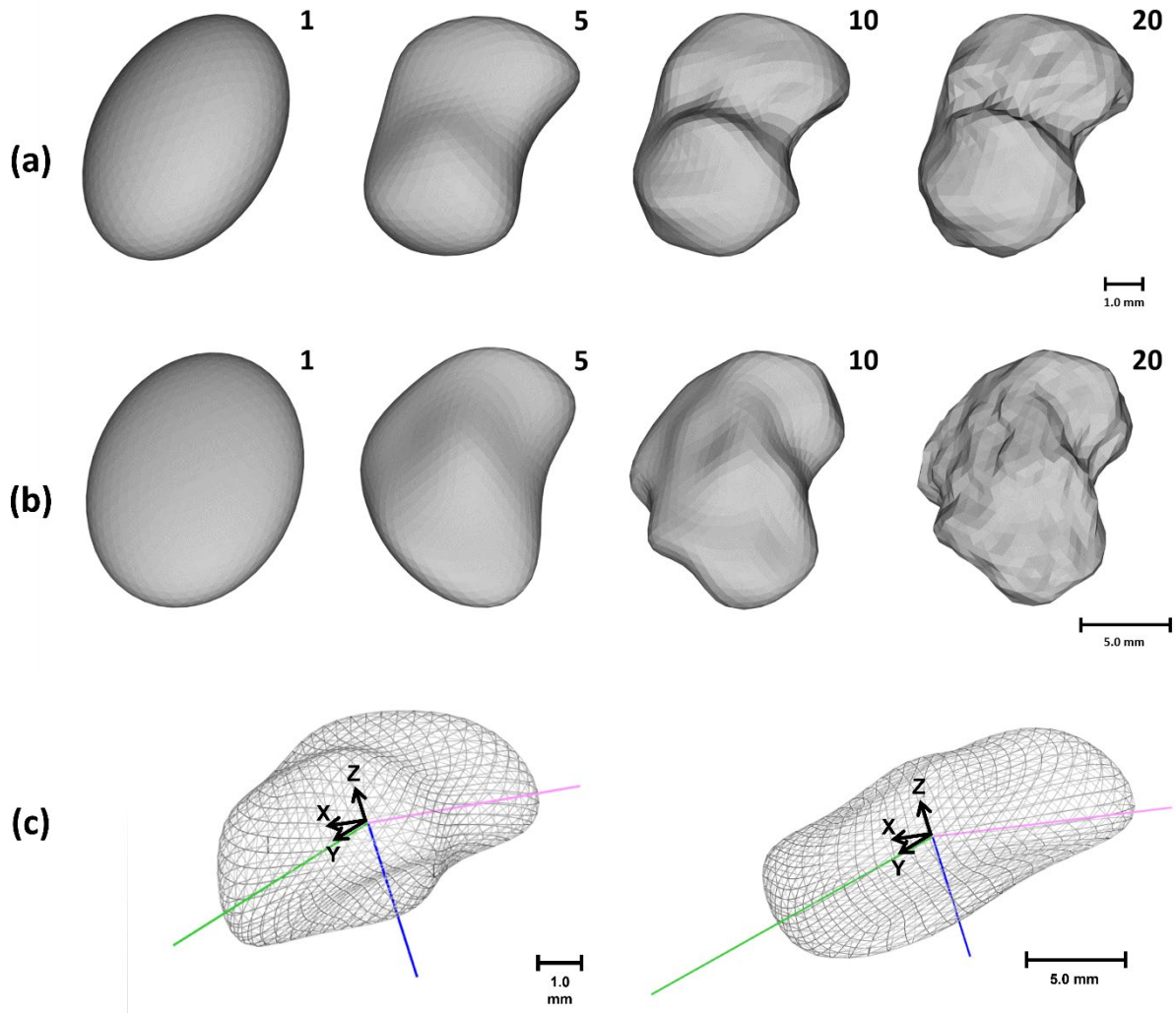

Figure 5-2: Isometric view of the SPHARM shape description of the proximal left tibial plateau of a typical rat (row a) and rabbit (row b) shown with different numbers of included basis functions of lowest degree (1, 5, 10, 20 harmonics, respectively). In row c, the shape of rat and rabbit tibia, represented by 5 harmonics and aligned towards a common orientation where the smallest principal component (blue) is aligned with the z-axis and the second smallest component (pink) is aligned with the x-axis are shown.

After obtaining the tibia's basic form from its truncated SPHARM description, principal component analysis (PCA) was performed. The smallest component of the tibia, which always aligns with its vertical axis, was used as the surrogate for the tibial vertical orientation, while the horizontal orientation was controlled by the second-smallest component. Subsequently, a series of transformation matrices aligning the smallest component with the z-axis and the second-smallest component with the x-axis was calculated, as seen in Figure 5-2c, and was used to transform the full joint image using a B-spline interpolation method as the subsequent joint alignment step.

5.4.2.2 Subdivision module

Images aligned in the previous module were further processed through the subdivision module to divide the image of the joint into its medial and lateral VOI. The module operates by performing a watershedding operation based on persistence homology to identify the local minimum between the intercondylar tubercles of the tibia's intercondylar eminence, as indicated in Figure 5-3a and Figure 5-3b, and using that location as the dividing point for defining the tibia, and subsequently the joint, medial and lateral side. The module achieves this by analysing a series of projections created from the aligned microCT dataset and taking advantage of the controlled alignment achieved in the previous module, where the axial and coronal planes are aligned with the z- and x-axis, respectively.

The subdivision module created a 2-dimensional (2D) topographic map of the tibial plateau's features by projecting along the coronal plane as seen in Figure 5-3c. Subsequently, the map was used to create a 1-dimensional (1D) projection on the coronal plane as illustrated by the blue profile in Figure 5-3d. To further limit the impact of osteophytes on the dividing point detection algorithm, the 1D projection was cropped to exclude values not in the centre of the object which is the area where the intercondylar tubercle is located.

From the processed 1D projection map, the dividing point was located using persistence homology, which is an algebraic method for capturing topological features like local extrema [23], [24], computed using the **persistence1d** [25] algorithm. In brief, the algorithm detects persistence homology from a 1D signal, which corresponds to all pairs of its local minima and maxima. Using this method, the global maxima is always paired with the background and has the highest persistence. The module's watershedding approach removes all persistence pairs except the second-largest one, whose maxima corresponds to the minimum point between

intercondylar eminences; and thus, defined as the watershed point used to divide and select the sub-images.

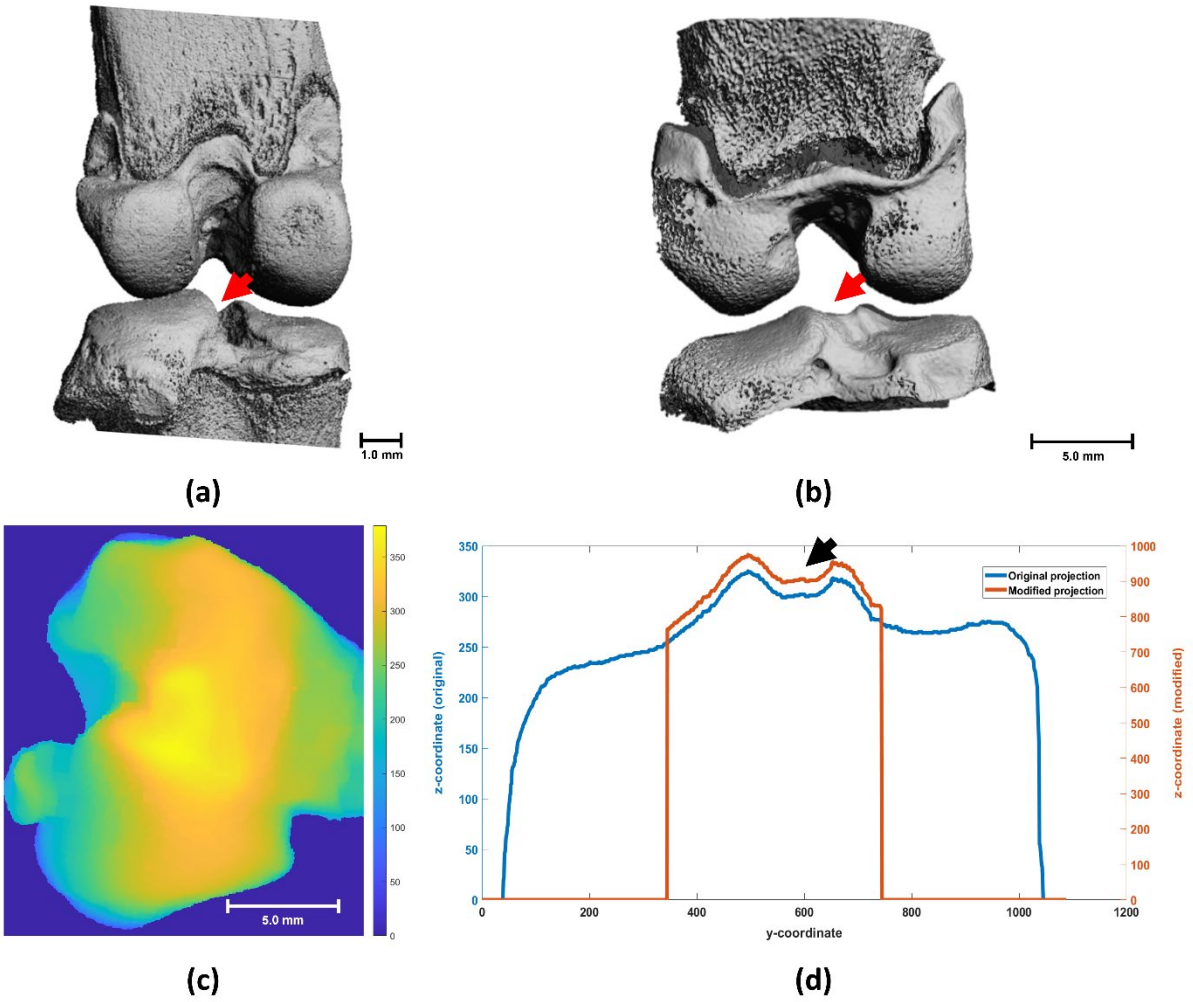

Figure 5-3: (a) Rat and (b) rabbit tibial intercondylar eminence used as the dividing point (red arrows) of the subdivision module. (c) Topographic map of the projections from a rabbit tibial plateau with values representing z-coordinates. (d) Subsequent 1D projection demonstrating the height profile of the tibia (blue line) as well as the cropped and boosted profile (orange line) used in actual computation of the point (black arrow).

5.4.3 3D joint QMA, reproducibility, and accuracy

The joint centre of mass, defined as a vector with orientation (α, degree; β, degree; and γ, degree) measured along the three principle Cartesian axes, and connecting the centres of mass of the two bones, was used to measure the relative position of the joint to evaluate the performance of the alignment module [11]. To assess the subdivision module, as well as the pipeline as a whole, several 3D joint metrics were measured from the resulting medial (M) and lateral (L) sub-images of the joint. Joint contact area under virtual loading was also measured. This was done by incrementally shifting the tibia onto the femur along the vertical z-axis. The contact area is, then, defined as the distance travelled to first contact ($\chi_{L/M}$, μm)

and the rate at which contact area increases ($m_{L/M}$, $\frac{mm^2}{step}$) [11]. Alongside these metrics, 3D measurements of the joint space width (JSW): joint space volume ($JSV_{L/M}$, mm^3), JSW ($JSW_{L/M}$, mm), minimum JSW ($JSW_{L/M}.min$, mm), and maximum JSW ($JSW_{L/M}.max$, mm) were also measured [12], [26].

Reproducibility of the measured 3D QMA was tested using RStudio (RStudio: Integrated development environment for R, Version 0.95.258, Boston, MA, USA). Precision error (PE(SD)) and precision error expressed as coefficients of variation (PE(%CV)), as well as an intraclass correlation coefficient (two-way random effects, consistency, multiple measurements ICC [27]) with 95% confidence interval (CI), were calculated to test the absolute agreement between each measurement [28]. ICC values range from 0 to 1, with those close to 1 indicating high similarity between measurements from the same group. Reproducibility of measurements is classified as excellent when ICC values are higher than 0.75 [29]. Good, fair, and poor reproducibility is classified when ICC values range from 0.6 to 0.74, 0.40 to 0.59, and 0 to 0.4, respectively [29].

Reproducibility results were compared with reproducibility values obtained in previous studies [11], [12] using the same dataset but has performed the tasks in this workflow manually. Additionally, to measure accuracy, the joint QMA results obtained in this study were compared with results from earlier studies [11], [12]. Measurement differences were evaluated as root-mean-squared error expressed in both absolute (RMSE) and mean-normalised (NRMSE) form by using the original results as reference.

5.4.4 Pipeline implementation and performance

The pipeline was implemented in two separate parts. SPHARM processing (statistical shape analysis module [30] on 3DSlicer [31]), alignment determination, and dividing point location were done on Windows 10 running on Intel i7-10875H processor (8 cores, 16MB cache, 2.30 GHz to 5.10 GHz) with Nvidia Quadro P620 GPU and 16GB RAM, while the subsequent joint alignment and subdivision were done on networked OpenVMS V8.4 I64 running on HP Integrity rx2800 i2 platform (8 Intel Itanium CPUs, 1.6 GHz, 5 MB cache) with 32 GB of allocated RAM. The source code is available from the corresponding author upon request.

Pipeline performance was recorded as the average CPU time (in seconds) required to perform each process. Processing time was measured to enable benchmarking against manual processing time in earlier studies (in hours) on the same dataset [11], [12] whose estimates were obtained through examination of processing logs. Additionally, to benchmark the alignment module against another solution, the automatic joint alignment module was applied to the original images, without using SPHARM as part of the process.

5.5 Results

To select the optimal SPHARM degree for the workflow, a parametric study where the ICCs of the resulting joint centre of mass were evaluated for an increasing number of harmonics. The results are available in Table 5-S5 of the supplementary section which shows that a SPHARM degree of 5 yielded the highest ICC result and was used for all the subsequent results in this manuscript.

5.5.1 Alignment module

For rat data, SPHARM-based module yielded excellent ICCs for all orientation measures (α: 0.955, β: 0.958, γ: 0.951) (Table 5-1) while alignment using full rat image yielded only good and fair ICCs for orientation measures (α: 0.508, β: 0.732, γ: 0.663) (Table 5-1). In contrast, alignment using full rabbit image yielded excellent and good ICCs (α: 0.965, β: 0.757, γ: 0.927) (Table 5-1), which were maintained or improved using SPHARM-based approach (α: 0.936, β: 0.920, γ: 0.934) (Table 5-1). For all centre of mass measurements in both models, minimal precision errors are reported with PE(%CV) lower than 2% for all values.

5.5.2 Subdivision module

Excellent reproducibility was achieved for the contact area QMA measured from both rat and rabbit samples. Results for rat data showed slightly lower ICC for χ of both medial and lateral side (χ_L: 0.871, χ_M: 0.875) compared to ICC for both m (m_L: 0.972, m_M: 0.982) (Table 5-2). For rabbit data, all except m_M with ICC of 0.841, has ICC of more than 0.9 (Table 5-2). For all contact area measurements of both models, small precision errors are reported with PE(%CV) lower than 10% for all value.

Table 5-1: Reproducibility of the rat and rabbit joint centre of mass in terms of intraclass correlation coefficient (ICC) and precision errors (PE) expressed in absolute and a percentage of the coefficient of variation of the repeated measure. (α: angle with respect to x-axis, β: angle with respect to y-axis, γ: angle with respect to z-axis)

Rat (10 µm voxel size, 21 tibio-femoral joint samples, 4 repeated scans each)															
	Manually aligned [12] using full image					Automatically aligned using full image					Automatically aligned using SPHARM descriptors				
	ICC	Lower 95%	Upper 95%	PE (SD)	PE (%CV)	ICC	Lower 95%	Upper 95%	PE (SD)	PE (%CV)	ICC	Lower 95%	Upper 95%	PE (SD)	PE (%CV)
α (°)	0.990	0.971	0.997	1.04	1.07%	0.508	0.207	0.800	21.90	34.96%	0.955	0.891	0.986	1.90	1.80%
β (°)	0.981	0.945	0.995	0.50	0.51%	0.732	0.483	0.906	4.54	5.21%	0.958	0.899	0.987	1.45	1.62%
γ (°)	0.998	0.995	0.999	0.35	0.47%	0.663	0.387	0.876	11.38	8.16%	0.951	0.884	0.985	1.67	1.06%

Rabbit (18 µm voxel size, 6 tibio-femoral joint samples, 4 repeated scans each)															
	Manually aligned [11] using full image					Automatically aligned using full image					Automatically aligned using SPHARM descriptors				
	ICC	Lower 95%	Upper 95%	PE (SD)	PE (%CV)	ICC	Lower 95%	Upper 95%	PE (SD)	PE (%CV)	ICC	Lower 95%	Upper 95%	PE (SD)	PE (%CV)
α (°)	0.978	0.915	0.996	1.80	1.77%	0.965	0.884	0.994	4.95	9.24%	0.936	0.796	0.990	1.87	1.96%
β (°)	0.913	0.681	0.984	1.16	1.20%	0.757	0.408	0.955	5.55	6.22%	0.920	0.753	0.987	1.63	1.82%
γ (°)	0.981	0.931	0.996	1.46	0.92%	0.927	0.772	0.988	5.23	3.35%	0.934	0.790	0.989	1.29	0.76%

Table 5-2: Reproducibility of the rat and rabbit joint contact area under virtual loading in terms of intraclass correlation coefficient (ICC) and precision errors (PE) expressed in absolute and a percentage of the coefficient of variation of the repeated measure. (χ: distance travelled to first contact, m: rate at which contact area increases)

Rat (10 µm voxel size, 21 tibio-femoral joint samples, 4 repeated scans each)											
		Manually subdivided [12]					Automatically subdivided				
		ICC	Lower 95%	Upper 95%	PE (SD)	PE (%CV)	ICC	Lower 95%	Upper 95%	PE (SD)	PE (%CV)
χ (mm)	Lateral	0.957	0.877	0.988	0.01	4.27%	0.871	0.689	0.960	0.01	3.10%
	Medial	0.925	0.777	0.980	0.01	5.57%	0.875	0.698	0.961	0.01	2.80%
m (mm²/mm)	Lateral	0.966	0.902	0.991	1.04	3.00%	0.972	0.924	0.992	2.87	2.84%
	Medial	0.992	0.976	0.998	0.42	1.30%	0.982	0.950	0.995	6.98	5.75%

Rabbit (18 µm voxel size, 6 tibio-femoral joint samples, 4 repeated scans each)											
		Manually subdivided [11]					Automatically subdivided				
		ICC	Lower 95%	Upper 95%	PE (SD)	PE (%CV)	ICC	Lower 95%	Upper 95%	PE (SD)	PE (%CV)
χ (mm)	Lateral	0.888	0.547	0.979	0.04	9.58%	0.952	0.815	0.993	0.01	4.39%
	Medial	0.754	0.202	0.951	0.03	8.72%	0.951	0.811	0.992	0.01	4.46%
m (mm²/mm)	Lateral	0.980	0.928	0.996	1.11	5.26%	0.906	0.669	0.985	5.60	3.64%
	Medial	0.903	0.642	0.982	0.95	4.18%	0.841	0.498	0.974	13.44	6.51%

For rat data, excellent reproducibility in was achieved for all joint space measurements, except $JSW.max$ where the reproducibility is very low ($JSW.max_L$: 0.384, $JSW.max_M$: 0.536). Among the rest, ICCs for $JSW.min$ are slightly lower ($JSW.min_L$: 0.859, $JSW.min_M$: 0.874) than others which have ICCs of more than 0.9, as shown in Table 5-3. Similarly, as seen in Table 5-4, excellent ICCs were also achieved for rabbit joint space measurements with values ranging from 0.780 (for $JSW.min_M$) to 0.955 (for JSV_L) except for $JSW.max_L$, which have an ICC of 0.608. Small precision error is also reported for both models, with PE(%CV) lower than 6.5% for all values except rabbit $JSW.min_M$ with PE(%CV) of 15.11%.

Table 5-3: Reproducibility of the rat and rabbit joint space measurements in terms of intraclass correlation coefficient (ICC) and precision errors (PE) expressed in absolute and a percentage of the coefficient of variation of the repeated measure. (JSW: mean joint space width, JSV: joint space volume, JSW.min: minimum joint space width, JSW.max: maximum joint space width)

Rat (10 µm voxel size, 21 tibio-femoral joint samples, 4 repeated scans each)											
		Manually subdivided [12]					Automatically subdivided				
		ICC	Lower 95%	Upper 95%	PE (SD)	PE (%CV)	ICC	Lower 95%	Upper 95%	PE (SD)	PE (%CV)
JSW (µm)	Lateral	0.986	0.960	0.996	0.02	3.34%	0.946	0.871	0.983	0.01	0.86%
	Medial	0.968	0.906	0.991	0.01	2.23%	0.943	0.866	0.982	0.01	2.26%
JSV (mm³)	Lateral	0.986	0.962	0.996	0.05	2.58%	0.952	0.886	0.985	0.04	2.41%
	Medial	0.983	0.955	0.995	0.03	1.79%	0.905	0.785	0.970	0.09	5.44%
JSW.min (µm)	Lateral	0.859	0.623	0.958	0.04	18.73%	0.911	0.789	0.972	0.01	5.15%
	Medial	0.874	0.663	0.963	0.03	24.70%	0.924	0.824	0.976	0.02	6.41%
JSW.max (µm)	Lateral	-0.030	-0.230	0.353	0.01	0.59%	0.384	0.089	0.725	0.02	2.15%
	Medial	0.763	0.378	0.929	0.01	1.00%	0.536	0.236	0.815	0.01	1.11%

Rabbit (18 µm voxel size, 6 tibio-femoral joint samples, 4 repeated scans each)											
		Manually subdivided [11]					Automatically subdivided				
		ICC	Lower 95%	Upper 95%	PE (SD)	PE (%CV)	ICC	Lower 95%	Upper 95%	PE (SD)	PE (%CV)
JSW (µm)	Lateral						0.907	0.719	0.985	0.05	2.61%
	Medial						0.941	0.811	0.991	0.04	2.20%
JSV (mm³)	Lateral						0.955	0.853	0.993	0.01	3.96%
	Medial	3D JSW was not performed in earlier study for					0.907	0.717	0.985	0.01	4.17%
JSW.min (µm)	Lateral	this dataset.					0.916	0.742	0.986	0.05	5.86%
	Medial						0.780	0.447	0.960	0.13	15.11%
JSW.max (µm)	Lateral						0.608	0.202	0.919	0.09	2.36%
	Medial						0.790	0.466	0.962	0.16	4.44%

Table 5-4: 3D joint QMA results for rat and rabbit datasets obtained in previous studies through manual processing, and in this study using the proposed automatic workflow. Accuracy of the automatically processed rat and rabbit measurements are shown in terms of root-mean-squared error expressed in absolute (RMSE) and mean-normalised (NRMSE) form. (JSW: mean joint space width, JSV: joint space volume, JSW.min: minimum joint space width, JSW.max: maximum joint space width, α: angle with respect to x-axis, β: angle with respect to y-axis, γ: angle with respect to z-axis, χ: distance travelled to first contact, m: rate at which contact area increases)

Rat (10 µm voxel size, 21 tibio-femoral joint samples, 4 repeated scans each)							
		Manually processed [12]		Automatically processed			
		Mean	± SD	Mean	± SD	RMSE	NRMSE
JSW (µm)	Lateral	578.0	33.0	534.6	19.3	49.7	8.53%
	Medial	683.7	66.5	629.4	54.2	60.1	8.88%
JSV (mm^3)	Lateral	1.40	0.16	1.40	0.15	0.05	3.27%
	Medial	1.76	0.26	1.76	0.28	0.05	2.86%
JSW.min (µm)	Lateral	246.8	40.8	224.5	40.3	23.5	9.50%
	Medial	382.7	74.7	362.7	74.5	21.3	5.63%
JSW.max (µm)	Lateral	996.6	27.3	975.7	26.7	22.4	2.24%
	Medial	1045.0	17.0	1026.6	15.2	20.2	1.93%
α (°)		94.3	11.0	97.6	8.8	8.0	8.39%
β (°)		85.9	2.5	87.6	7.0	6.6	7.69%
γ (°)		167.2	4.2	168.5	7.5	6.6	4.00%
χ (mm)	Lateral	0.25	0.02	0.27	0.02	0.02	7.10%
	Medial	0.26	0.02	0.28	0.02	0.02	7.92%
m (mm^2/mm)	Lateral	91.1	15.9	96.6	16.5	6.3	6.81%
	Medial	115.9	43.8	124.9	46.9	10.0	8.69%

Rabbit (18 µm voxel size, 6 tibio-femoral joint samples, 4 repeated scans each)							
		Manually processed [11]		Automatically processed			
		Mean	± SD	Mean	± SD	RMSE	NRMSE
JSW (µm)	Lateral	3D JSW was not performed in earlier study for this dataset.		1889.1	147.6	3D JSW was not performed in earlier study for this dataset.	
	Medial			1953.3	172.7		
JSV (mm^3)	Lateral			39.62	6.92		
	Medial			45.32	5.57		
JSW.min (µm)	Lateral			806.8	171.6		
	Medial			872.1	224.6		
JSW.max (µm)	Lateral			3742.8	121.4		
	Medial			3616.0	294.2		
α (°)		89.0	6.5	94.1	7.0	7.0	7.78%
β (°)		90.4	1.8	89.2	5.1	6.5	7.33%
γ (°)		171.1	3.4	171.9	4.9	6.5	3.81%
χ (mm)	Lateral	0.48	0.08	0.52	0.08	0.04	7.93%
	Medial	0.50	0.08	0.54	0.09	0.04	8.18%
m (mm^2/mm)	Lateral	51.2	6.4	55.1	6.9	4.3	8.31%
	Medial	77.7	8.4	83.3	10.0	6.5	8.43%

5.5.3 3D joint QMA result and accuracy

For both datasets, all 3D joint QMA measurements have differences from the manual measures of less than 9.5% (Table 5-4). For rabbit data, 3D joint space measurements were not performed, so that accuracy results are available only for the rat dataset which have differences from the manual measures of less than 9.5% (Table 5-4). JSV and JSW.max have particularly low differences; less than 3.5% and less than 2.5%, respectively (Table 5-4).

5.5.4 Pipeline performance

As seen in Table 5-5, the average time the pipeline used to finish processing a sample is shorter (rat: 693 s, rabbit: 2,112 s) than manual processing done on the same datasets in previous rat and rabbit studies (7,200 s for initial alignment and an additional 2,700 s for each rat sample and an additional 5,400 s for each rabbit sample). It is noted that a relatively high standard deviation was observed (rat: 212 s, rabbit: 276 s) due to networked connections. The most time-consuming process of the pipeline was the subsequent joint alignment using B-spline interpolation (rat: 248 ± 69 s, rabbit: 883 ± 261 s) and SPHARM processing (rat: 184 ± 77 s, rabbit: 1,019 ± 61 s) while the subdivision location was the fastest (rat: 19 ± 10 s, rabbit: 10 ± 3 s).

Table 5-5: CPU time for each process of the pipeline expressed in mean (± SD) seconds. Total time for manual processing performed in earlier studies is shown on the last column for comparison.

	Alignment module						Subdivision module				Framework		Manual processing from earlier studies [11-12]	
	SPHARM processing time (s)		Alignment determination time (s)		Subsequent joint alignment time (s)		Subdivision point location time (s)		Subsequent joint subdivision time (s)		Total processing time (s)		Total processing time (s)	
	mean	± SD	mean	± SD	mean	± SD	mean	± SD	mean	± SD	mean	± SD	mean	± SD
Rat	184	77	27	4	248	69	19	10	215	100	693	212	9,900	1,100
Rabbit	1,019	61	27	15	883	261	10	3	172	64	2,112	276	12,600	1,300

5.6 Discussions

In this study, an image processing pipeline, that automatically prepares 3D joints images for sensitive and reproducible joint QMA measurements, does not require adaptation between animal models and is computationally efficient, was developed. Using SPHARM spherical harmonics modelling, the pipeline describes the tibia's basic form and determines the transformation needed to align the joint. The second module subdivides the joint into medial and lateral compartments by locating the tibia's intercondylar eminence as the watershed point using persistence homology to divide the VOI. The novelty of this work lies in the development of a new image processing pipeline that has been proven to prepare images efficiently and automatically for high-quality QMA, while remaining robust across two different preclinical animal models. This allows researchers to effectively perform 3D joint QMA in studies involving a larger number of samples, such as in longitudinal studies, with less expertise and a reduced time requirements compared to manual processing. Coupled with its robustness across rat and rabbit species, two common preclinical models for OA research [32], the pipeline has the potential to make 3D joint QMA a more accessible technique.

The alignment and subdivision pipeline, used in conjunction with 3D joint QMA, could be applied to studies involving other musculoskeletal diseases beyond OA to reveal previously unknown quantitative changes to the joint. Moreover, although the proposed pipeline was developed and validated on microCT data, it should be noted that the workflow starts after segmentation. Consequently, if the segmented components of a joint are available with appropriate resolution (i.e., two segmented bone images for the joint centre of mass and joint space width measurements, and additional cartilage images for contact area under virtual loading), the framework could be applied to calculate 3D joint QMA for other imaging modalities (such as magnetic resonance imaging or CT), in addition to other joint sites.

The pipeline also utilises SPHARM in a novel application. From its original proposal [20], SPHARM has been widely used in statistical shape modelling for analysis of many organs, while others have found applications in using SPHARM descriptors for efficient image rotation estimation to take advantage of its hierarchical representation property [33], [34]. However, few works have taken advantage of SPHARM's ability to represent objects in hierarchical levels of details in the object space for image processing purposes. The approach used in this work eliminated complex computation needed to perform image registration with $O(n^2)$

complexity [35] and focused instead on finding a single solution that aligned the principal components to the desired pose with $O(n)$ complexity. This performance improvement can be highlighted in Table 5-5, where the average time needed to calculate the transformation matrix for both rat and rabbit dataset were approximately 27 seconds, while the B-spline image transformation performed in the subsequent joint alignment step took much longer to complete.

Moreover, the pipeline's use of an efficient algorithm for subdivision - locating persistence homology pairs by Kozlov and Weinkauf [25], which has $O(n \log n)$ complexity - allows for highly efficient processing overall. On average, the pipeline finished processing each sample in 693 seconds for rat and 2,112 seconds for rabbit, which is a great reduction from the 2,700 seconds for each rat and 5,400 seconds for each rabbit needed in earlier studies [11], [12] with most of the reduction coming from automation of the alignment. As shown in Table 5-5, the major difference in processing time between both animals can be traced back to the SPHARM modelling and subsequent joint alignment processes, where the average time needed for a rabbit sample is significantly higher than that of a rat. This is likely due to the differences in animal size and imaging scale (imaged volume and resolution) as described in the imaging protocol and resulted in rabbit images containing significantly more voxels than rat images (5.52×10^9 more voxels on average). Therefore, more time was needed to perform SPHARM modelling and transformation. Other processes did not rely on the resolution of the images and resulted in similar processing times across animal models.

With regards to the quality of the QMA measurements, the pipeline is able to produce QMA measurement results with excellent reproducibility (ICC > 0.75) and precision errors (< 2% PE(%CV)) for the centre of mass and < 10% PE(%CV) for contact area but have comparable or slightly lower ICC compared to the gold-standard of manual processing by experts. As seen in Table 5-1, reproducibility values for the joint centre of mass from the pipeline are, generally, very slightly lower than that obtained from manually processed images from previous studies [11], [12]. Reproducibility of contact area measurements, however, showed a mix of superior and inferior values when comparing with previous works. In general, manual processing in the earlier rat study [12] produced slightly better ICC than those from the pipeline, while manual processing in the earlier rabbit study [11] showed more mixed results as seen in Table 5-2. This could point to the increased experience of the operators in the follow-up study in

the rat model [12] as compared to the pioneering 3D joint QMA study of the rabbit model [11].

It should be noted that the joint space measurements performed in the rat study [12] and the rabbit study [11] were not the same JSW modules. In the original QMA work [11], JSW was measured as the distance of the joint space between the centre of the femoral condyle and the tibia; while, in the later work [12], the JSW was directly measured in 3D using the SPECTRA consensus approach [26] with JSV also being evaluated. In this study, the SPECTRA consensus approach was used to calculate JSW and JSV on both rat and rabbit dataset. As with the centre of mass and contact area measurements, reproducibility of the rat JSW and JSV showed excellent (ICC > 0.9), though slightly lower, values compared to results obtained with manual preprocessing. However, the pipeline results for $JSW.min_{M/L}$ have significantly lower precision error PE(%CV) as seen in Table 5-3. For rabbit data, this study also presents novel 3D JSW and JSV measurements with corresponding reproducibility values in Table 5-3 which shows excellent reproducibility for all joint space measures, except $JSW.max_L$ with ICC of 0.608. This generally high-quality result for previously unperformed joint space QMA for the rabbit dataset highlights the pipeline's ability to correctly subdivide the images into the appropriate VOI and can support new QMA parameters in the future. With regards to low reproducibility of $JSW.max$, this study's result affirms earlier study's recommendation [12] not to use in further analysis for rat knee. Moreover, the lower ICC for $JSW.max_L$ in rabbit sample also lead this study to recommend $JSW.max$ not be used for further analysis in rabbit knee as well.

The 3D joint QMA values measured using the proposed automatic workflow were shown to have similar values to those from earlier studies in Table 5-4. For both datasets, all measurements have NRMSE errors of up to 9.5%. This highlights the sensitivity of 3D joint QMA to the differences in alignment results, despite using the same image datasets. However, it should be further noted that there are no standard values of acceptable precision (PE(SD) and PE(%CV) and accuracy (RMSE and NRMSE) as they are highly dependent on the measurement context. Values of error for these measurements should be considered acceptable when the measurement approach provides results which are sensitive to the effects of disease or treatment, while maintaining consistent reproducibility values. With comparable reproducibility and precision errors, joint QMA results from previous rat (Table

5-S8, [12]) and rabbit (Table 5-S9, [11]) studies were shown to be sensitive to OA, pointing to an acceptable range of precision errors obtained in this study.

Since SPHARM modelling was used as the basis for its alignment algorithm, one of the essential requirements is that the input tibia must be spherical in nature. This presents one of the main limitations of the pipeline as any samples such as those bone with convex surfaces at the edge of the image due to the VOI cropping through the medullary canal will not meet this requirement and will fail during the SPHARM processing step. Some manual closing, and smoothing operations will have to be performed on these samples prior to being processed through the pipeline.

Additionally, even though the pipeline has solved the issue of joint alignment in the image processing stage, it is clear that systematic positioning of the joint during the acquisition of the images is fundamental to ensure that all joints are captured in a similar pose. In joint imaging where multiple rigid structures are of interest, it is not possible to simultaneously align both the femur and tibia without altering their original relative position which provides important pathological information [36]. Similar challenges have been noted in clinical measurement of radiological JSW, where reproducible patient position is required for reliable tracking of joint changes [37], [38]. Future improvements in this direction would be in the form of a standardised positioning for acquisition that would allow the joints to be scanned and rescanned with minimal difference in pose between each. Further investigation, in strict quantitative terms, the definition of a gold standard alignment from which joint QMA can be precisely measured should also be done. Together, it is expected that even higher measurement reproducibility could be achieved.

Moreover, further *in vivo* experiments with regards to sensitivity and reproducibility of the proposed workflow and the novel 3D joint QMA parameters is required to determine whether these *ex vivo* results can be replicated *in vivo*. Movement artifact in live animal may reduce the precision and accuracy of these measurements, requiring further development of the workflow.

5.7 Conclusion

In previous work, quantitative measurements of joint morphometry using QMA has shown potential as a platform to quantify disease-based morphometric features for joint research

using multiple preclinical animal models. However, its accessibility and usage are limited by high sensitivity to alignment and joint subdivision which are technically challenging and time-consuming to implement manually. In this work, we developed an automatic, efficient, and model-invariant image processing pipeline. The software was found to allow 3D joint QMA measurements with excellent reproducibility comparable to those obtained from manual processing in earlier studies.

5.8 Acknowledgement

This work was supported by the Discovery Projects scheme of the Australian Research Council (DP180101838).

References

[1] G. Dougherty, Ed., *Medical Image Processing: Techniques and Applications*. New York, NY: Springer New York, 2011.

[2] I. Scholl, T. Aach, T. M. Deserno, and T. Kuhlen, "Challenges of medical image processing," *Comput. Sci. - Res. Dev.*, vol. 26, no. 1–2, pp. 5–13, Feb. 2011, doi: 10.1007/s00450-010-0146-9.

[3] T. Hildebrand and P. Rüegsegger, "A new method for the model-independent assessment of thickness in three-dimensional images," *J. Microsc.*, vol. 185, no. 1, pp. 67–75, Jan. 1997, doi: 10.1046/j.1365-2818.1997.1340694.x.

[4] T. Hildebrand, A. Laib, R. Müller, J. Dequeker, and P. Rüegsegger, "Direct Three-Dimensional Morphometric Analysis of Human Cancellous Bone: Microstructural Data from Spine, Femur, Iliac Crest, and Calcaneus," *J. Bone Miner. Res.*, vol. 14, no. 7, pp. 1167–1174, Jul. 1999, doi: 10.1359/jbmr.1999.14.7.1167.

[5] A. Odgaard and H. J. G. Gundersen, "Quantification of connectivity in cancellous bone, with special emphasis on 3-D reconstructions," *Bone*, vol. 14, no. 2, pp. 173–182, Mar. 1993, doi: 10.1016/8756-3282(93)90245-6.

[6] A. Odgaard, E. B. Jensen, and H. J. G. Gundersen, "Estimation of structural anisotropy based on volume orientation. A new concept," *J. Microsc.*, vol. 157, no. 2, pp. 149–162, Feb. 1990, doi: 10.1111/j.1365-2818.1990.tb02955.x.

[7] F. Eckstein, D. Burstein, and T. M. Link, “Quantitative MRI of cartilage and bone: degenerative changes in osteoarthritis,” *NMR Biomed.*, vol. 19, no. 7, pp. 822–854, Nov. 2006, doi: 10.1002/nbm.1063.

[8] W. Wirth and F. Eckstein, “A technique for regional analysis of femorotibial cartilage thickness based on quantitative magnetic resonance imaging,” *IEEE Trans. Med. Imaging*, vol. 27, no. 6, pp. 737–744, Jun. 2008, doi: 10.1109/TMI.2007.907323.

[9] J. Hohe, G. Ateshian, M. Reiser, K.-H. Englmeier, and F. Eckstein, “Surface size, curvature analysis, and assessment of knee joint incongruity with MRI in vivo,” *Magn. Reson. Med.*, vol. 47, no. 3, pp. 554–561, Mar. 2002, doi: 10.1002/mrm.10097.

[10] T. Stammberger, F. Eckstein, K. Englmeier, and M. Reiser, “Determination of 3D cartilage thickness data from MR imaging: Computational method and reproducibility in the living,” *Magn. Reson. Med.*, vol. 41, no. 3, pp. 529–536, Mar. 1999, doi: 10.1002/(SICI)1522-2594(199903)41:3<529::AID-MRM15>3.0.CO;2-Z.

[11] K. S. Stok *et al.*, “Three-Dimensional Quantitative Morphometric Analysis (QMA) for In Situ Joint and Tissue Assessment of Osteoarthritis in a Preclinical Rabbit Disease Model,” *PLoS One*, vol. 11, no. 1, p. e0147564, Jan. 2016, doi: 10.1371/journal.pone.0147564.

[12] B. A. Besler *et al.*, “Quantitative measures of bone shape, cartilage morphometry and joint alignment are associated with disease in an ACLT and MMx rat model of osteoarthritis,” *Bone*, vol. 146, p. 115903, Feb. 2021, doi: 10.1016/j.bone.2021.115903.

[13] P. Thévenaz, T. Blu, and M. Unser, “Interpolation revisited,” *IEEE Trans. Med. Imaging*, vol. 19, no. 7, pp. 739–758, Jul. 2000, doi: 10.1109/42.875199.

[14] F. A. Schulte, F. M. Lambers, T. L. Mueller, M. Stauber, and R. Müller, “Image interpolation allows accurate quantitative bone morphometry in registered micro-computed tomography scans,” *Comput. Methods Biomech. Biomed. Engin.*, vol. 17, no. 5, pp. 539–548, Apr. 2014, doi: 10.1080/10255842.2012.699526.

[15] D. L. Batiste *et al.*, “High-resolution MRI and micro-CT in an ex vivo rabbit anterior cruciate ligament transection model of osteoarthritis,” *Osteoarthr. Cartil.*, vol. 12, no. 8, pp. 614–626, 2004, doi: 10.1016/j.joca.2004.03.002.

[16] L. Xie, A. S. P. Lin, K. Kundu, M. E. Levenston, N. Murthy, and R. E. Guldberg, “Quantitative imaging of cartilage and bone morphology, reactive oxygen species, and vascularization in a rodent model of osteoarthritis,” *Arthritis Rheum.*, vol. 64, no. 6, pp. 1899–1908, Jun. 2012, doi: 10.1002/art.34370.

[17] G. Mohan, E. Perilli, J. S. Kuliwaba, J. M. Humphries, I. H. Parkinson, and N. L. Fazzalari, “Application of in vivo micro-computed tomography in the temporal characterisation of subchondral bone architecture in a rat model of low-dose monosodium iodoacetate-induced osteoarthritis,” *Arthritis Res. Ther.*, vol. 13, no. 6, p. R210, 2011, doi: 10.1186/ar3543.

[18] R. D. Kapadia *et al.*, “Applications of micro-CT and MR microscopy to study pre-clinical models of osteoporosis and osteoarthritis,” *Technol. Heal. Care*, vol. 6, no. 5–6, pp. 361–372, Jan. 1998, doi: 10.3233/thc-1998-65-609.

[19] M. Sode, A. J. Burghardt, R. A. Nissenson, and S. Majumdar, “Resolution Dependence of the Non-metric Trabecular Structure Indices,” *Bone*, vol. 42, no. 4, pp. 728–736, Apr. 2008, doi: 10.1016/J.BONE.2007.12.004.

[20] C. M. Brechbühler, G. Gerig, and O. Kubler, “Parametrization of closed surfaces for 3-D shape description,” *Comput. Vis. Image Underst.*, vol. 61, no. 2, pp. 154–170, Mar. 1995, doi: 10.1006/cviu.1995.1013.

[21] N. Otter, M. A. Porter, U. Tillmann, P. Grindrod, and H. A. Harrington, “A roadmap for the computation of persistent homology,” *EPJ Data Sci.*, vol. 6, p. 17, 2017, doi: 10.1140/epjds/s13688-017-0109-5.

[22] C. M. Brechbühler, “Description and analysis of 3-D shapes by parametrization of closed surfaces,” Swiss Federal Institute of Technology Zurich, Zurich, 1995.

[23] S. Huber, “Persistent Homology in Data Science,” *3rd Int. Data Sci. Conf. (iDSC’20)*, May 2020.

[24] T. Weinkauf and D. Günther, “Separatrix persistence: Extraction of salient edges on surfaces using topological methods,” *Eurographics Symp. Geom. Process.*, vol. 28, no. 5, pp. 1519–1528, 2009.

[25] Y. Kozlov and T. Weinkauf, “Persistence1D: Extracting and filtering minima and maxima of 1d functions.” 2015, Accessed: Nov. 10, 2020. [Online]. Available: https://www.csc.kth.se/~weinkauf/notes/persistence1d.html.

[26] K. S. Stok *et al.*, “Consensus approach for 3D joint space width of metacarpophalangeal joints of rheumatoid arthritis patients using high-resolution peripheral quantitative computed tomography,” *Quant. Imaging Med. Surg.*, vol. 10, no. 2, pp. 314–325, Feb. 2020, doi: 10.21037/qims.2019.12.11.

[27] T. K. Koo and M. Y. Li, “A Guideline of Selecting and Reporting Intraclass Correlation Coefficients for Reliability Research,” *J. Chiropr. Med.*, vol. 15, no. 2, pp. 155–163, Jun. 2016, doi: 10.1016/j.jcm.2016.02.012.

[28] T. Kohler, M. Beyeler, D. Webster, and R. Müller, “Compartmental bone morphometry in the mouse femur: reproducibility and resolution dependence of microtomographic measurements.,” *Calcif. Tissue Int.*, vol. 77, no. 5, pp. 281–90, Nov. 2005, doi: 10.1007/s00223-005-0039-2.

[29] D. V. Cicchetti, “Guidelines, Criteria, and Rules of Thumb for Evaluating Normed and Standardized Assessment Instruments in Psychology,” *Psychol. Assess.*, vol. 6, no. 4, pp. 284–290, 1994, doi: 10.1037/1040-3590.6.4.284.

[30] M. Styner *et al.*, “Framework for the Statistical Shape Analysis of Brain Structures using SPHARM-PDM.,” *Insight J.*, no. 1071, pp. 242–250, 2006, Accessed: Mar. 06, 2020. [Online]. Available: http://www.ncbi.nlm.nih.gov/pubmed/21941375.

[31] A. Fedorov *et al.*, “3D Slicer as an image computing platform for the Quantitative Imaging Network,” *Magn. Reson. Imaging*, vol. 30, no. 9, pp. 1323–1341, Nov. 2012, doi: 10.1016/j.mri.2012.05.001.

[32] A. M. McCoy, “Animal Models of Osteoarthritis: Comparisons and Key Considerations,” *Vet. Pathol.*, vol. 52, no. 5, pp. 803–818, Sep. 2015, doi: 10.1177/0300985815588611.

[33] S. Althloothi, M. H. Mahoor, and R. M. Voyles, “A robust method for rotation estimation using spherical harmonics representation,” *IEEE Trans. Image Process.*, vol. 22, no. 6, pp. 2306–2316, 2013, doi: 10.1109/TIP.2013.2249083.

[34] H. E. Benseddik, H. Hadj-Abdelkader, B. Cherki, and S. Bouchafa, “Direct method for rotation estimation from spherical images using 3D mesh surfaces with SPHARM representation,” *J. Vis. Commun. Image Represent.*, vol. 40, no. Part B, pp. 708–720, Oct. 2016, doi: 10.1016/j.jvcir.2016.08.010.

[35] K. Toraichi, K. Katagishi, I. Sekita, and R. Mori, “Computational complexity of spline interpolation,” *Int. J. Syst. Sci.*, vol. 18, no. 5, pp. 945–954, 1987, doi: 10.1080/00207728708964021.

[36] D. J. Hunter, L. Sharma, and T. Skaife, “Alignment and Osteoarthritis of the Knee,” *J. Bone Jt. Surgery-American Vol.*, vol. 91, no. Suppl 1, pp. 85–89, Feb. 2009, doi: 10.2106/JBJS.H.01409.

[37] C. Peterfy *et al.*, “Comparison of fixed-flexion positioning with fluoroscopic semi-flexed positioning for quantifying radiographic joint-space width in the knee: Test-retest reproducibility,” *Skeletal Radiol.*, vol. 32, no. 3, pp. 128–132, Mar. 2003, doi: 10.1007/S00256-002-0603-Z.

[38] M. Kothari *et al.*, “Fixed-flexion radiography of the knee provides reproducible joint space width measurements in osteoarthritis,” *Eur. Radiol.*, vol. 14, no. 9, pp. 1568–1573, Sep. 2004, doi: 10.1007/S00330-004-2312-6.

Supplementary material

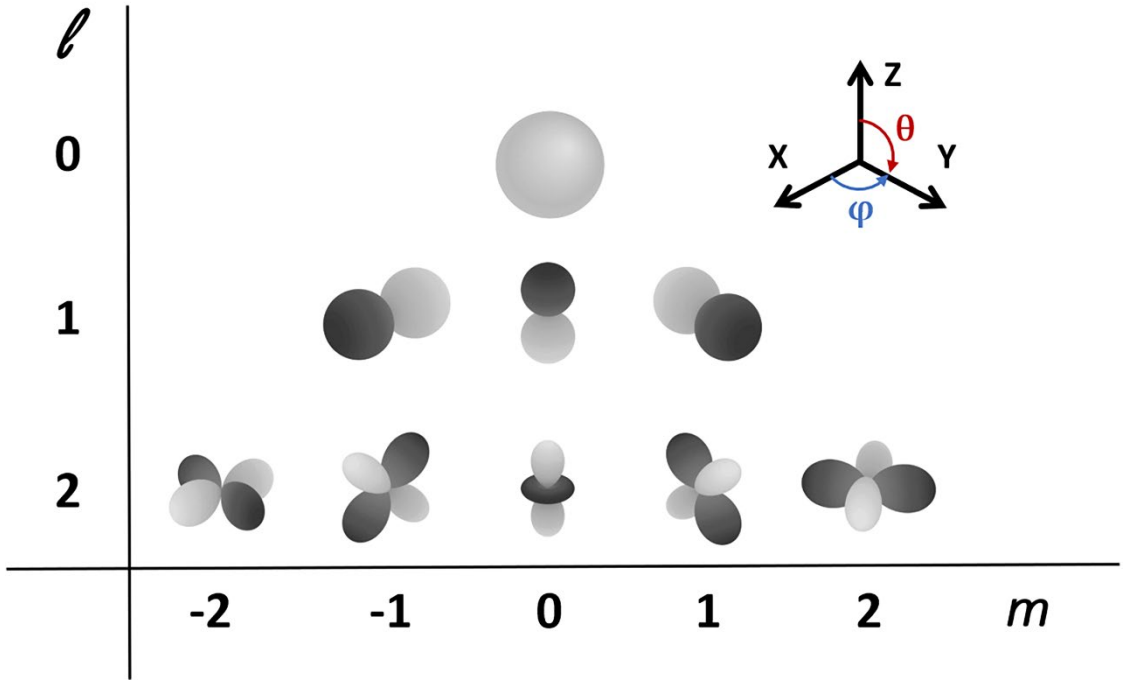

Supplementary Figure 5-S1: Visual representations of real spherical harmonics for the first few low values of l and m.

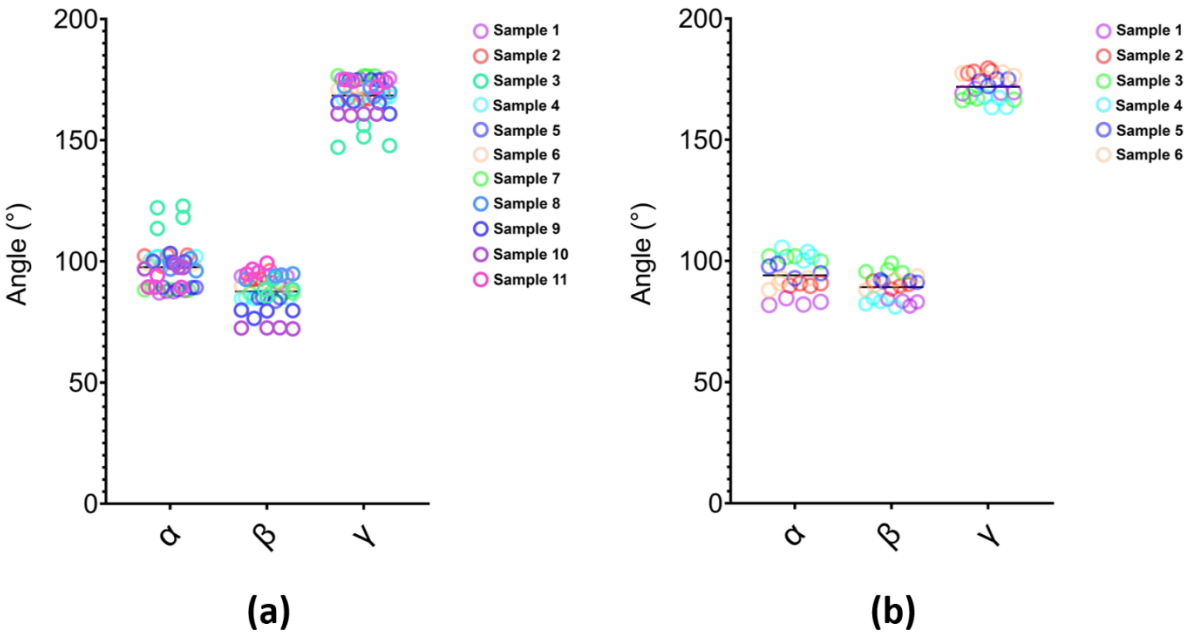

Supplementary Figure 5-S2: Sample-wise scatterplot of centre of mass measurement results for (a) rat and (b) rabbit samples after processing with the alignment module. Colour denotes repeated measurement of the same sample.

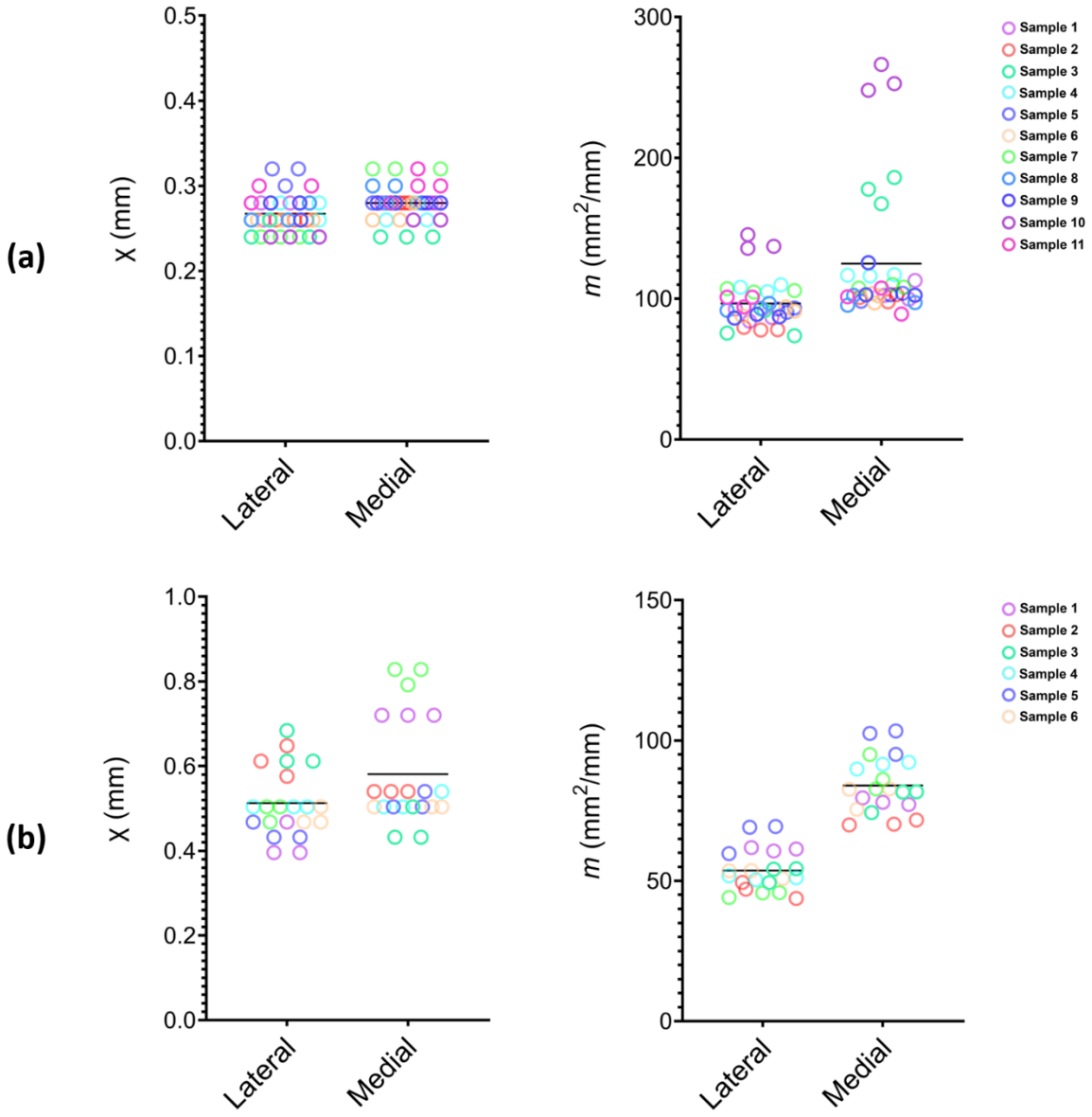

Supplementary Figure 5-S3: Sample-wise scatterplot of in silico loading contact area measurement results for rat (in row a) and rabbit (in row b) samples after processing with the alignment and subdivision module. Colour denotes repeated measurement of the same sample.

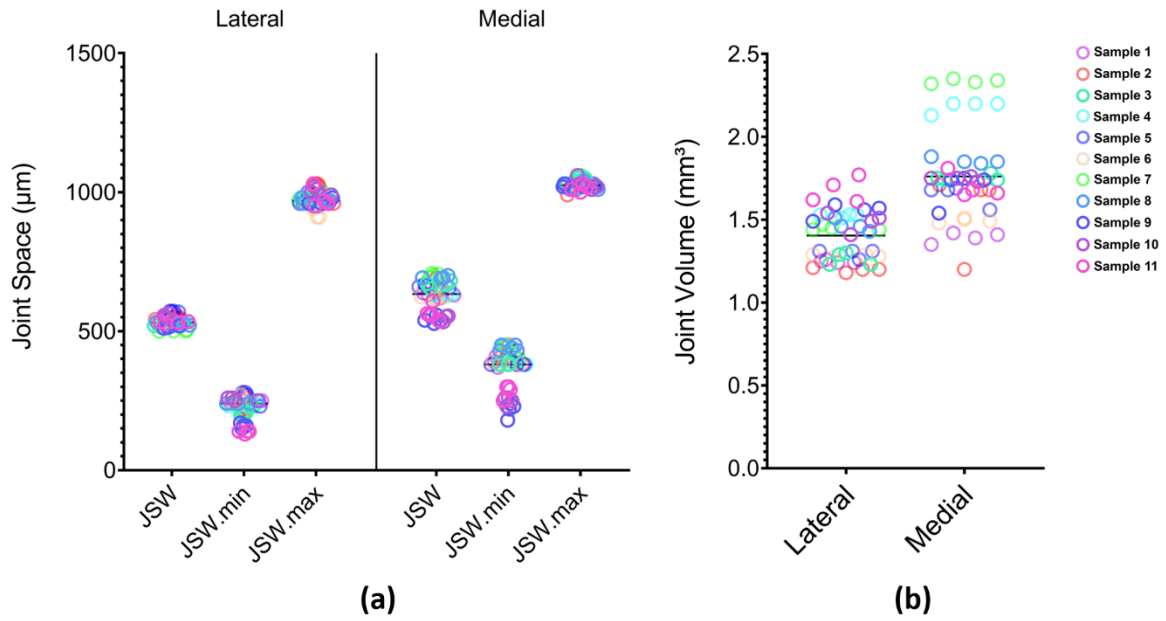

Supplementary Figure 5-S4: Sample-wise scatterplot of joint space measurement results for rat samples for (a) JSW and (b) JSV after processing with the alignment and subdivision module. Colour denotes repeated measurement of the same sample.

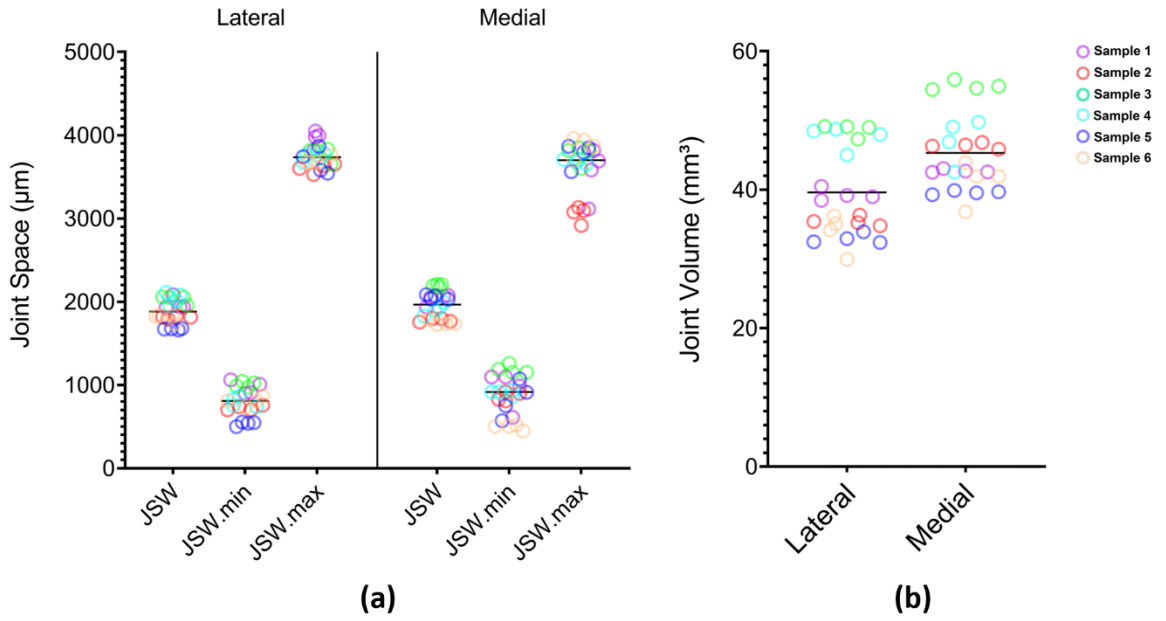

Supplementary Figure 5-S5: Sample-wise scatterplot of joint space measurement results for rat samples for (a) JSW and (b) JSV after processing with the alignment and subdivision module. Colour denotes repeated measurement of the same sample.

Result of SPHARM degree parametric study

Supplementary Table 5-S6: Reproducibility of the rat and rabbit joint centre of mass in terms of intraclass correlation coefficient (ICC) obtained by aligning models with different SPHARM degree. Gray row highlighted the most optimum SPHARM degree.

SPHARM Degree	Rat (10 µm voxel size)			Rabbit (18 µm voxel size)		
	α	β	γ	α	β	γ
20	0.954	0.956	0.952	0.942	0.915	0.915
10	0.953	0.955	0.950	0.940	0.919	0.915
5	0.955	0.958	0.951	0.936	0.920	0.934
4	0.954	0.954	0.951	0.938	0.920	0.915
3	0.954	0.955	0.952	0.938	0.919	0.915
2	0.956	0.954	0.952	0.940	0.920	0.916
1	0.955	0.953	0.951	0.938	0.919	0.916

Reproducibility for 3D joint centre of mass of unprocessed data

Supplementary Table 5-S7: Reproducibility of the rat and rabbit joint centre of mass in terms of intraclass correlation coefficient (ICC) and precision errors (PE) when PCA alignment was performed directly on unprocessed data.

Rat (10 µm voxel size) Unprocessed					
	ICC	Lower 95%	Upper 95 %	PE (SD)	PE (%CV)
λ (mm)	0.863	0.702	0.955	0.06	1.18%
α (°)	0.577	0.282	0.836	10.98	13.60%
β (°)	0.890	0.755	0.965	1.39	1.54%
γ (°)	0.731	0.483	0.906	3.84	26.27%
Rabbit (18 µm voxel size) Unprocessed					
	ICC	Lower 95%	Upper 95 %	PE (SD)	PE (%CV)
λ (mm)	0.986	0.952	0.998	0.23	1.61%
α (°)	0.901	0.702	0.984	2.38	2.71%
β (°)	0.739	0.379	0.951	3.66	4.11%
γ (°)	0.385	-0.005	0.843	2.60	1.52%

Joint QMA results from previous studies of OA in small animal models

Supplementary Table 5-S8: Joint QMA results from previous study of rat OA [12] *with 11 control samples (NO) and 11 samples with OA induced through anterior cruciate ligament transection and medial meniscectomy (OP). (10 µm voxel size, p < 0.05).*

		NO		OP		
		Mean	± SD	Mean	± SD	p
JSW (µm)	Lateral	565.3	62.2	718.9	129.4	*
	Medial	539.3	43.7	625.6	72.8	*
JSV (mm^3)	Lateral	2.42	0.59	1.63	0.29	*
	Medial	1.78	0.35	2.31	0.56	*
JSW.min (µm)	Lateral	215.00	97.67	342.09	209.20	
	Medial	73.0	36.5	206.7	157.9	*
JSW.max (µm)	Lateral	1089.0	12.0	1101.4	18.5	
	Medial	1087.0	17.0	1098.6	16.6	
α (°)		102.1	8.5	83.7	25.6	*
β (°)		98.1	2.1	98.1	3.7	
γ (°)		15.7	6.4	25.1	10.2	*
χ (mm)	Lateral	0.16	0.05	0.18	0.10	
	Medial	0.09	0.02	0.05	0.08	
m (mm^2/mm)	Lateral	39.2	5.6	34.0	8.4	
	Medial	35.1	3.1	27.0	11.2	

Supplementary Table 5-S9: Joint QMA results from previous study of rabbit OA [11] *with 8 control samples (NO) and 8 samples with OA induced through anterior cruciate ligament transection (OP). (18 µm voxel size, p < 0.05).*

		NO		OP		
		Mean	± SD	Mean	± SD	p
JSW (µm)	Lateral	3D JSW analysis was not performed in this study.				
	Medial					
JSV (mm^3)	Lateral					
	Medial					
JSW.min (µm)	Lateral					
	Medial					
JSW.max (µm)	Lateral					
	Medial					
α (°)		96.7	8.0	91.0	7.4	*
β (°)		94.4	3.4	93.7	3.2	
γ (°)		169.5	4.7	172.3	3.8	
χ (mm)	Lateral	0.15	0.05	0.60	0.35	*
	Medial	0.23	0.12	0.30	0.19	
m (mm^2/mm)	Lateral	38.2	8.2	71.0	40.0	*
	Medial	49.9	12.8	45.4	11.1	

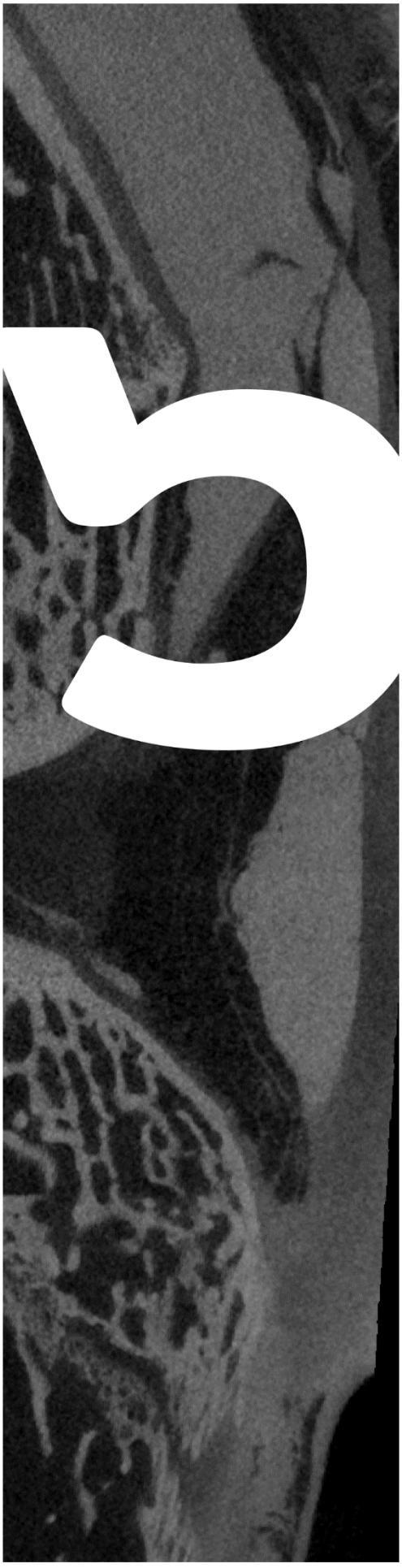

Chapter 6
Analysis

Empirical probabilistic approach
for QMA of osteophyte activity

Chapter 6

6.1 Chapter introduction

Traditionally, quantitative morphometric analysis (QMA) is often performed using workflows based on morphological operations such as dilation and erosion which are dependent on animal scale and voxel size. Parametric tuning of multiple variables must be performed for every new study to ensure consistent and valid QMA outcomes, presenting reproducibility and efficiency issues. This chapter presents an automatic and model-invariant solution to QMA using empirical probabilistic approach to statistically model morphological changes due to osteoarthritis (OA) by detecting osteophyte activity.

This chapter is based on the manuscript entitled "Automatic, objective, and resolution invariant approach for quantitative assessment of osteophyte in rabbit and rat trauma models of osteoarthritis" which is **in progress** towards submission.

Automatic, objective, and resolution invariant approach for quantitative assessment of osteophyte in rabbit and rat trauma models of osteoarthritis

Pholpat Durongbhan[1], Catherine E. Davey[1], Kathryn S. Stok[1]

[1]Department of Biomedical Engineering, The University of Melbourne, Parkville, Australia

6.2 Abstract

Objective: This study aims to investigate and develop an automated and resolution-invariant 3D image processing approach for quantitative assessment of osteophytes. Crucially, it is independent of baseline models and is validated using experimental rabbit and rat trauma models of knee osteoarthritis.

Design: Micro-computed tomography scans of rabbit and rat tibiofemoral joints, along with their histological OARSI grading, were obtained from previous OA studies. Cortical bone was segmented, and a 3D sphere-fitting transform was performed to obtain a thickness map, for which each voxel is assigned a thickness value corresponding to the size of the largest sphere containing the voxel that fits entirely within the cortical bone. From the thickness map, a 1-voxel thick outer surface was extracted to model surface roughness. The thickness values of the outer surface were empirically estimated by a series of known statistical distributions. Parameters describing best-fit distributions, along with cortical thickness and porosity were analysed to determine sensitivity to osteoarthritis and the presence of osteophytes.

Results: Visual inspection shows that samples with osteoarthritis and the presence of osteophytes have an increase in surface voxels assigned small thickness values. The distributions of thickness values for each animal are best described by a Gamma distribution, across both the rabbit and rat datasets. The shape parameter of the Gamma distribution is consistently sensitive to osteoarthritis and the presence of osteophytes in two animal models, while other parameters are not.

Conclusions: Combining traditional image processing with empirical distribution fitting provides an automated, objective, and resolution-invariant method for osteophyte assessment.

6.3 Introduction

Osteophytes are a hallmark feature of osteoarthritis (OA) and are often used as a marker to define the presence of disease [1] in clinical assessments. Despite the prevalence of osteophyte formation, its role and purpose in OA pathogenesis is still unclear [2]. Currently, grading schemes are available for semi-quantitative assessment of osteophytes in both 2D and 3D imaging modalities. Implementing these grading schemes in a longitudinal radiographic study has shown its potential to uncover the role of osteophyte size in OA progression; nonetheless, 2D assessments may miss the extent, size, and location of osteophytes which could be quantitatively analysed with higher sensitivity and accuracy using 3D datasets [3], Figure 6-1.

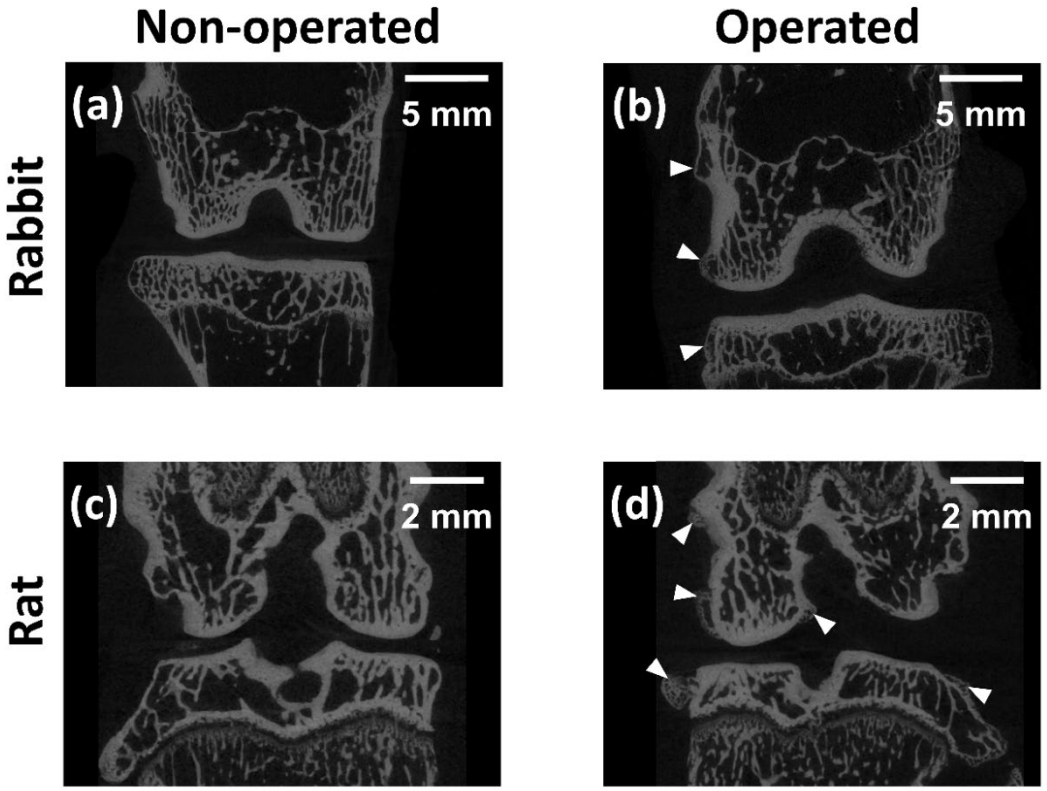

Figure 6-1: Typical greyscale microCT images of (a,b) rabbit and (c,d) rat, non-operated and operated samples, respectively, indicating the presence of osteophytes along the periarticular margins (white arrow heads).

Recent studies have shown that quantitative assessment of osteophytes can be done in human hand OA using clinical computed tomography (CT) [4]–[6] and small animal knee OA using micro-computed tomography (microCT) [7]–[10]. Osteophyte volume is often reported using various approaches for osteophyte segmentation, namely: manual segmentation [8], [11]–[13], subtraction of the diseased model from a control sample to obtain their differences [4], [9], [10], and using a matching library of models or creating average shapes from which

statistical shape analysis can be performed [5], [6], [14], [15]. However, manual segmentation is time consuming and inconsistent, potentially leading to reproducibility and efficiency issues. On the other hand, the quality and reproducibility of the described automated methods are highly reliant on the availability, size, and quality of the baseline models (i.e., average models, control samples, model library) used to extract osteophytes for subsequent volumetric analysis.

Alternatively, an automated and objective assessment of osteophytes, independent of baseline models, could be achieved by evaluating bone surface derangement. As additional outgrowths on normal bone surface, osteophytes disrupt the integrity of the cortical surface of the periarticular bone, leading to an abnormally coarse exterior. Previous studies [7], [16] have quantified surface disruptions in murine models of rheumatoid arthritis using microCT datasets. Their approach was done by measuring the ratio between a sample's actual, rough surface, and a smooth, ideal surface, by assuming that an over-smoothed surface is a good representation of the diseased sample in its healthy form. However, this can introduce artifacts to the results where surfaces that are naturally rough, even in healthy controls, could be artificially smoothed and incorrectly identified as pathologically affected.

Based on the idea of assessing surface disruptions, without assuming idealised surfaces, this study hypothesises that quantitative assessment of osteophytes through surface derangements can be achieved using an approach based on a combination of empirical data exploration and 3D thickness [17].

Briefly described, local thickness at a given point in the structure is defined as the diameter of the largest sphere that incorporates the point and can be entirely fitted inside the structure [17]. As each local point in the structure is assigned a thickness value, they can be empirically approximated by a known distribution, providing an automatic, objective, and resolution-independent approach to parameterisation and analysis [18]. In regions with osteophytes, the resulting coarse surface restricts the fitting of larger spheres to the underlying periarticular bone cortex due to changing cortical porosity and inconsistent mineralisation. This leads to a clustering of voxels with small thickness values around cortical surfaces with osteophytes and an overall shift of the estimated thickness distribution towards smaller values.

Based on this concept, we aim to investigate and develop an image processing approach that can quantitatively assess the local presence of osteophytes while addressing shortfalls in previous proposals. The method proposed in this work calculates the 3D thickness of the periarticular cortical bone and extracts the thickness values assigned to voxels at the outer surface. A histogram of these values is empirically fitted to a distribution. The distribution parameters are analysed with histological scoring for osteoarthritis and osteophyte severity, as well as compared against other traditional morphometric measurements of periarticular cortical bone. The approach is validated using high-resolution microCT scans of the tibiofemoral joints from earlier rabbit [19] and rat [20] studies of post-traumatic OA, to demonstrate its sensitivity and application across differing voxel sizes and animal models.

6.4 Materials and methods

6.4.1 Animals and microCT scan protocols

The datasets used in this study were obtained from previous studies of rabbit and rat trauma models of OA, whose protocols were approved by the Cantonal Ethics Commission of Bern (Permit Number: 49/10) and are described in detail in respective publications [19], [20]. For the rabbit dataset, eight healthy New Zealand white rabbits, 4.5 months in age and 3.5 ± 0.4 kg, underwent anterior cruciate ligament transection (ACLT) on the right knee (rabbit operated, OP, n = 8), while the left joint was used as contralateral control (rabbit non-operated, NO, n = 8). Animals were sacrificed eight weeks after operation. For the rat dataset, nine healthy male Wistar rats, 3 months in age and 565 ± 48 g, underwent anterior cruciate ligament transection and medial meniscectomy (ACLT + MMx) on the right knee (rat operated, OP, n = 9), and left knees were kept as contralateral controls (rat non-operated, NO, n = 9). Animals were sacrificed three weeks after operation.

For both datasets, intact joints were dissected to include soft tissue and scanned within 3 hours while stored at 4°C. MicroCT scans (SCANCO Medical AG, Brüttisellen, Switzerland) were obtained with 300 ms integration time, 70 kVp voltage source, and 8 W power with an isotropic voxel size of 18 µm and 10 µm for rabbit and rat datasets, respectively. The volume of interest was defined with the epiphyseal bone of the femur as the upper limit and the epiphyseal bone of the tibia as the lower limit and centring around the femoral condyles and

the tibia plateau. All microCT data were reconstructed and filtered using a constrained 3D Gaussian filter (window, σ = 1.2, support, s = 1).

6.4.2 Histological preparation and scoring

As described previously [19], [20], joints were disarticulated after scanning and prepared for histology [21], [22]. The femurs and tibias were subsequently decalcified, dehydrated, and embedded in paraffin. Three µm sections (sagittal slices for rabbits and frontal slices for rats) comprising of cartilage and underlying subchondral bone were stained with Safranin-O/Fast Green (Fluka, Sigma Aldrich, MO, USA). For semi-quantitative scoring, three histology sections per each femur and tibia were digitised using light microscope (Leica DM/RB, Leica AG, Germany). The resulting series of overlapping sub-images were stitched together using ImageJ [23], and each histology image was registered to a corresponding microCT slice using a custom C++ script [24]. Semi-quantitative evaluation was done on Safranin-O/Fast Green stained sections using OARSI histopathology guidelines for rabbit [21] and rat [22] models of osteoarthritis. The assessment included a scoring scheme for osteophyte severity which ranges from 0 (absent) to 4 (severe).

It was noted in this study that some contralateral control samples developed osteophytes after OA induction while some operated samples did not. To validate the workflow's quantitative result with gradings of osteophyte presence, the rabbit and rat datasets were categorised into groups without osteophyte (NS) and with osteophyte (OS) according to the described osteophyte grading such that every sample in the non-osteophyte group has an osteophyte score of 0.

6.4.3 Periarticular cortical surface analysis

Images of the femur and tibia were segmented using a global thresholding procedure [25] (Figure 6-2a) and separated into cortical and trabecular components (Figure 6-2b) using previously described automated algorithms [26]. 3D cortical thickness was determined using a spherical distance transform [27], which estimates a volume-based local thickness for every voxel by fitting maximal spheres to every point in the structure. The thickness of a voxel is defined as the diameter of the largest sphere incorporating that voxel, which can be fitted entirely inside the structure of interest. Applying this technique to the cortical bone resulted

in a bone thickness map (Figure 6-2c). A 1-voxel thick outer surface was extracted with each voxel encoded for its thickness from the distance transform (Figure 6-2d). A histogram of voxel thickness values for the outer cortical surface was plotted for subsequent analysis (Figure 6-2e).

Using the segmented cortical bone, structural measurements of cortical morphometry (cortical thickness (Ct.Th, μm), cortical porosity (Ct.Po, %)) were also evaluated.

6.4.4 Data analysis and statistics

A series of common distributions were fitted to each thickness histogram (Figure 6-2e) using MATLAB (MathWorks, Natick, MA, USA); namely, Birnbaum–Saunders, exponential, generalised extreme value, Gamma, half-normal, inverse Gaussian, kernel, logistic, log-logistic, lognormal, Nakagami, Gaussian, Rayleigh, Rician, and Weibull distributions. The best-fit distribution for each sample was determined by calculating the maximum likelihood estimates (MLE), and identifying the distribution with the optimal negative log-likelihood. The best MLE fit for the majority of samples was defined as the best fit distributions for the datasets.

Statistical analysis was performed using GraphPad Prism (GraphPad Software, Inc., Version 8.0.0, San Diego, CA, USA) and RStudio (RStudio: Integrated development environment for R, Version 0.95.258, Boston, MA, USA). Parameters describing the best fit distribution, along with the measured cortical thickness and porosity, were tested for normality using Shapiro-Wilk test and visually examined using Q-Q plot. Homogeneity of variance of the dataset was tested with an F-test. A paired Student's t-test was used to test for significant differences between non-operated (NO) and operated groups (OP). For comparisons between groups with (OS) and without (NS) osteophytes an unpaired Student's t-tests were performed. All tests were two-sided, and a p-value < 0.05 was considered statistically significant.

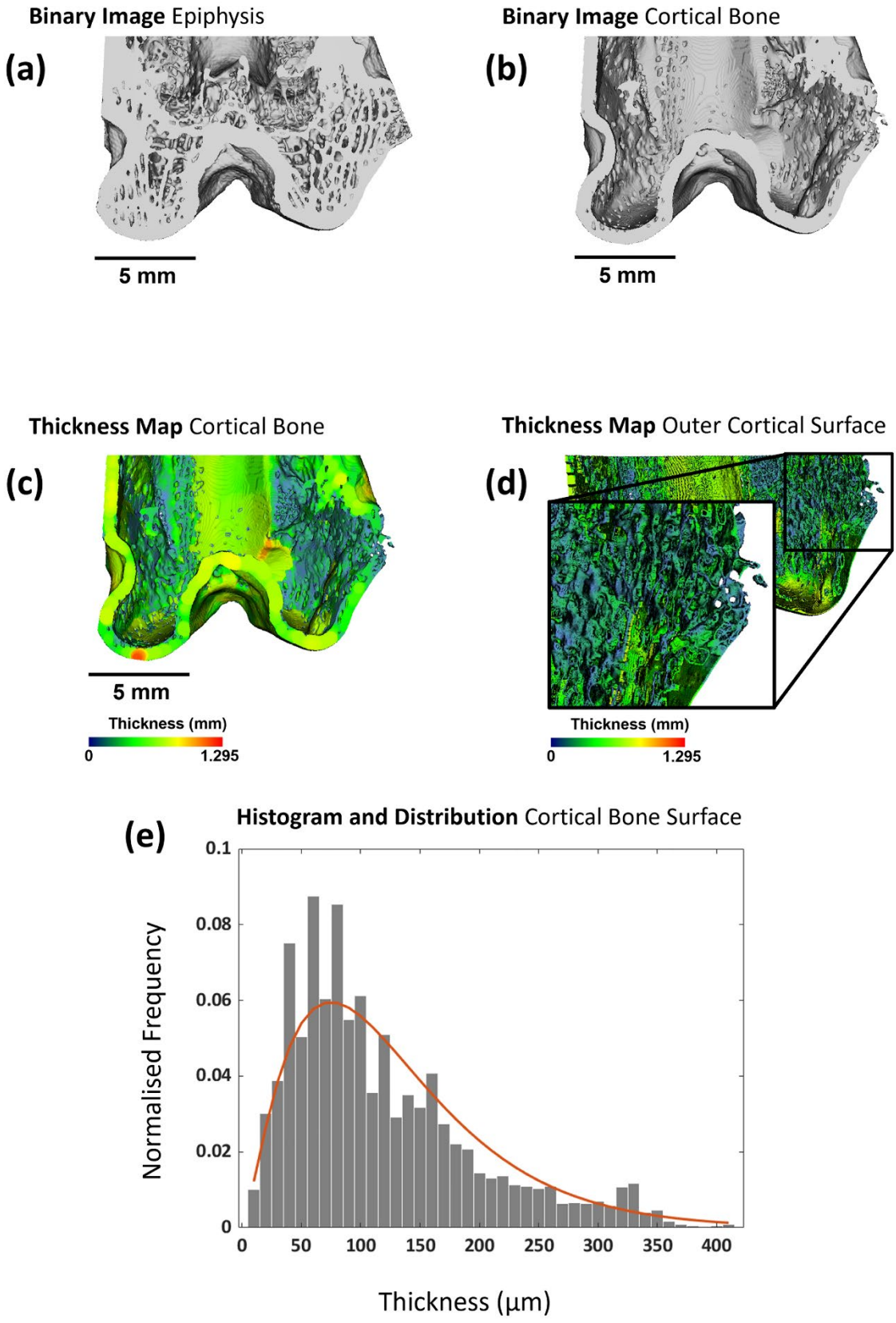

Figure 6-2: Periarticular cortical surface analysis workflow. (a) A binary image of segmented femur or tibia is used as the input. (b) Cortical and epiphyseal bone are separated [26] *and the cortical shell is retained. (c) A thickness map of the cortical bone is obtained using 3D sphere-fitting* [27]*. (d) The outer surface of the cortical bone is extracted. (Inset: Surface with osteophytes enlarged) (e) Histogram of the cortical surface thickness map is obtained and fits of the thickness distribution (red line) are calculated for analysis.*

6.5 Results

6.5.1 Dataset characteristics

The characteristics of the groups categorised with and without osteophytes, along with the original operated and non-operated groups, are presented in Table 6-1. Of the 16 rabbit knees used in this study, two operated femurs and one operated tibia did not develop any visible osteophyte, while one non-operated tibia developed osteophyte. For the 18 rat knees, four operated femurs and one operated tibia did not develop osteophyte, and no non-operated bones developed osteophyte.

Table 6-1: Summary of the datasets used in this study where the number of samples for each group (n) and their OARSI and osteophyte scores (mean (SD)) are shown. Groups without (NS) and with (OS) osteophytes were derived from non-operated and operated groups such that groups without osteophytes have osteophyte scores of 0. Original non-operated and operated data were collected in previous studies [19], [20].

		Femur				Tibia			
		Non-operated (NO)	Operated (OP)	Without Osteophyte (NS)	With Osteophyte (OS)	Non-operated (NO)	Operated Joint (OP)	Without Osteophyte (NS)	With Osteophyte (OS)
Rabbit	n	8	8	10	6	8	8	8	8
	OARSI score (0 - 24)	3.6 (1.4)	9.0 (3.2)	5.0 (3.6)	8.2 (2.6)	4.9 (1.6)	11.4 (4.8)	4.8 (1.5)	11.3 (4.5)
	Osteophyte score (0 – 4)	0.0 (0.0)	0.6 (0.7)	0.0 (0.0)	0.8 (0.6)	0.2 (0.6)	2.2 (1.0)	0.0 (0.0)	2.4 (0.6)
Rat	n	9	9	13	5	9	9	10	8
	OARSI score (0 - 15)	9.7 (2.9)	12.3 (1.5)	10.0 (2.5)	13.2 (1.2)	6.4 (2.1)	11.9 (1.3)	7.3 (2.3)	12.0 (1.5)
	Osteophyte score (0 – 4)	0.1 (0.1)	0.9 (0.7)	0.0 (0.0)	1.3 (0.6)	0.1 (0.1)	1.1 (0.6)	0.0 (0.0)	1.3 (0.5)

6.5.2 Visual inspection and distribution fitting

Typical images of the periarticular cortical surface analysis and their normalised histograms are presented in Figure 6-3, where surface voxels with small thickness values are highlighted. It can be seen from visual inspections that small voxel values are typically clustered around osteophytes with rough surface areas. When comparing the histograms between non-operated and operated samples for both animals in Figure 6-3, a shift toward smaller voxel thickness values can be observed (blue arrows).

Results for empirical MLE distribution fitting are presented in Figure 6-S1 (rabbit femur), Figure 6-S2 (rabbit tibia), Figure 6-S3 (rat femur), and Figure 6-S4 (rat tibia). A Gamma distribution was found to yield the optimal negative log-likelihood in most samples for both animal datasets (17 out of 32 for rabbit, 31 out of 36 for rat). Nakagami (8 out of 32 for rabbit, 3 out of 36 for rat) was the distribution with the next highest number of optimal fits. Therefore, the Gamma distribution was selected as optimal. It is characterised by the shape (k) and scale (θ) parameters which, in general terms, describe the skewness and the range of the distribution, respectively.

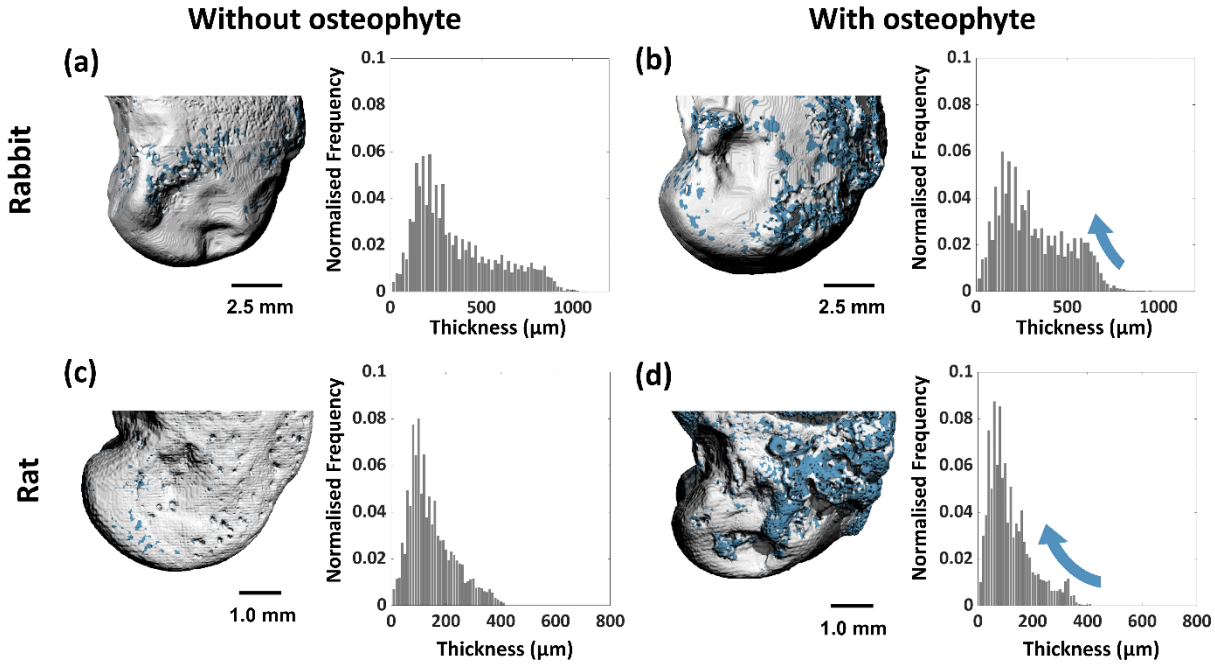

Figure 6-3: Exemplar periarticular cortical surface analysis highlighting areas with low thickness values (in blue) and their accompanying histogram. Thickness maps are thresholded at 90 µm and 50 µm for rabbit and rat samples, respectively. Typical results for a rabbit pair (a) without and (b) with osteophytes, and a rat pair (c) without and (d) with osteophytes. Arrows in histograms for samples with osteophytes highlight the shift toward smaller surface thickness values compared to samples without osteophytes.

6.5.3 Sensitivity analysis of the fitted Gamma distribution

Histograms of the surface thickness and estimated Gamma distribution for each rabbit and rat (femur and tibia) samples are shown in Figures 6-S5 to 6-S8, respectively. The summary statistics of the fitted Gamma distributions, described in terms of their shape (k) and scale (θ) parameters, for each group are shown in the first two rows of Table 6-2. Shapiro-Wilk test results do not show evidence of non-normality (Table 6-S1) for both parameters. Further visual inspections of QQ plots (data not shown) support this conclusion. F-test results comparing non-operated to operated and without and with osteophyte groups do not show evidence of variance inhomogeneity (Table 6-S2). For each parameter, comparisons between each group are presented as mean difference with 95% confidence intervals (Figure 6-4).

As seen in Figure 6-4a, the shape parameter values, k, in operated groups are significantly smaller than non-operated groups for both bones in both animal datasets, with mean difference ranging from -0.24 for rat tibia ($p = 0.004$) to -0.37 ($p < 0.001$) for rat femur. Smaller shape parameter values, k, were also recorded for both bones in both animal datasets when comparing with to without osteophyte groups (mean difference of -0.22 for rabbit tibia ($p = 0.026$) to mean difference of -0.45 for rat femur ($p < 0.001$). Additionally, the mean difference of k for both bones are smaller in rat non-operated versus operated comparisons, in contrast to those from groups with versus without osteophyte comparisons, while the mean difference of k for both bones in rabbit non-operated versus operated comparisons changed slightly compared to rabbit with versus without osteophyte comparisons.

There are also generally slight, but not significant, increases in the scale parameter value, θ, for both comparisons (operated versus non-operated, with versus without osteophytes) across all datasets (Figure 6-4b). The largest increase in θ can be observed in the rabbit femur datasets where mean differences of 16.76 ($p = 0.010$) and 19.93 ($p = 0.045$) were observed for non-operated versus operated and with versus without osteophyte comparisons, respectively.

6.5.4 Sensitivity analysis of other cortical morphometric measurements

Summary statistics for other cortical measurements (Ct.Th, Ct.Po) are shown in Table 6-2. Shapiro-Wilk test and F-test results do not show evidence of non-normality (Table 6-S1) nor variance inhomogeneity (Table 6-S2). Additionally, for each parameter, comparisons between each group are presented as mean difference with 95% confidence intervals in Figure 6-4c and Figure 6-4d. Results show that the mean difference between non-operated versus operated and with versus without osteophyte comparisons for these parameters are generally small and not statistically significant.

Table 6-2: Summary statistics for parameters of the fitted Gamma distribution and other morphometric metrics of the cortical bone. Parameters shown are: shape (k) and scale (θ) of the fitted Gamma distribution, cortical thickness (Ct.Th), and cortical porosity (Ct.Po) in mean (SD). (NO: non-operated group, OP: operated group, NS: group without osteophyte, OS: group with osteophyte)

		Femur						Tibia					
		NO	OP	p	NS	OS	p	NO	OP	p	NS	OS	p
Rabbit	k (1)	2.83 (0.20)	2.58 (0.21)	0.005	2.81 (0.19)	2.54 (0.21)	0.029	2.38 (0.16)	2.12 (0.14)	0.008	2.36 (0.19)	2.14 (0.14)	0.026
	θ (1)	125.27 (13.79)	144.53 (16.14)	0.010	126.18 (16.18)	146.11 (16.75)	0.045	85.23 (8.25)	89.28 (12.27)	0.332	85.82 (9.36)	88.69 (11.62)	0.620
	Ct.Th (µm)	573.2 (48.8)	565.6 (55.3)	0.680	565.3 (52.3)	576.2 (51.5)	0.712	703.9 (41.8)	714.8 (81.3)	0.686	713.2 (52.6)	705.5 (60.4)	0.827
	Ct.Po (%)	17.5 (2.6)	16.5 (1.6)	0.430	16.9 (2.6)	17.2 (1.2)	0.777	18.2 (1.3)	19.3 (1.5)	0.303	18.1 (1.3)	19.4 (1.4)	0.101
Rat	k (1)	2.83 (0.15)	2.46 (0.17)	< 0.001	2.76 (0.20)	2.31 (0.12)	< 0.001	2.40 (0.23)	2.16 (0.27)	0.004	2.44 (0.25)	2.08 (0.17)	0.004
	θ (1)	47.86 (4.18)	53.63 (4.09)	0.012	49.74 (5.19)	53.37 (3.45)	0.192	50.16 (5.55)	52.09 (7.84)	0.484	49.09 (6.17)	53.66 (6.84)	0.180
	Ct.Th (µm)	234.2 (18.8)	251.9 (17.2)	0.017	245.4 (17.3)	236.9 (24.8)	0.447	205.2 (18.2)	210.9 (16.7)	0.536	207.5 (21.2)	208.6 (16.3)	0.910
	Ct.Po (%)	24.0 (2.3)	24.6 (2.5)	0.713	24.3 (2.8)	24.3 (0.9)	0.948	22.8 (1.3)	22.5 (2.1)	0.707	22.3 (2.0)	23.0 (1.2)	0.435

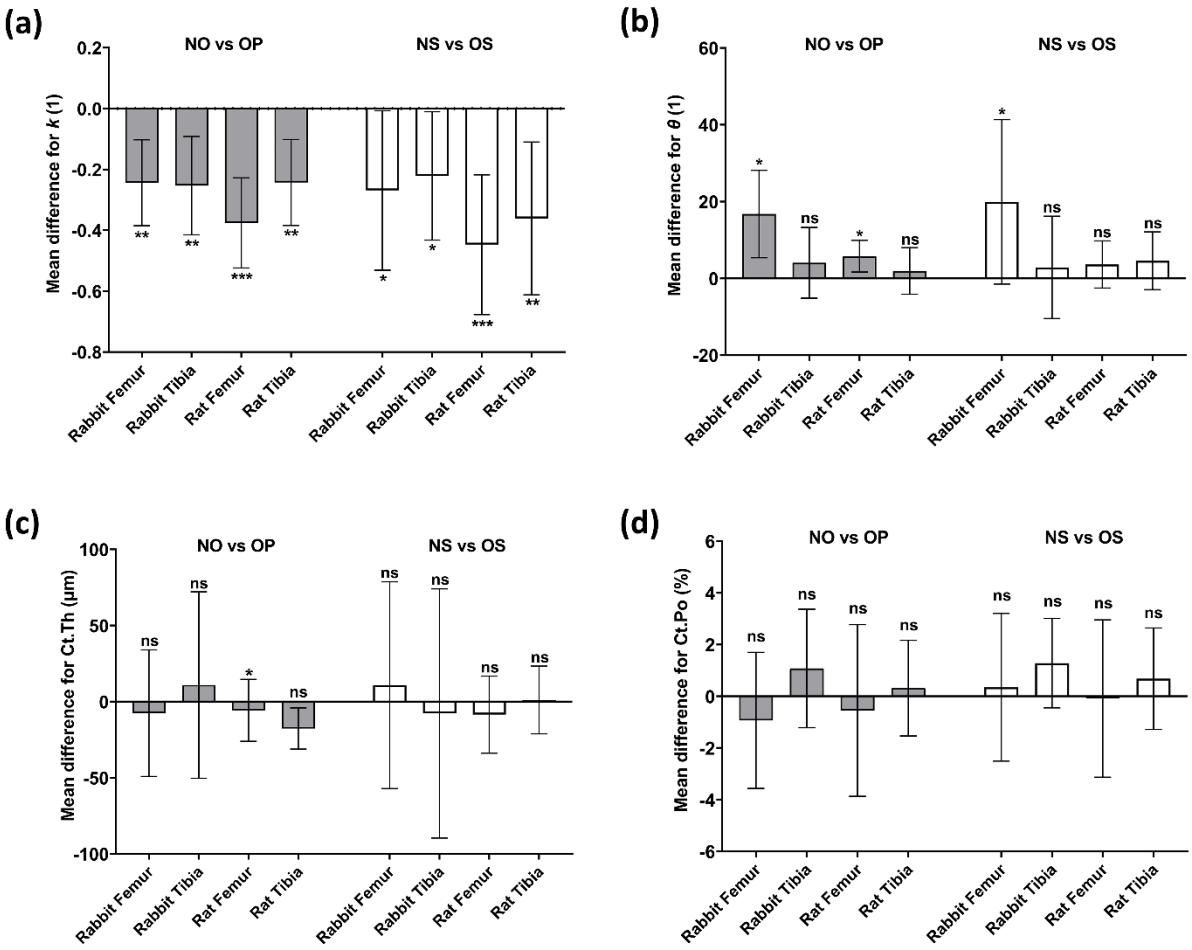

Figure 6-4: Mean difference with 95% confidence interval for (a) shape, k and (b) scale, θ parameters of the fitted Gamma distribution and for (c) cortical thickness (Ct.Th) and (d) cortical porosity (Ct.Po) for the femur and tibia of the rat and rabbit datasets. For each group, comparisons were made for non-operated (NO) versus operated (OP) samples (in grey) and samples without (NS) versus with (OS) osteophytes (in white). Asterisks denotes statistically significant differences (: $p < 0.05$, **: $p < 0.01$, ***: $p < 0.001$)*

6.6 Discussion

This study investigated a novel, automatic, objective, and resolution-invariant approach for the quantification of osteophyte activity in animal models of OA that is independent of baseline cohorts. The results confirm the stated hypothesis that using an approach based on the combination of empirical data exploration and a 3D thickness transform, quantitative assessment of osteophytes through surface derangements can be achieved. An increase in surface roughness restricts the fitting of larger spheres for 3D thickness at the surface and leads to a change in overall distribution of thickness values. Through empirical fitting of the Gamma distribution, it is possible to obtain a statistical description of the overall shape and scale of the histogram of the surface thickness while remaining invariant to the animal scale and image voxel size.

Validated on microCT datasets of rabbit and rat posttraumatic models of tibiofemoral OA, the approach does not require re-adjustment between animal models and images with different resolutions. Its key contribution lies in the ability to distinguish between non-operated and operated samples and, using osteophyte scores, between samples with and without osteophytes as well. This work builds upon the concept of capturing bone surface roughness explored in previous studies [7], [16] and was implemented as a novel, automated, and objective approach that fully appreciates the 3D nature of the datasets without making assumptions of idealised, smoothed surfaces. Moreover, the performance of the approach is not reliant on the availability of longitudinal scans [10], average model [5], [6], or a library of matches [28]. Taken together, the workflow can be deployed in new studies without requiring high technical input, recalibration to match animal and voxel size, or access to other datasets.

Interestingly, MLE results found that outer surface thickness values typically fit best to the Gamma distribution, followed by Nakagami distribution. Both are related [29] and are appropriate for real-valued, non-negative, continuous observations [30]. A Gamma random variable with shape parameter, k, and scale parameter, θ, is equivalent to the square of a Nakagami random variable with its shape, $m = k$, and spread, $\Omega = k\theta$, (i.e., $X = Y^2 \text{ when } X \sim \Gamma(k, \theta), \text{ and } Y \sim \text{Nakagami}(k, k\theta)$) [29].

Gamma distribution is the most common non-normal distribution used in health sciences [31], which is also the case in this study. With the Gamma distribution, a histogram of surface thickness can be summarily described in terms of its shape, k, and scale, θ, parameters, whose changes affect the shape and spread of the distribution, respectively. This approach could be useful for describing the shift towards small thickness values observed in samples with OA and osteophytes, as seen in this study.

As shown in Figure 6-4a, there is a general decrease in k in non-operated versus operated and with versus without osteophyte comparisons, in accordance with the visual changes in the shape of the histogram in Figure 6-3. No significant changes to θ are anticipated because the overall scale of the histogram is unchanged compared to controls. This matches with the finding in which there are generally small but statistically insignificant increases in k in all comparisons except for the rabbit femur. More considerable θ increases for the rabbit femur can be attributed to the loss of voxels with high thickness values in operated samples and samples with osteophytes, leading to a change in the tail length of the Gamma distribution

compared with controls (Figure 6-S5). Further visual inspection of raw scans show that surface disruptions in rabbit femurs are more severe, and larger thickness values do not appear as frequently. Regardless, the shift towards smaller thickness values is still reflected in k for those datasets.

Manual grading of histology performed in previous studies (Table 6-1) showed that osteophyte scores are higher in all samples with osteophytes when compared to samples without. However, these increases in osteophyte activity were not appropriately reflected by traditional morphometric measurement of cortical bone, as seen in Figure 6-3c and Figure 6-3d. It is noted that almost all traditional cortical measures of the periarticular bone have small and insignificant mean differences with no noticeable pattern between those without versus with osteophyte comparisons. In contrast, k values obtained in this study show a consistently negative mean difference for the same set of comparisons across different bones and animal models. This suggests that traditional morphometric analysis of the cortical bone is insufficient to capture osteophytes at the surface as they are "diluted" by the whole volume thickness. In this context, k and θ may be helpful imaging markers to consider in future research on osteophytes.

In terms of limitations, the dataset, collected in previous studies [19], [20], used contralateral limbs as controls where abnormal biomechanical changes may still be present. Indeed, it was found that some contralateral control samples have high OARSI and osteophyte scores as well. By rearranging the datasets according to their osteophyte gradings, this effect could be mitigated; however, a dataset with additional controls would be preferable. Furthermore, the approach introduced in this study should be further validated with scorings and scans from a longitudinal study with a large number of samples where considerable variations in disease and osteophyte severity can be observed. This would allow regression analysis between gold standard OARSI osteophyte scoring and morphometric results [32]. Previously, semi-quantitative gradings, which are localised to the medial and lateral aspect of the joint, were done for the rat but not the rabbit datasets. To maintain consistency, this study only used gradings that were done for the whole joint. However, it has been reported that biomechanical changes in the bone and cartilage are different in different joint compartments [11], [33], so compartmental distinction may be of interest in future studies.

6.7 Conclusion

In conclusion, this work has presented a novel, automated, and objective 3D image processing approach for osteophyte assessment at the cortical surface, which is invariant to image resolution, animal model, and voxel size. The method is not reliant on access to other datasets and does not make assumptions on idealised, smoothed surfaces. Using 3D thickness transform and probability distribution fitting of surface voxel values, the study found that the shape parameter of the fitted Gamma distribution is sensitive to the presence of OA and osteophytes. Validated using previously obtained rabbit and rat datasets, the technique has the potential to be a valuable addition to the current suite of analysis methods for periarticular cortical bone.

6.8 Acknowledgement

This work was supported by the Discovery Projects scheme of the Australian Research Council (DP180101838) and the Christine and T Jack Martin Research Travel Grant of the Australian & New Zealand Bone & Mineral Society. Data used in this work is from previously studies supported by the Swiss Commission for Technology and Innovation CTI (Grant No. 9853.1).

References

[1] R. Altman *et al.*, "Development of criteria for the classification and reporting of osteoarthritis: Classification of osteoarthritis of the knee," *Arthritis Rheum.*, vol. 29, no. 8, pp. 1039–1049, 1986, doi: 10.1002/ART.1780290816.

[2] S. R. Goldring and M. B. Goldring, "Changes in the osteochondral unit during osteoarthritis: structure, function and cartilage-bone crosstalk," *Nat. Rev. Rheumatol.*, vol. 12, no. 11, pp. 632–645, Nov. 2016, doi: 10.1038/NRRHEUM.2016.148.

[3] D. T. Felson *et al.*, "Osteophytes and progression of knee osteoarthritis," *Rheumatology*, vol. 44, no. 1, pp. 100–104, Jan. 2005, doi: 10.1093/RHEUMATOLOGY/KEH411.

[4] K. Oura *et al.*, "Three-dimensional analysis of osteophyte formation on distal radius following scaphoid nonunion," *J. Orthop. Sci.*, vol. 22, no. 1, pp. 50–55, Jan. 2017, doi: 10.1016/j.jos.2016.06.018.

[5] J. J. Crisco, A. M. Morton, D. C. Moore, L. G. Kahan, A. L. Ladd, and A. P. C. Weiss, “Osteophyte growth in early thumb carpometacarpal osteoarthritis,” *Osteoarthr. Cartil.*, vol. 27, no. 9, pp. 1315–1323, Sep. 2019, doi: 10.1016/j.joca.2019.05.008.

[6] A. M. Morton, B. Akhbari, D. C. Moore, and J. J. Crisco, “Osteophyte volume calculation using dissimilarity-excluding Procrustes registration of archived bone models from healthy volunteers,” *J. Orthop. Res.*, vol. 38, no. 6, pp. 1307–1315, Jun. 2020, doi: 10.1002/jor.24569.

[7] M. D. Silva *et al.*, “Quantitative analysis of micro-CT imaging and histopathological signatures of experimental arthritis in rats,” *Mol. Imaging*, vol. 3, no. 4, pp. 312–318, 2004, doi: 10.1162/1535350042973562.

[8] H. M. Pauly *et al.*, “Assessment of cortical and trabecular bone changes in two models of post-traumatic osteoarthritis,” *J. Orthop. Res.*, vol. 33, no. 12, pp. 1835–1845, Dec. 2015, doi: 10.1002/JOR.22975.

[9] P. Das Neves Borges, T. L. Vincent, and M. Marenzana, “Automated assessment of bone changes in cross-sectional micro-CT studies of murine experimental osteoarthritis,” *PLoS One*, vol. 12, no. 3, p. e0174294, Mar. 2017, doi: 10.1371/journal.pone.0174294.

[10] A. W. Hsia, M. J. Anderson, M. A. Heffner, E. P. Lagmay, R. Zavodovskaya, and B. A. Christiansen, “Osteophyte formation after ACL rupture in mice is associated with joint restabilization and loss of range of motion,” *J. Orthop. Res.*, vol. 35, no. 3, pp. 466–473, Mar. 2017, doi: 10.1002/jor.23252.

[11] D. L. Batiste, A. Kirkley, S. Laverty, L. M. F. Thain, A. R. Spouge, and D. W. Holdsworth, “Ex vivo characterization of articular cartilage and bone lesions in a rabbit ACL transection model of osteoarthritis using MRI and micro-CT,” *Osteoarthr. Cartil.*, vol. 12, no. 12, pp. 986–996, Dec. 2004, doi: 10.1016/j.joca.2004.08.010.

[12] N. J. Willett, T. Thote, M. Hart, S. Moran, R. E. Guldberg, and R. V. Kamath, “Quantitative pre-clinical screening of therapeutics for joint diseases using contrast enhanced micro-computed tomography,” *Osteoarthr. Cartil.*, vol. 24, no. 9, pp. 1604–1612, Sep. 2016, doi: 10.1016/j.joca.2016.04.021.

[13] M. Yin, L. Schaefer, M. Sury, J. A. Lynch, and J. Duryea, “Osteophyte volume

measurements – Analysis of a subgroup of the FNIH OA Biomarker Cohort," *Osteoarthr. Cartil.*, vol. 24, pp. S269–S270, Apr. 2016, doi: 10.1016/j.joca.2016.01.506.

[14] T. F. Henchie, E. M. Gravallese, T. L. Bredbenner, and K. L. Troy, "An image-based method to measure joint deformity in inflammatory arthritis: development and pilot study," *Comput. Methods Biomech. Biomed. Engin.*, vol. 22, no. 10, pp. 942–952, Jul. 2019, doi: 10.1080/10255842.2019.1607315.

[15] P. K. Saha *et al.*, "A new osteophyte segmentation algorithm using the partial shape model and its applications to rabbit femur anterior cruciate ligament transection via micro-CT imaging," *IEEE Trans. Biomed. Eng.*, vol. 58, no. 8, pp. 2212–2227, Aug. 2011, doi: 10.1109/TBME.2011.2129519.

[16] M. Marenzana, A. Vugler, A. Moore, and M. Robinson, "Effect of sclerostin-neutralising antibody on periarticular and systemic bone in a murine model of rheumatoid arthritis: a microCT study," *Arthritis Res. Ther. 2013 155*, vol. 15, no. 5, pp. 1–12, Sep. 2013, doi: 10.1186/AR4305.

[17] T. Hildebrand and P. Rüegsegger, "Quantification of Bone Microarchitecture with the Structure Model Index," *Comput. Methods Biomech. Biomed. Engin.*, vol. 1, no. 1, pp. 15–23, 1997, doi: 10.1080/01495739708936692.

[18] G. J. Hahn and S. S. Shapiro, *Statistical models in engineering*. New York City, NY, USA: Wiley, 1994.

[19] K. S. Stok *et al.*, "Three-Dimensional Quantitative Morphometric Analysis (QMA) for In Situ Joint and Tissue Assessment of Osteoarthritis in a Preclinical Rabbit Disease Model," *PLoS One*, vol. 11, no. 1, p. e0147564, Jan. 2016, doi: 10.1371/journal.pone.0147564.

[20] B. A. Besler *et al.*, "Quantitative measures of bone shape, cartilage morphometry and joint alignment are associated with disease in an ACLT and MMx rat model of osteoarthritis," *Bone*, vol. 146, p. 115903, Feb. 2021, doi: 10.1016/j.bone.2021.115903.

[21] S. Laverty, C. A. Girard, J. M. Williams, E. B. Hunziker, and K. P. H. Pritzker, "The OARSI histopathology initiative - recommendations for histological assessments of osteoarthritis in the rabbit," *Osteoarthr. Cartil.*, vol. 18, no. SUPPL. 3, pp. S53–S65, Oct.

2010, doi: 10.1016/j.joca.2010.05.029.

[22] N. Gerwin, A. M. Bendele, S. Glasson, and C. S. Carlson, “The OARSI histopathology initiative - recommendations for histological assessments of osteoarthritis in the rat,” *Osteoarthr. Cartil.*, vol. 18, no. SUPPL. 3, pp. S24–S34, Oct. 2010, doi: 10.1016/j.joca.2010.05.030.

[23] S. Preibisch, S. Saalfeld, and P. Tomancak, “Globally optimal stitching of tiled 3D microscopic image acquisitions,” *Bioinformatics*, vol. 25, no. 11, pp. 1463–1465, Jun. 2009, doi: 10.1093/BIOINFORMATICS/BTP184.

[24] A. J. Trüssel, D. J. Webster, and R. Müller, “3D SPATIAL MAPPING OF OSTEOCYTES IN AN IN VIVO MODEL FOR BONE ADAPTATION,” *J. Biomech.*, vol. 45, p. S108, Jul. 2012, doi: 10.1016/S0021-9290(12)70109-4.

[25] K. S. Stok *et al.*, “Revealing the interplay of bone and cartilage in osteoarthritis through multimodal imaging of murine joints,” *Bone*, vol. 45, no. 3, pp. 414–422, Sep. 2009, doi: 10.1016/j.bone.2009.05.017.

[26] B. A. Besler, R. E. Sondergaard, R. Müller, and K. S. Stok, “Reproducibility of compartmental subchondral bone morphometry in the mouse tibiofemoral joint,” *Bone*, vol. 81, pp. 649–653, Dec. 2015, doi: 10.1016/J.BONE.2015.09.014.

[27] T. Hildebrand and P. Rüegsegger, “A new method for the model-independent assessment of thickness in three-dimensional images,” *J. Microsc.*, vol. 185, no. 1, pp. 67–75, Jan. 1997, doi: 10.1046/j.1365-2818.1997.1340694.x.

[28] A. J. Ramme *et al.*, “Automated Bone Segmentation and Surface Evaluation of a Small Animal Model of Post-Traumatic Osteoarthritis,” *Ann. Biomed. Eng.*, vol. 45, no. 5, pp. 1227–1235, May 2017, doi: 10.1007/s10439-017-1799-3.

[29] L.-F. Huang, “The Nakagami and its related distributions,” *WSEAS Trans. Math.*, vol. 15, pp. 477–485, 2016, Accessed: Jul. 20, 2022. [Online]. Available: https://www.semanticscholar.org/paper/The-Nakagami-and-its-related-distributions-Huang-Chuan/333a57886641b2dff2b1d26a18979884a9e629f8.

[30] J. Dagpunar, “The gamma distribution,” *Significance*, vol. 16, no. 1, pp. 10–11, Feb.

2019, doi: 10.1111/J.1740-9713.2019.01226.X.

[31] R. Bono, M. J. Blanca, J. Arnau, and J. Gómez-Benito, “Non-normal distributions commonly used in health, education, and social sciences: A systematic review,” *Front. Psychol.*, vol. 8, no. SEP, p. 1602, Sep. 2017, doi: 10.3389/FPSYG.2017.01602.

[32] A. Agresti, *Analysis of Ordinal Categorical Data*, 2nd ed. John Wiley & Sons, Incorporated, 2012.

[33] T. D. Turmezei *et al.*, “Quantitative three-dimensional assessment of knee joint space width from weight-bearing CT,” *Radiology*, vol. 299, no. 3, pp. 649–659, Jun. 2021, doi: 10.1148/RADIOL.2021203928.

Supplementary material

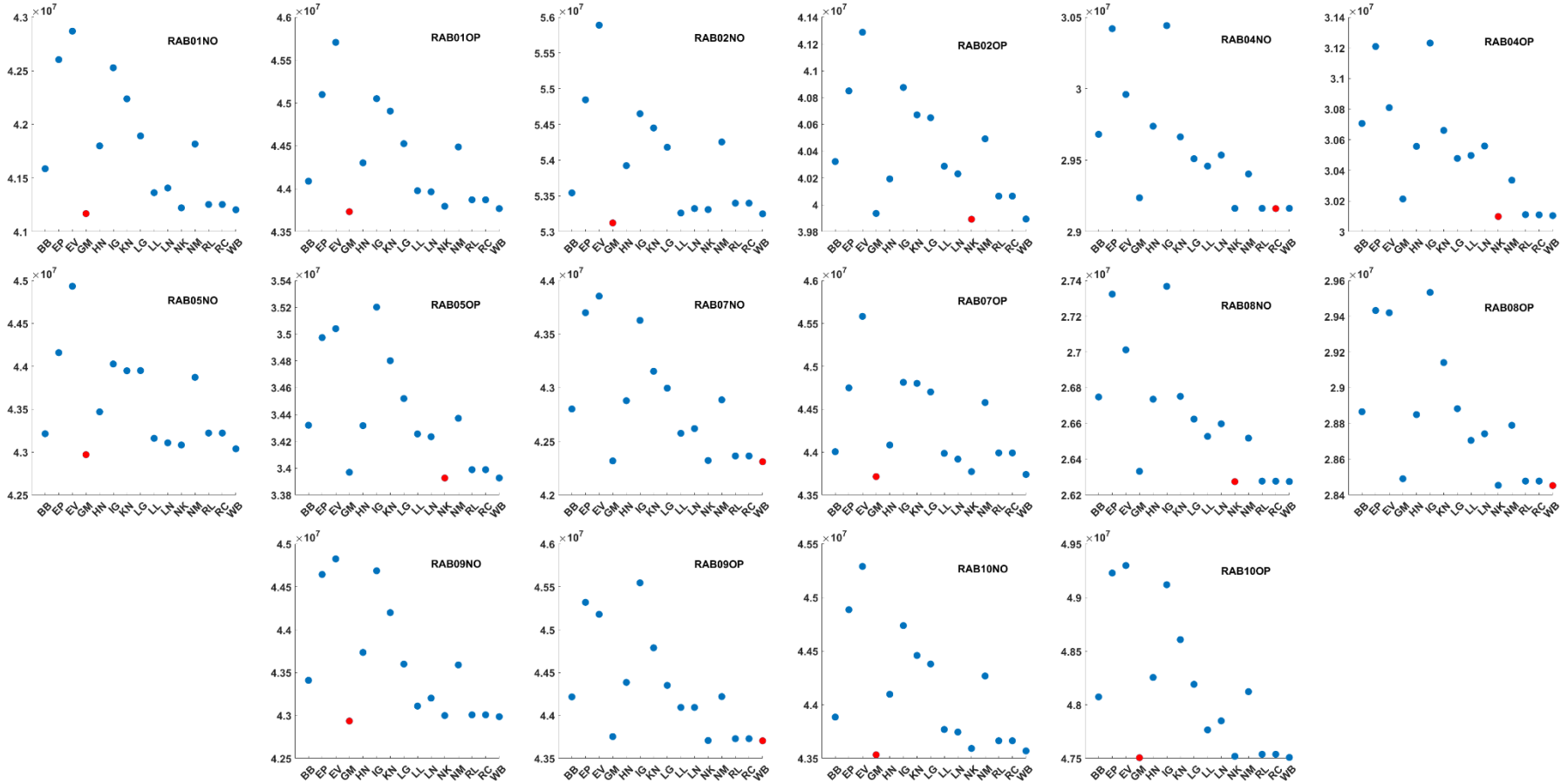

Supplementary Figure 6-S1: Comparison of maximum likelihood estimates (MLE) of distributions fitted to the histogram of surface thickness values for each rabbit femur sample. MLE was evaluated using negative log likelihood method and optimal fit is denoted with a red circle. The fitted distributions are, in order from left to right on x-axis, Birnbaum–Saunders (BB), exponential (EP), generalised extreme value (EV), Gamma (GM), half-normal (HN), inverse Gaussian (IG), kernel (KN), logistic (LG), log-logistic (LL), lognormal (LN), Nakagami (NK), Gaussian (NM), Rayleigh (RL), Rician (RC), and Weibull (WB) distributions.

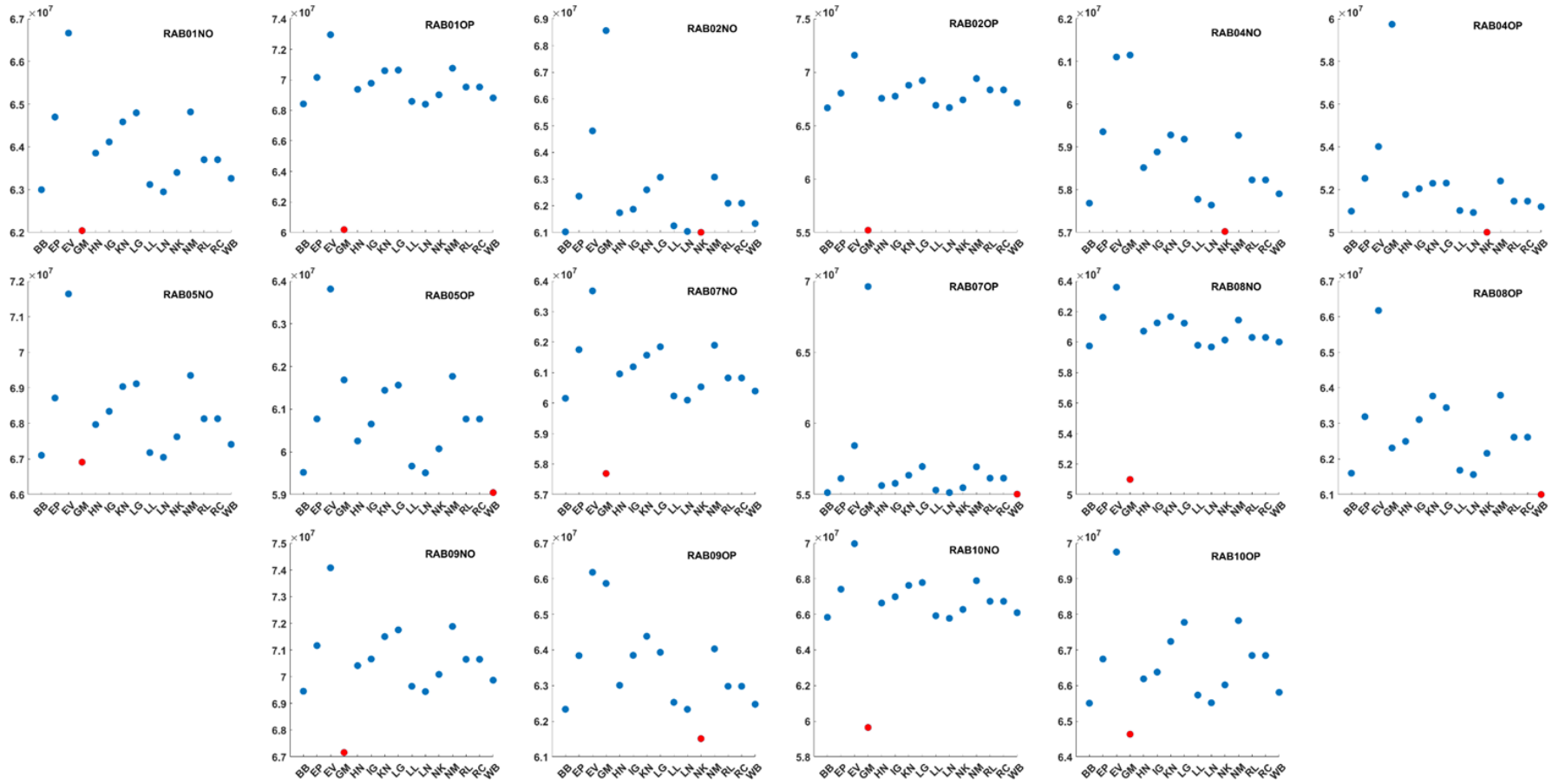

Supplementary Figure 6-S2: Comparison of maximum likelihood estimates (MLE) of distributions fitted to the histogram of surface thickness values for each rabbit tibia sample. MLE was evaluated using negative log likelihood method and optimal fit s denoted with a red circle. The fitted distributions are, in order from left to right on x-axis, Birnbaum–Saunders (BB), exponential (EP), generalised extreme value (EV), Gamma (GM), half-normal (HN), inverse Gaussian (IG), kernel (KN), logistic (LG), log-logistic (LL), lognormal (LN), Nakagami (NK), Gaussian (NM), Rayleigh (RL), Rician (RC), and Weibull (WB) distributions.

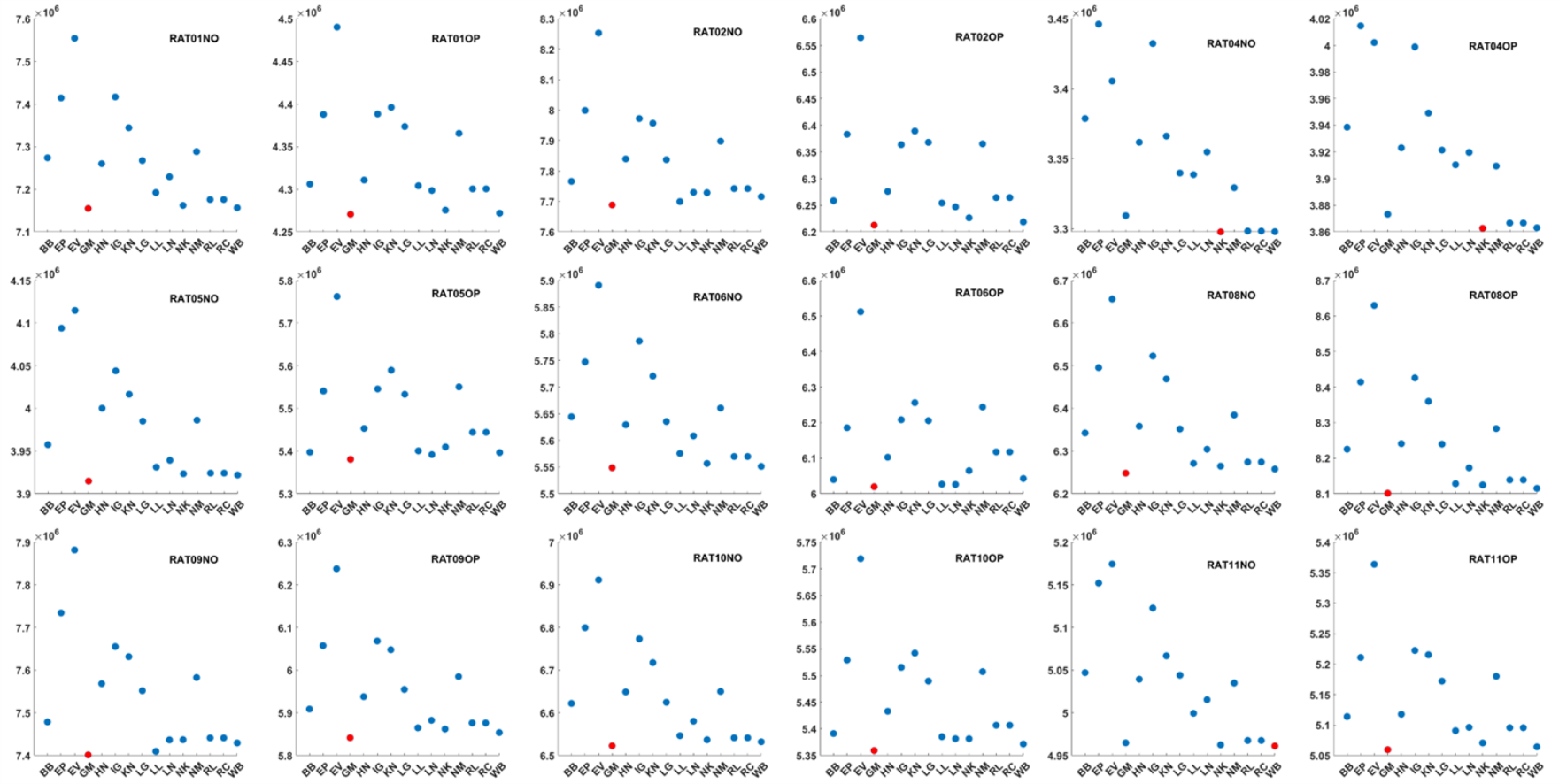

Supplementary Figure 6-S3: Comparison of maximum likelihood estimates (MLE) of distributions fitted to the histogram of surface thickness values for each rat femur sample. MLE was evaluated using negative log likelihood method and optimal fit is denoted with a red circle. The fitted distributions are, in order from left to right on x-axis, Birnbaum–Saunders (BB), exponential (EP), generalised extreme value (EV), Gamma (GM), half-normal (HN), inverse Gaussian (IG), kernel (KN), logistic (LG), log-logistic (LL), lognormal (LN), Nakagami (NK), Gaussian (NM), Rayleigh (RL), Rician (RC), and Weibull (WB) distributions.

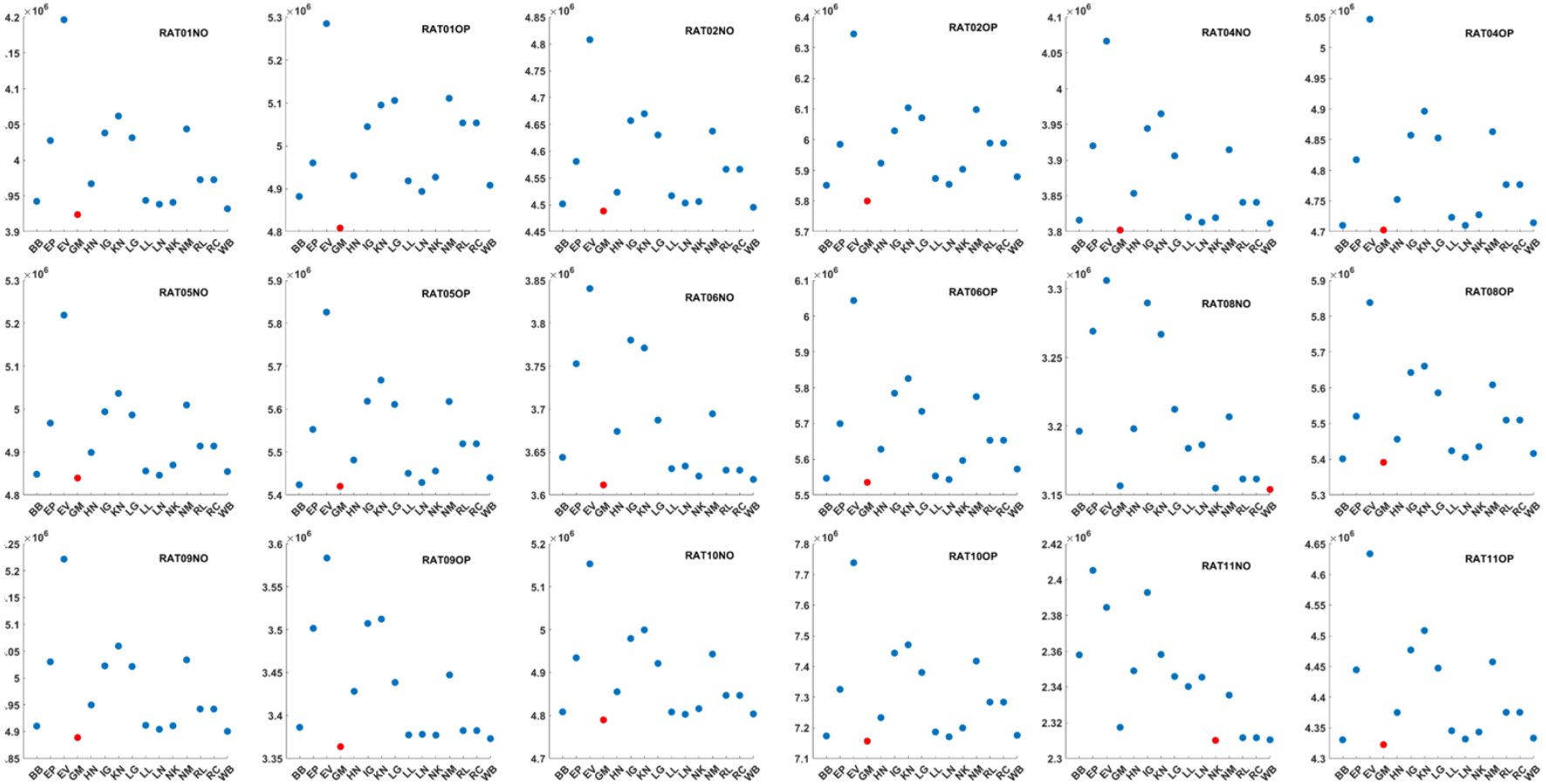

Supplementary Figure 6-S4: Comparison of maximum likelihood estimates (MLE) of distributions fitted to the histogram of surface thickness values for each rat tibia sample. MLE was evaluated using negative log likelihood method and optimal fit is denoted with a red circle. The fitted distributions are, in order from left to right on x-axis, Birnbaum–Saunders (BB), exponential (EP), generalised extreme value (EV), Gamma (GM), half-normal (HN), inverse Gaussian (IG), kernel (KN), logistic (LG), log-logistic (LL), lognormal (LN), Nakagami (NK), Gaussian (NM), Rayleigh (RL), Rician (RC), and Weibull (WB) distributions.

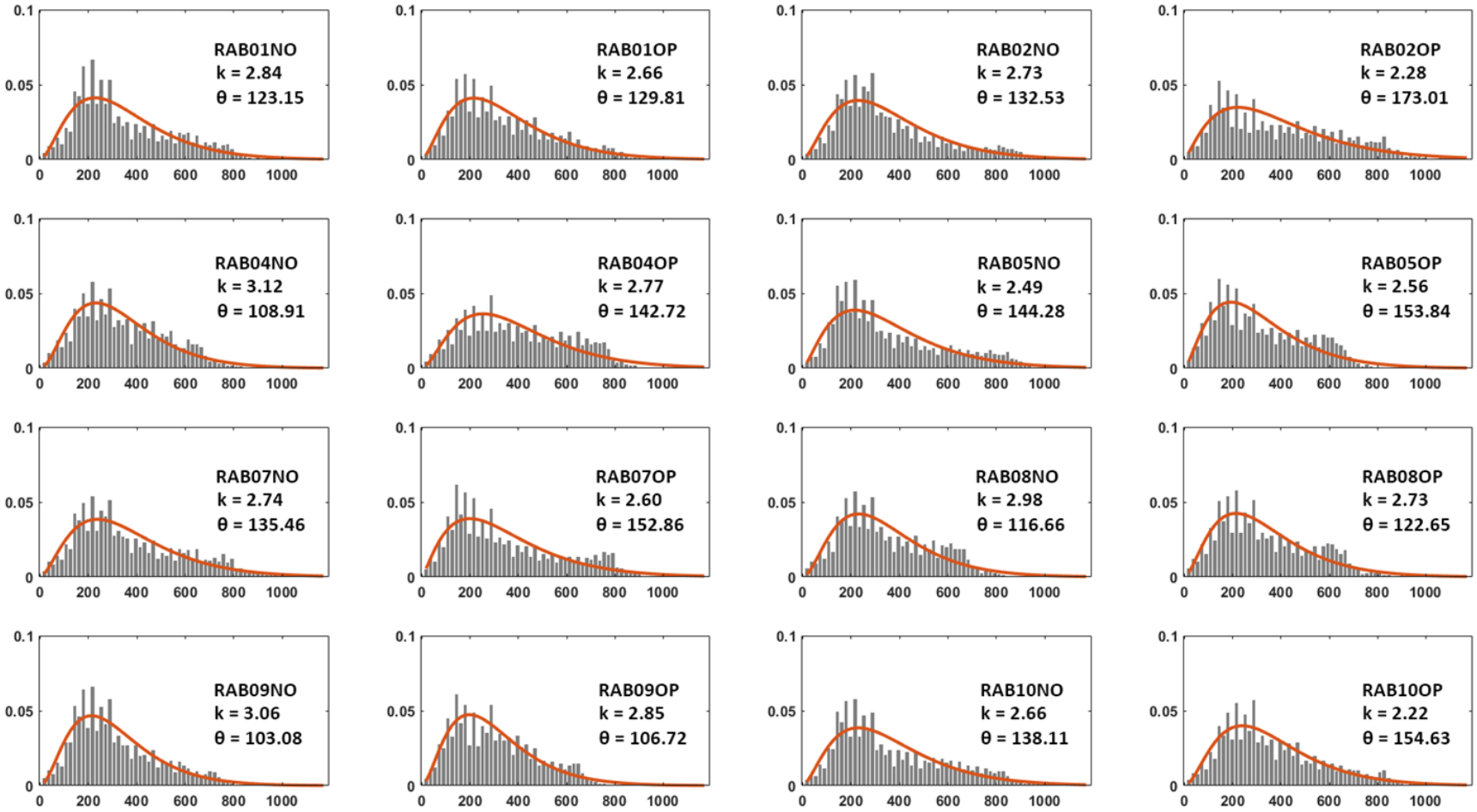

Supplementary Figure 6-S5: Histogram of surface thickness values and the estimated Gamma distribution (red) for each rabbit femur. Vertical axes show normalised frequency and the horizontal axes show thickness values in micrometre. (NO: control group, OP: operated group).

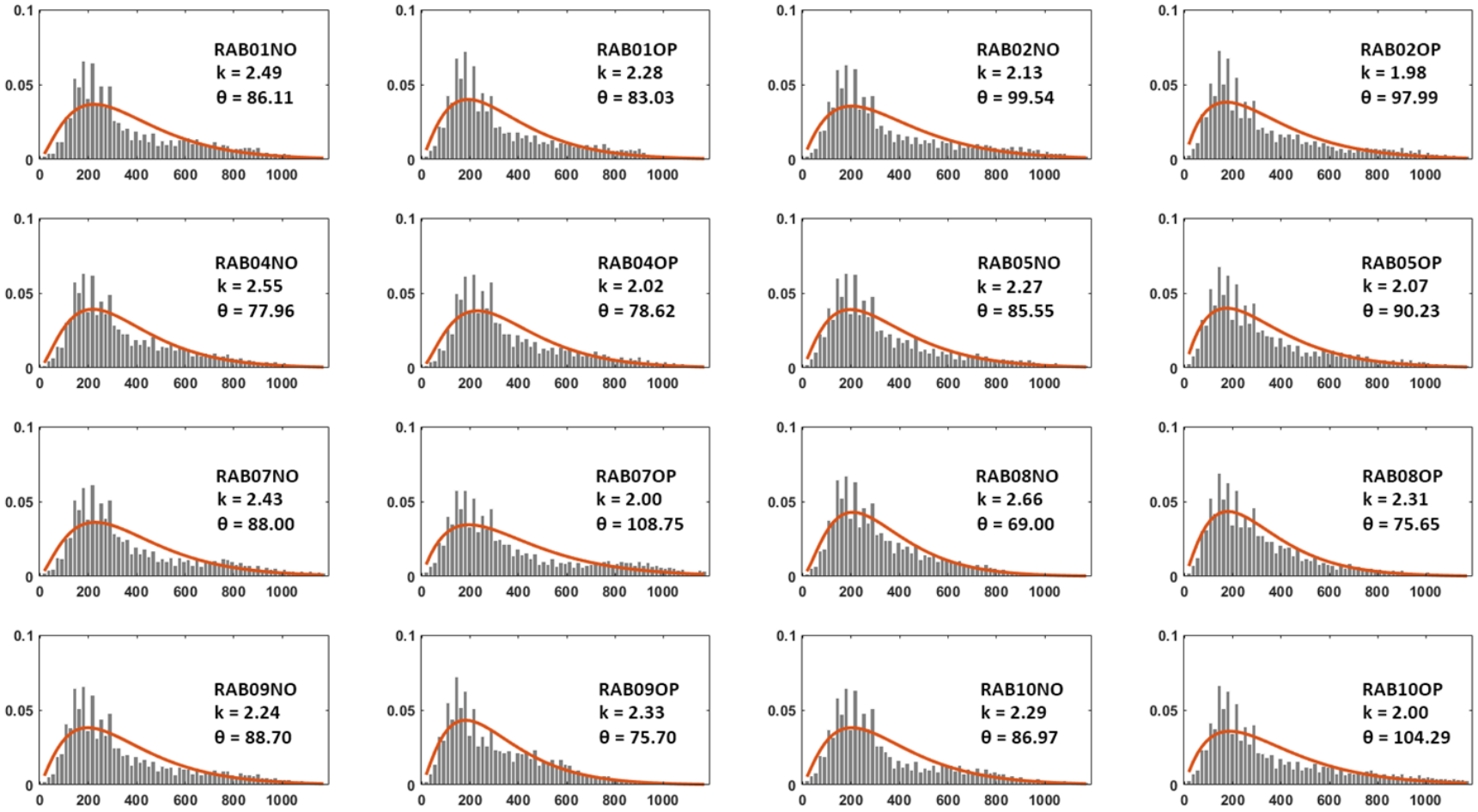

Supplementary Figure 6-S6: Histogram of surface thickness values and the estimated Gamma distribution (red) for each rabbit tibia. Vertical axes show normalised frequency and the horizontal axes show thickness values in micrometre. (NO: control group, OP: operated group).

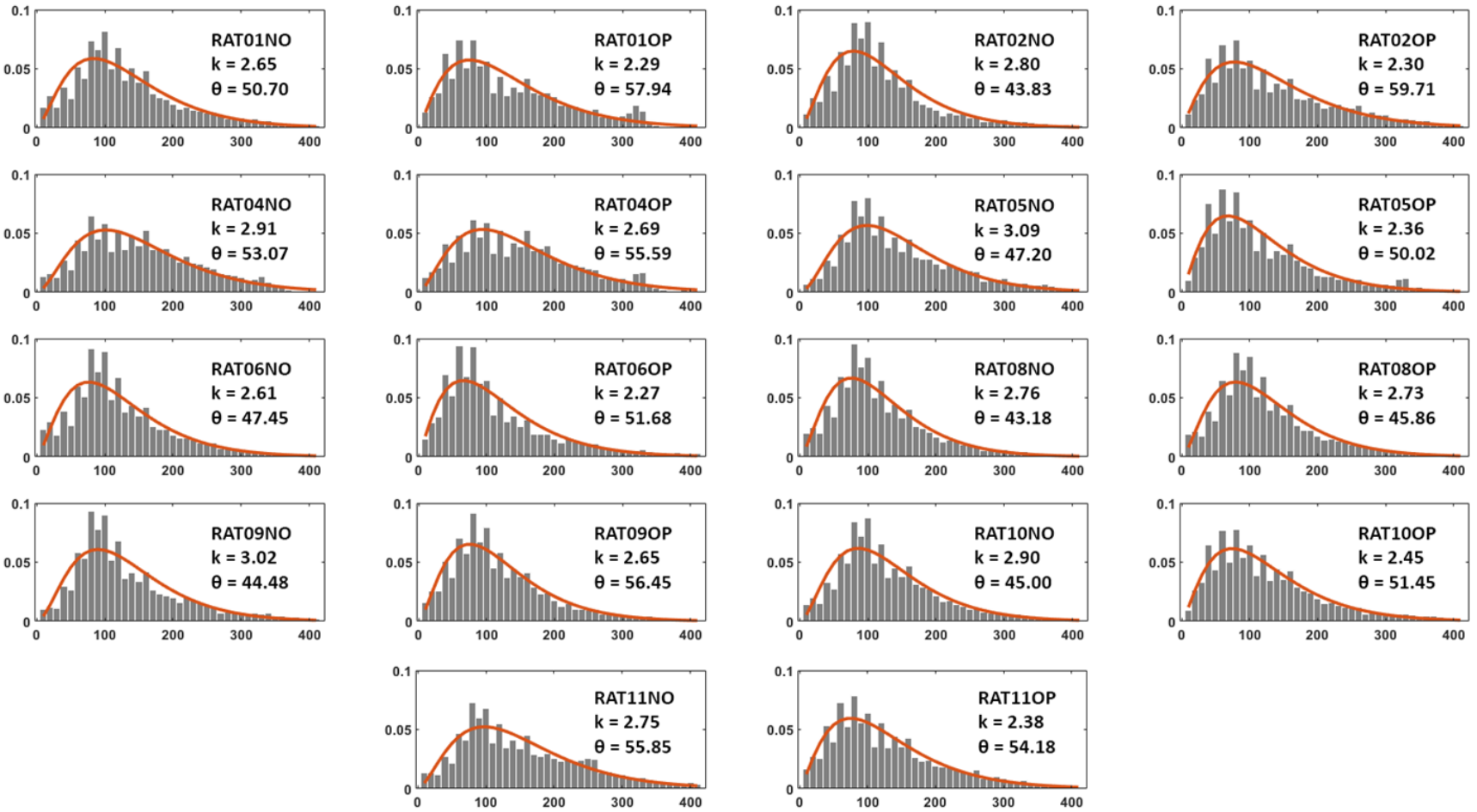

Supplementary Figure 6-S7: Histogram of surface thickness values and the estimated Gamma distribution (red) for rat femur. Vertical axes show normalised frequency and the horizontal axes show thickness values in micrometre. (NO: control group, OP: operated group).

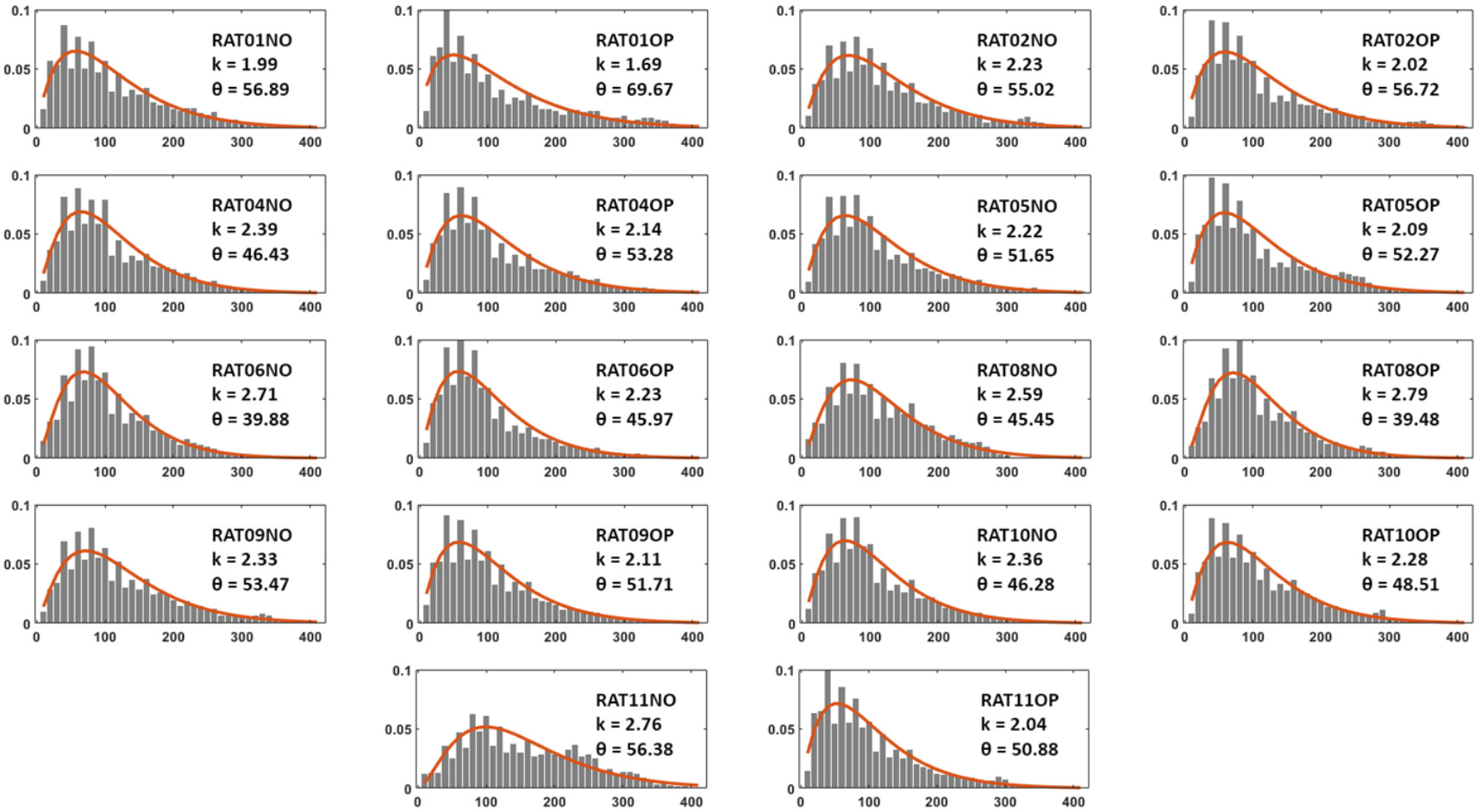

Supplementary Figure 6-S8: Histogram of surface thickness values and the estimated Gamma distribution (red) for rat tibia. Vertical axes show normalised frequency and the horizontal axes show thickness values in micrometre. (NO: control group, OP: operated group).

Supplementary Table 6-S9: Shapiro-Wilk test results for the fitted Gamma distribution and other morphometric measurements of the cortical bone. Parameters shown are: shape (k) and scale (θ) of the fitted Gamma distribution, cortical thickness (Ct.Th), and cortical porosity (Ct.Po). Test result shown as test statistics (W) and respective p-values.

			Femur				Tibia			
			NO	OP	NS	OS	NO	OP	NS	OS
Rabbit	k (1)	Test statistic (W)	0.964	0.904	0.972	0.878	0.970	0.945	0.973	0.855
		p-value	0.847	0.315	0.911	0.258	0.894	0.661	0.918	0.107
	θ (1)	Test statistic (W)	0.948	0.932	0.949	0.966	0.917	0.897	0.909	0.910
		p-value	0.696	0.533	0.661	0.865	0.409	0.273	0.345	0.354
	Ct.Th (μm)	Test statistic (W)	0.891	0.973	0.897	0.991	0.979	0.932	0.946	0.969
		p-value	0.241	0.919	0.202	0.992	0.959	0.533	0.675	0.888
	Ct.Po (%)	Test statistic (W)	0.909	0.909	0.880	0.900	0.932	0.984	0.939	0.933
		p-value	0.350	0.350	0.131	0.373	0.538	0.978	0.599	0.540
Rat	k (1)	Test statistic (W)	0.970	0.945	0.973	0.855	0.955	0.883	0.939	0.873
		p-value	0.894	0.661	0.918	0.107	0.745	0.168	0.543	0.163
	θ (1)	Test statistic (W)	0.917	0.897	0.909	0.910	0.918	0.916	0.906	0.824
		p-value	0.409	0.273	0.345	0.354	0.373	0.357	0.254	0.051
	Ct.Th (μm)	Test statistic (W)	0.894	0.868	0.870	0.886	0.860	0.912	0.857	0.906
		p-value	0.221	0.116	0.053	0.339	0.097	0.328	0.070	0.325
	Ct.Po (%)	Test statistic (W)	0.842	0.876	0.870	0.839	0.962	0.915	0.965	0.927
		p-value	0.061	0.141	0.052	0.163	0.820	0.355	0.842	0.490

Supplementary Table 6-S10: F-test results for the fitted Gamma distribution and other morphometric measurements of the cortical bone. Parameters shown are: shape (k) and scale (θ) of the fitted Gamma distribution, cortical thickness (Ct.Th), and cortical porosity (Ct.Po). Test result shown as test statistics (F) and respective p-values.

			Femur		Tibia	
			NO vs OP	NS vs OS	NO vs OP	NS vs OS
Rabbit	k (1)	Test statistic (F)	1.125	1.356	1.303	1.988
		p-value	0.881	0.651	0.736	0.385
	θ (1)	Test statistic (F)	2.068	1.157	2.211	1.544
		p-value	0.359	0.798	0.317	0.581
	Ct.Th (µm)	Test statistic (F)	1.288	1.046	3.781	2.033
		p-value	0.747	0.896	0.100	0.370
	Ct.Po (%)	Test statistic (F)	2.725	4.546	1.463	1.089
		p-value	0.209	0.110	0.628	0.914
Rat	k (1)	Test statistic (F)	1.279	2.267	1.386	2.181
		p-value	0.736	0.447	0.655	0.316
	θ (1)	Test statistic (F)	1.046	1.967	1.993	1.266
		p-value	0.951	0.539	0.349	0.725
	Ct.Th (µm)	Test statistic (F)	1.190	2.363	1.165	1.644
		p-value	0.811	0.223	0.835	0.525
	Ct.Po (%)	Test statistic (F)	1.218	8.650	2.641	2.849
		p-value	0.787	0.051	0.191	0.181

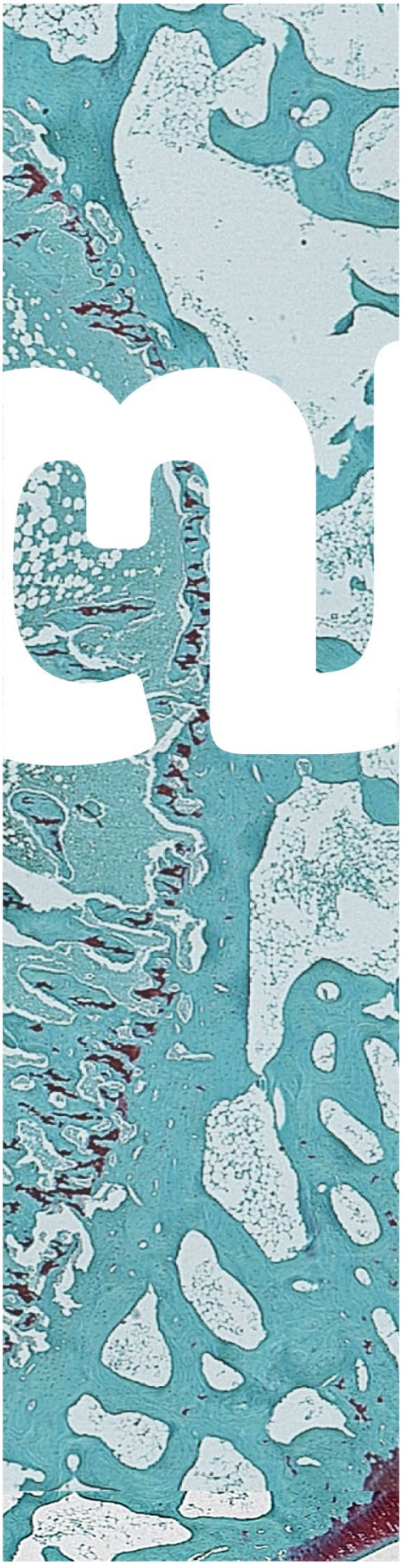

Chapter 7
Synthesis

Chapter 7

Structural degradation and biomechanical conditions of joint tissues in preclinical small animal models of knee osteoarthritis (OA) can be non-invasively assessed through quantitative morphometric analysis (QMA) using micro-computed tomography (microCT). Metrics such as cartilage thickness, trabecular separation, and joint space width were shown to be sensitive to the disease [1], [2]. Shifting joint pose between scans during image acquisition, inconsistent joint alignment relative to reference axes during image processing, combined with traditionally manual processing and analysis methods, often leads to reproducibility issues in QMA measurements which are technically challenging and time-consuming to correct in individual studies. The work presented in this thesis has examined how systematic improvements in imaging and processing protocols can lead to reproducible and dynamic quantitative analysis of joint morphology by tackling the hypotheses formulated in Chapter 1:

1. Introduction of contrast agents and control of knee pose with a positioning device during microCT acquisition allows reproducible and accurate *in situ* QMA of cartilage and joint.

2. Automating the image processing pipeline through morphological representation using spherical harmonics improves the efficiency and reproducibility of joint QMA.

3. An empirical probabilistic approach provides an automatic and model invariant solution to statistically capture morphological changes due to OA by detecting osteophyte activity.

In doing so, innovative technical solutions have been developed, presented, and discussed. This section aims to synthesise and discuss contributions and limitations across chapters and present a conclusion to this thesis as a whole.

7.1 Innovations and contributions

This highly multidisciplinary work synergised computational modelling, software engineering, and 3D image processing for morphometric analysis of OA pathological features. The protocols and techniques developed in this work have presented tangible contributions to the broader field of musculoskeletal imaging by demonstrating the potential benefits of open-source and reproducible QMA approaches to the research field through its literature review, while also addressing specific reproducibility issues in the acquisition, processing, and analysis protocols for QMA of small animal models of knee OA, leading to high quality and high throughput quantitative results.

It was shown in Chapter 3 that many methods could be translated from one modality, site, or tissue to the other. By adopting open-source practices, it is possible to improve reproducibility, reduce redundancy, and increase research throughput overall. In fact, this work built upon an open-source image processing pipeline, which is widely used for brain morphological analysis in MRI [3]. As detailed in Chapter 4 and 5, its spherical harmonics and statistical shape modelling methods were applied for joint alignment and epiphysis selection. Importantly, this work took advantage of its extensively validated algorithms by translating them to musculoskeletal CT image processing. Doing so saves development time and ensures accurate reimplementation.

Additionally, for the first time, reproducible joint and cartilage QMA results are acquired *in situ*. By combining solutions in Chapter 4 and 5, a comprehensive acquisition and processing protocol for QMA of the mouse knee using contrast-enhanced microCT was developed. Joint pose and cartilage attenuation were controlled during acquisition using a whole-animal positioning device and a cationic contrast agent injection protocol. Consistent joint alignment and subdivision are achieved in a morphologically meaningful and efficient manner with an automatic workflow based on spherical harmonics and persistent homology. In this thesis, the combined protocol is demonstrated to allow reproducible and efficient QMA, reducing the technical and time requirements needed to obtain QMA results.

Importantly, this work pioneers image processing and analysis approaches for QMA that are invariant to animal models and voxel sizes. The workflow based on morphological representation using spherical harmonics for joint alignment and subdivision is developed and

validated on rabbit and rat datasets with different animal scales and voxel sizes. The workflow is subsequently expanded to include an epiphyseal plate 'cropping' module and, without recalibration, performed well for QMA of mouse contrast-enhanced microCT datasets. In fact, its invariance property is further demonstrated in a successful alignment and subdivision of human interphalangeal and metacarpophalangeal joints with rheumatoid arthritis in a trial deployment using images from high-resolution peripheral quantitative computed tomography (HR-pQCT).

Furthermore, by statistically modelling changes in surface roughness due to OA as distributions, an invariant approach to QMA is achieved in rabbit and rat models of OA in Chapter 6. In a similar manner to the workflow developed in Chapter 4 and 5, its robustness is being tested in ongoing mouse OA studies. With various preclinical models involved in OA research, removing the need for parametric tuning helps maintain the reproducibility of computational methods and facilitates their adoption in new studies and settings.

7.2 Limitations and potential future directions

Improvements can be made regarding the segmentation protocols. Datasets in this doctoral work are segmented using the same routine. Bone segmentation is done semi-automatically with some manual contouring to exclude the menisci, which are ossified in rats and mice, during the thresholding process [4]. Cartilage, with the presence of contrast agents, has similar X-ray attenuation to other soft tissues, making segmentation based on thresholding unfeasible. Incorporating anatomical knowledge and prior training, cartilage segmentation in this study is done entirely through manual contouring, which is time-consuming and susceptible to inter-operator error. To further improve the efficiency and reproducibility of the QMA workflow, future work could focus on automating bone and cartilage segmentation routines. Recent deep learning segmentation approaches [5]–[7], often robust and open-sourced, could provide a practical alternative in future studies of joint morphology [8], [9].

In terms of future applications, the combined workflow presented in this thesis allows reproducible and efficient QMA of small animal knees. However, only animal carcasses and excised limbs are used for its validation. To fully harness the strength of 3D imaging, the combined protocol could be deployed in longitudinal studies of OA where reproducibility and accuracy of QMA measurements must be maintained from one time point to another. Besides

cross-sectional variations, longitudinal studies will involve variations due to animal growth and ageing, which may influence QMA outcomes. This thesis has already assessed the reproducibility and accuracy between cohorts at a single time point; however, its performance in longitudinal studies remains to be investigated.

7.3 Conclusion

Inconsistent poses between scans, shifting alignment relative to reference axes, and manual processing and analysis methods all lead to reproducibility and efficiency issues in QMA of the joint. This thesis examines how, and has concluded that, improvements in image acquisition, processing, and analysis protocols can lead to reproducible and dynamic quantitative analysis of joint morphology. The introduction of contrast agents and control of knee pose with a positioning device during microCT acquisition, combined with the automated image processing pipeline based on morphological representation, allows efficient and reproducible QMA of the joint. Furthermore, reproducibility and efficiency in translating QMA workflows between studies of different OA models can be maintained using the presented empirical probabilistic approach to detect osteophyte activity and the model-invariant processing workflow. Altogether, the techniques developed in this work lead to improvements in reproducibility, efficiency, and accuracy for QMA outcomes.

References

[1] K. S. Stok *et al.*, "Three-Dimensional Quantitative Morphometric Analysis (QMA) for In Situ Joint and Tissue Assessment of Osteoarthritis in a Preclinical Rabbit Disease Model," *PLoS One*, vol. 11, no. 1, p. e0147564, Jan. 2016, doi: 10.1371/journal.pone.0147564.

[2] B. A. Besler *et al.*, "Quantitative measures of bone shape, cartilage morphometry and joint alignment are associated with disease in an ACLT and MMx rat model of osteoarthritis," *Bone*, vol. 146, p. 115903, Feb. 2021, doi: 10.1016/j.bone.2021.115903.

[3] M. Styner *et al.*, "Framework for the Statistical Shape Analysis of Brain Structures using SPHARM-PDM.," *Insight J.*, no. 1071, pp. 242–250, 2006, Accessed: Mar. 06, 2020. [Online]. Available: http://www.ncbi.nlm.nih.gov/pubmed/21941375.

[4] B. A. Besler, R. E. Sondergaard, R. Müller, and K. S. Stok, "Reproducibility of

compartmental subchondral bone morphometry in the mouse tibiofemoral joint," *Bone*, vol. 81, pp. 649–653, Dec. 2015, doi: 10.1016/J.BONE.2015.09.014.

[5] F. Milletari, N. Navab, and S. A. Ahmadi, "V-Net: Fully convolutional neural networks for volumetric medical image segmentation," in *2016 4th International Conference on 3D Vision (3DV)*, Dec. 2016, pp. 565–571, doi: 10.1109/3DV.2016.79.

[6] O. Ronneberger, P. Fischer, and T. Brox, "U-net: Convolutional networks for biomedical image segmentation," in *Medical Image Computing and Computer-Assisted Intervention – MICCAI 2015*, Nov. 2015, vol. 9351, pp. 234–241, doi: 10.1007/978-3-319-24574-4_28.

[7] E. Shelhamer, J. Long, and T. Darrell, "Fully Convolutional Networks for Semantic Segmentation," *IEEE Trans. Pattern Anal. Mach. Intell.*, vol. 39, no. 4, pp. 640–651, Apr. 2017, doi: 10.1109/TPAMI.2016.2572683.

[8] B. Norman, V. Pedoia, and S. Majumdar, "Use of 2D U-net convolutional neural networks for automated cartilage and meniscus segmentation of knee MR imaging data to determine relaxometry and morphometry," *Radiology*, vol. 288, no. 1, pp. 177–185, Jul. 2018, doi: 10.1148/RADIOL.2018172322.

[9] F. Ambellan, A. Tack, M. Ehlke, and S. Zachow, "Automated segmentation of knee bone and cartilage combining statistical shape knowledge and convolutional neural networks: Data from the Osteoarthritis Initiative," *Med. Image Anal.*, vol. 52, pp. 109–118, Feb. 2019, doi: 10.1016/J.MEDIA.2018.11.009.